UNIVERSITÀ
DEGLI STUDI
DI PADOVA

Head Office: Università degli Studi di Padova

Department of Geosciences

Ph.D. Course in: Geosciences

SERIES XXXVI

TECTONIC CONTROL ON ENHANCED GEOGENIC RADON AS A FIRST ORDER FARCTOR IN RADON HAZARD ASSESSMENT

Coordinator: Prof. Agnini Claudia

Supervisor: Prof. Sassi Raffaele

Co-Supervisors: Dr. Ciotoli Giancarlo

Dr. Spagnuolo Elena

Ph.D. Candidate: Eleonora Benà

Table of contents

Abstract **5**

Riassunto **6**

FOREWORD **7**

The silent killer 7

1. INTRODUCTION **8**

1.1. Why radon gas? 8

1.2. State of the art 8

1.2.1. General background information 8

1.2.2. Epidemiology in a nutshell 9

1.2.3. Basic Safety Standards and Radiation protection 10

1.2.4. Radon hazard *vs.* radon risk 12

1.2.5. The Geogenic Radon Potential 12

1.2.6. GRP mapping 13

1.2.7. Radon as environmental tracer 14

2. PhD PROJECT **15**

2.1. Motivations 15

2.2. The study area 16

2.2.1. Geological and structural setting of the Pusteria Valley 18

References 20

3. Chapter 1: Evaluation of tectonically enhanced radon in faulted zone by quantification of the radon activity index **23**

Abstract 23

3.1. Introduction **24**

3.2. Methods **28**

3.2.1. Structural model 28

3.2.2. Radionuclide content 28

3.2.3. Soil gas sampling 30

3.2.4. Statistical and Geospatial analyses 30

3.2.5. RAI Calculation 31
3.3. Results 32
3.4. Discussion 37
3.5. Conclusions 43
References 44

4. Chapter 2: A new perspective in radon risk assessment: Mapping the geological hazard as a first step to define the collective radon risk exposure 47
Abstract 47
Graphical abstract 48
Highlights 48
4.1. Introduction 48
4.2. Methods 51
4.2.1. Test area 51
4.2.2. Experimental strategy 52
4.2.3. Dataset 53
4.2.3.1. Response variable 54
4.2.3.2. On-site predictor variables 54
4.2.3.3. Derived predictor variables 56
4.2.4. Predictor selection 57
4.2.5. Machine learning and Geogenic Radon Potential mapping 58
4.2.6. Radon risk mapping 59
4.2.6.1. Risk concept 59
4.2.6.2. Construction of Collective Risk Areas (CRAs) map 59
4.3. Results 60
4.3.1. Selected Predictors, RF Modelling and Predictors Importance 60
4.3.2. Geogenic Radon Potential map 62
4.3.3. The Collective Risk Areas (CRAs) map 63
4.4. Discussion 65
4.4.1. Interpretation of predictors in the RF model 65
4.4.2. Map of the Collective Risk Areas (CRAs) 67
4.5. Conclusions 68
References 69

5. Chapter 3: Rock deformation *vs.* radon emission: some constraints from shear stress-controlled experiments 74

Abstract 74
5.1. Introduction 75
5.2. Methods 76
5.2.1. Petrographic analysis 76
5.2.2. Shear stress-controlled experiments 76
5.2.3. Real-time radon time series 78
5.2.4. Change-point analysis 78
5.3. Results 80
5.3.1. Petrographic analysis 80
5.3.1.1. Paragneiss 80
5.3.1.2. Granite 81
5.3.1.3. Orthogneiss 82
5.3.2. Shear stress-controlled experiments 83
5.3.2.1. Paragneiss 84
5.3.2.2. Granite 86
5.3.2.3. Orthogneiss 88
5.4. Discussion 90
5.5. Conclusions 92
References 92

6. CONCLUSIONS 95
Chapter 1. What is the potential degassing process along the non-seismic Pusteria fault system and its role in increasing the GRP at surface? 95
Chapter 2. What is the effectiveness of mapping the geological hazard to define the collective radon risk exposure? 96
Chapter 3. What is the potential relationship between radon migration dynamics and rocks deformation? 97

Appendix 1 99
Appendix 2 104
Appendix 3 112

Abstract

The main goal proposed in this thesis aimed to investigate the tectonic control on enhancing the geogenic radon component as a fundamental factor in radon hazard, and further radon risk assessment. In particular, the importance of the geogenic radon potential, originated by degassing processes in faulted areas, has been deeply investigated. This so-called *Tectonically Enhanced Radon* quantity can increase radon availability at surface and its ability to influx within buildings. Mapping the geogenic radon potential represent a crucial tool for both Rn hazard and Rn risk assessment and the first step to identify the Radon Priority Areas as required by the European regulation.

To address this goal, the thesis has been developed following two different parallel approaches: at the macro- and micro scale.

At the macro-scale, Rn and other soil gases degassing processes along an aseismic fault system and its role on the degassing as an additional component for the Geogenic Radon Potential, has been investigated. Furthermore, a transition from the Rn hazard toward the more comprehensive Rn risk concept has been proposed, in order to suggest a new and clear methodology to define the Radon Priority Areas as required by the European regulation and by the radiation protection objectives.

At the micro-scale the potential relationship between Rn migration dynamics and rock deformation mechanisms has been investigated on three different lithologies, by simulating the seismic cycle using SHIVA apparatus in the laboratory.

The chosen test area (~60 km^2) is located in the Pusteria Valley (Eastern Alps, Bolzano) due to its well-known geological, structural and geochemical characteristics and the availability of numerous additional data.

These evidences increase the knowledge about radon migration mechanisms in different geodynamic environments and will have important implications on the collective risk assessment and the further identification of Radon Priority Areas under a new, more comprehensive geological perspective.

Riassunto

L'obiettivo principale proposto in questa tesi è stato quello di indagare il controllo che ha la tettonica sull'incremento della componente del radon geogenico come fattore fondamentale nella valutazione della pericolosità e del rischio radon. In particolare, è stata studiata in dettaglio l'importanza del Potenziale Geogenico di Radon originato da processi di degassamento in zone di faglia. Questa quantità, definita come *Tectonically Enhanced Radon,* può aumentare la disponibilità di radon in superficie e la sua capacità di infiltrarsi all'interno degli edifici. La mappatura del Potenziale Geogenico di Radon ha un ruolo chiave nella valutazione della pericolosità e del rischio radon ed è il primo passo per identificare le aree a priorità di radon, come richiesto dalla normativa Europea.

Per raggiungere questo obiettivo, la tesi è stata sviluppata su due linee di ricerca parallele: alla macroscala ed alla microscala.

Alla macroscala sono stati studiati i potenziali processi di degassamento del radon ed altri gas lungo un sistema di faglie asismiche e il ruolo che hanno sul degassamento, come componente addizionale al Potenziale Geogenico di Radon. Inoltre, è stata proposta una transizione dal solo concetto di pericolosità di radon a quello più completo di rischio radon, al fine di suggerire una nuova e chiara metodologia per definire le aree a priorità di radon, come richiesto dalla normativa Europea e dagli obiettivi di radioprotezione.

Alla microscala è stata studiata la potenziale relazione tra le dinamiche di migrazione del radon, ancora dibattute ed i meccanismi di deformazione delle rocce su tre diverse litologie, simulando il ciclo sismico in laboratorio con l'apparato SHIVA.

L'area in studio (~60 km^2) è situata in Val Pusteria (Alpi Orientali, Bolzano) ed è stata scelta per le sue caratteristiche geologiche, strutturali e geochimiche ben conosciute e per l'ampia disponibilità di dati.

Queste evidenze aumentano le conoscenze sui meccanismi di migrazione del radon in diversi ambienti geodinamici e avranno importanti implicazioni sulla valutazione del rischio collettivo e sull'ulteriore identificazione delle aree a priorità di radon in una nuova e più completa prospettiva geologica.

FOREWORD

The silent killer

95% of the tumours is ascribed to the relationship between the humans and the environment (The Cancer Atlas, 2019). Among all the existent tumours, the lung cancer is the leading cause of mortality in industrialised countries, representing the 18% of the total amount of deaths due to cancer diagnosis.
In the world: 2,094,000 new cases per year of lung cancer, 1,761,000 lung cancer deaths (GLOBOCAN, 2018; Riudavets, 2022). 3% of these cases of death (~53,000) is ascribed to radon gas exposure (Gaskin et al., 2018).
In Europe: 470,000 new cases per year of lung cancer, 388,000 lung cancer deaths (GLOBOCAN, 2018). Estimated 21,000 of these cases of death are ascribed to radon (referred to ^{222}Rn) gas exposure (WHO, 2009).
In Italy: 43,900 new cases per years of lung cancer. 10% of these cases (between 4,000 and 5,000) is due to radon (referred to ^{222}Rn) gas exposure (AIRTUM, 2022).
Despite these scary numbers, radon risk remains still scarcely known by the population. At the same time, these numbers are sufficient to realise how crucial it is to dedicate time and effort to this silent killer.
However, the question is: how can citizens be concerned about something not visible at all?
Contrary to other natural hazards and risks (i.e., landslides, floods, earthquakes, eruptions) marked by immediately visible effects, radon is not visible and its effects have impact on human health over the time.
Additionally, radon displays an ambiguous nature: on the one hand it has a natural origin, on the other hand its concentration in the indoor environments is anthropogenic controlled.
This control, with regards to prevention and remediation, requires personal initiative to some extent.
For these reasons, in this thesis, an innovative geological point of view, in terms of controlling factors (e.g. faults and tectonic), planning and remediation (e.g. hazard and risk) has been proposed and detailed analysed at a double scale (from macro to micro).
Thereafter, the introduction has been voluntarily opened with the question "*Why radon gas?*" in order to propose motivations aimed to explain why it is fundamental to investigate this natural risk.

In 2015, UN member states agreed to 17 global Sustainable Development Goals (SDGs 2030) to end poverty, protect the planet and ensure prosperity for all.

This PhD project work contributes towards the following SDG:

1. INTRODUCTION

1.1. Why radon gas?

Radon (^{222}Rn, hereafter referred to as radon or Rn) is a radioactive gas considered the main source of ionising radiation exposure to the living population. The US Environmental Protection Agency (EPA), the World Health Organization (WHO) and other international institutions agree that approximately 50% of all the ionising radiation, received during a lifetime, is the result of radon exposure (EPA, 2023).

It has been also widely documented (WHO, 2009) as a significant hazard, in particular, when it accumulates in indoor environments, such as residential houses, schools and workplaces.

1.2. State of the art

1.2.1. General background information

In daily life, people and natural organisms in general, are constantly exposed to different natural sources of ionising radiation and this exposure is unavoidable. Among all the natural sources of radiation, this thesis focuses on those derived from the natural primordial radionuclides which are present from the solar system formation (^{238}U, ^{235}U and ^{232}Th) (EANR, 2019).

From a chemical point of view, radon is a radioactive noble gas and it is found in nature as three primary isotopes: ^{222}Rn (Radon *s.s.*), ^{220}Rn (Thoron) and ^{219}Rn (Actinon) (Nazaroff et al., 1998).

^{222}Rn (hereafter, radon or Rn) belongs to ^{238}U decay chain (see Fig. 1) and directly originates from the radium (^{226}Ra) by alpha decay mechanism. ^{222}Rn is characterised by the short half-life of 3.8 days. In particular, radon gas has a density of 9.73 gL^{-1} (T = 0°C, P = 1 atm) which is 7.5 times higher than the air density. It is also very soluble in water, and its solubility decreasing with increasing temperature (e.g. 530 $cm^3 \cdot kg^{-1}$ at T = 0°C; 230 $cm^3 \cdot kg^{-1}$ at T = 20°C; 169 $cm^3 \cdot kg^{-1}$ at T = 30°C), however it is also easily removable from water (Cinelli et al., 2019).

Similarly, ^{220}Rn (hereafter, thoron or Tn) belongs to ^{232}Th decay chain and derives from ^{224}Ra by alpha-decay. Tn has also a very short half-life of 55.6 seconds.

In this thesis, the attention is primarily focused on radon and, to a lesser extent, on thoron natural radioactivity.

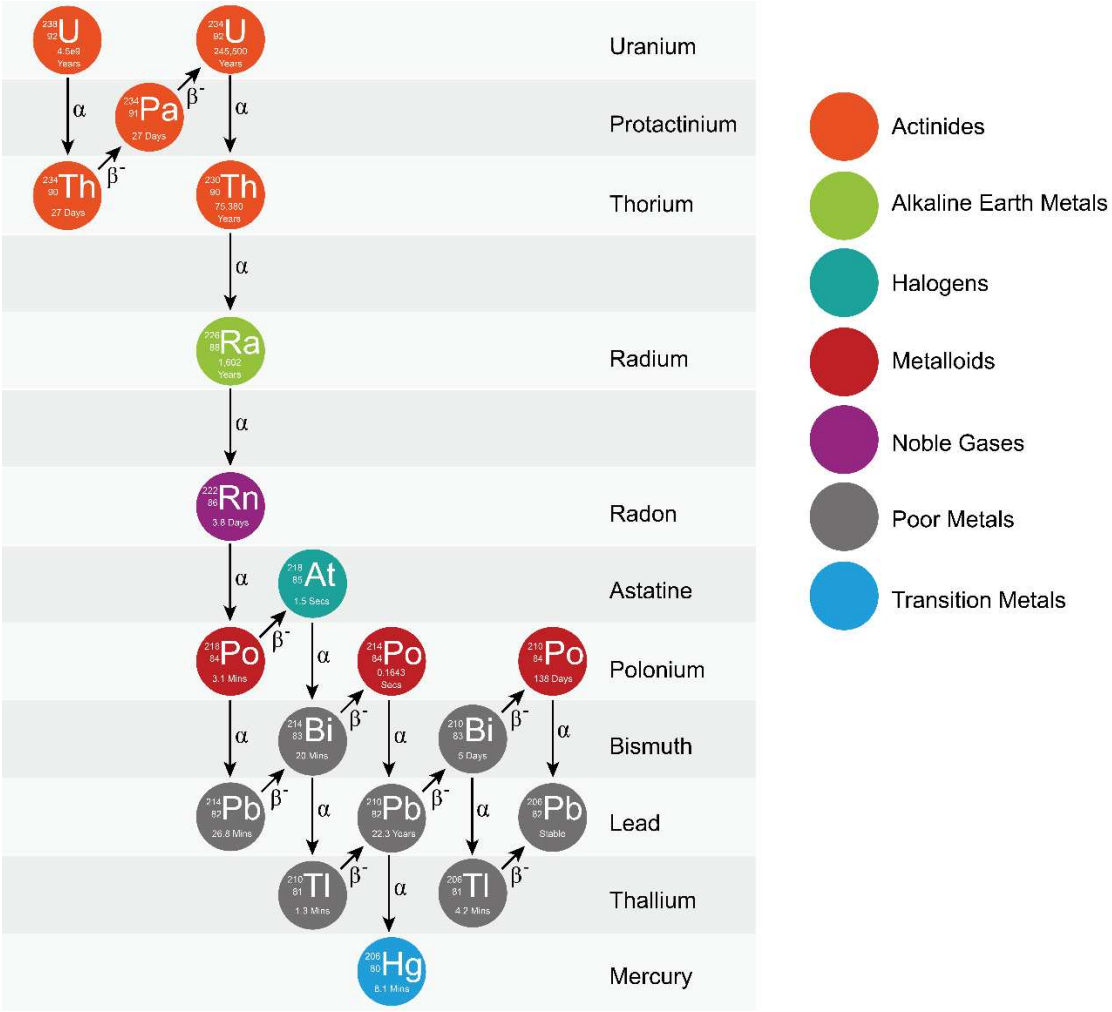

Figure 1. Natural ^{238}U radioactive series (Cinelli et al., 2019; source: UNSCEAR, 2000, Vol. 1 ANNEX B, Table 3).

1.2.2. Epidemiology in a nutshell

Being a radioactive gas, Rn represents a serious hazard for the human health. In outdoor air, Rn concentration is very low and does not represent a health risk; in indoor spaces it can reach hazardous concentrations. In particular, Rn was declared human carcinogen by the US Environmental Protection Agency (EPA, 1987), and by the International Agency for Research on Cancer (IARC, 1988). The WHO, through the IARC, has further classified Rn gas in the cancerogenic group 1, i.e., substances with sufficient evidences of carcinogenicity, based on epidemiological studies in humans.

As previously emphasised, Rn gas is a source of ionising radiation and this is due to its ability to disintegrate into other radioactive atoms releasing alpha particles and gamma radiations. Despite

alpha particles are highly energetic, they are a type of ionising radiation with low penetration capacity. In fact, Rn gas (half-life = 3.8 days) itself is not hazardous, on the contrary its decay products or progenies (e.g., Polonium, Po; Actinon, At; Bismuth, Bi; and Lead, Pb) are solid and characterised by a shorter half-life (in the order of minutes and seconds). For this reason, Rn progeny has the capability to adhere to other small particles and remain in the lung, exposing the lung to harmful radiation (Ruano-Ravina et al., 2023).

Specifically, most of inhaled Rn is effectively eliminated via respiration prior to its decay. Nevertheless, only a small amount is released into the lungs, bloodstream, and other organs in the body. The decay products attached to the atmospheric particulate can be inhaled and deposited on the cavities of the respiratory system. Consequently, these products emit radiation (mostly alpha radiation) that irradiates the bronchial cells. In some cases, this radiation may cause harm to the DNA of the cells which may evolve into lung cancer if not properly repaired by the suitable cellular mechanisms. Therefore, Rn behaves as a 'carrier' of its progeny, which are mostly responsible for causing the biological damage. For the sake of brevity, it is commonly referred to as “radon risk”, meaning the risk associated with exposure to radon decay products (ISS, 2019).

1.2.3. Basic Safety Standards and Radiation protection

Exposure to indoor radon is a serious issue that has prompted Europe to introduce legislation aimed to reduce Rn exposure, named the Basic Safety Standards (BSS) Directive 2013/59/EURATOM. This European Directive deals with all the aspect of the radiation protection and all the Member States are obliged to transpose it into a National legislation. In this regard, BSS was also transposed in the Italian legislation with the Legislative Decree n.101/2020. These regulations, on the one hand, set maximal national reference levels aimed to reduce Indoor Radon Concentration (IRC) exposure; on the other hand, urges the public administrations to create a Radon Action Plan to define the so-called Radon Priority Areas (RPAs).

The RPA is defined as “the frequency or the probability that in an area a significant number of buildings exceed the reference level (RL) value”. However, different issues arise from this apparently clear definition, starting from the interpretation of “significant number of buildings” and moving to the definition of a uniform RL. As Petermann et al. (2022) recently emphasised, the interpretation of "significant number" of buildings is based on the idea of geogenic hazard rather than the more comprehensive concept of geogenic risk. However, at the regional scale, there is no uniform agreement on the selection of the RL and the percentage of probability threshold (p_0) exceeding this level.

In general, for residential buildings, most European governments favour for a reference level of 300 Bq·m^{-3} and a common probability threshold of 10% (Bossew, 2018). For instance, Finland, Germany, Greece, Montenegro and Spain chose a RL=300 Bq·m^{-3} and p_0=10% (for Germany, the RL is referred to ground-floor rooms in buildings with basement only; for Spain, the RL is referred to the ground or first floor rooms only). Ireland has chosen RL=200 Bq·m^{-3}, p_0=10%. Other countries, such as Austria and Switzerland, define also different priority levels based on the RL and IRC measurements (Bossew, 2018). Italy chose a RF=300 Bq·m^{-3} and p_0=15% (D. Lgs. n. 101/2020). For the workplaces, all countries chosen the RL of 300 Bq·m^{-3}. These formulations emerged from a complicated, heavily politicised decision process (Bossew and Suhr, 2023).

Figure 2 shows a complete and global overview of the definition of the RPA in Europe (Bossew and Suhr, 2023); the comparison among the countries is quite difficult. Despite the problem of the RPA, harmonisation has been addressed in the European MetroRadon project and in Bossew et al. (2021), no authoritative solutions exist at the moment.

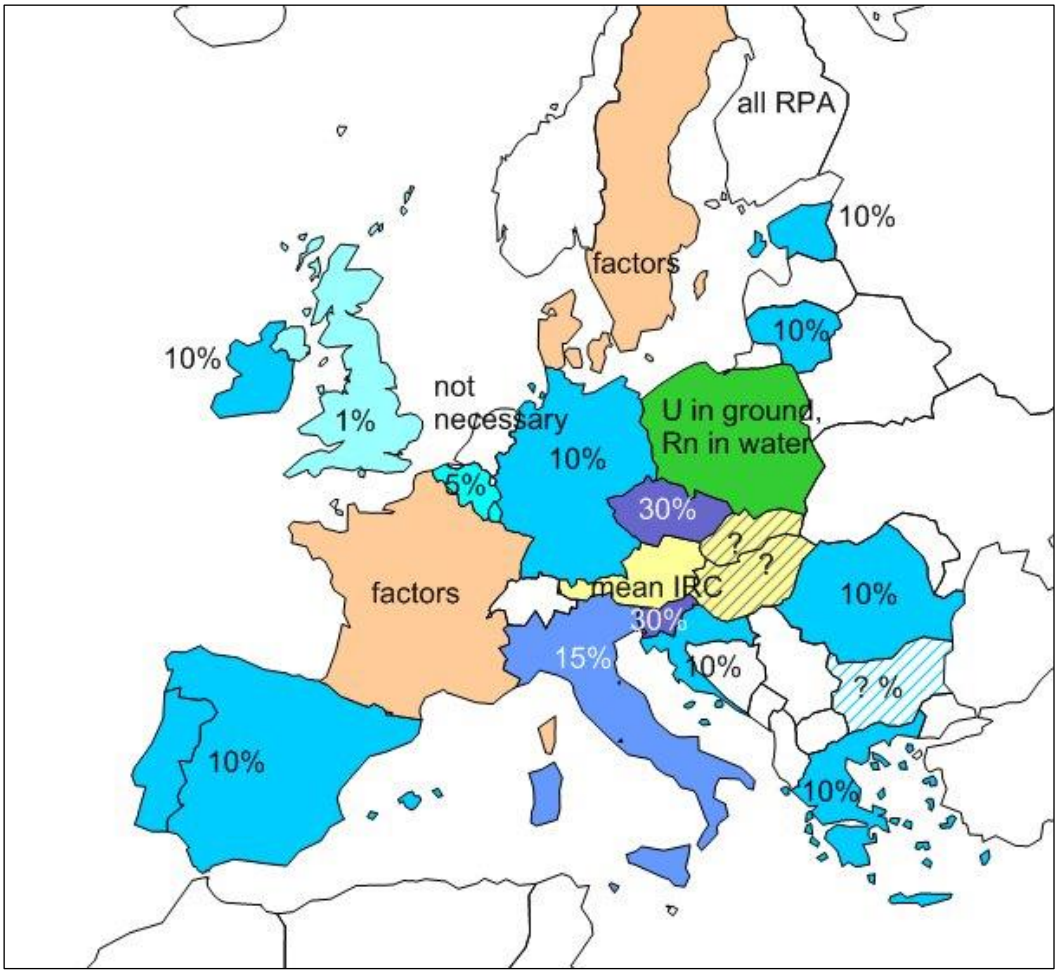

Figure 2. Definitions of RPA in Europe: blue: based on exceedance probability (% prob > RL) in a geographical unit; but notice that RLs are different; yellow: based on mean per unit; rose: based on factors such as geology; green: different; white: not known, entire country RPA (Finland) or considered not necessarily due to overall low Rn (Netherlands). Based on data from Perko et al., 2022, state early 2022 (Bossew and Suhr, 2023).

1.2.4. Radon hazard *vs.* radon risk

Another issue dealing with the tricky "significant number" of buildings is that this interpretation is only based on the idea of geogenic hazard rather than the collective concept of geogenic risk. The conventional idea of RPAs does not consider the number of people affected. This is founded in the concept of the Geogenic Radon Potential (GRP) conceptualised as “what Earth delivers in terms of radon” (Bossew, 2015) and this quantity can potentially influx within buildings. For this reason, the GRP is considered the most important spatial predictor of the IRC (Bossew, 2020).

In this way, it is straightforward to think about the link between high GRP values and high IRC and, as a consequence, define an RPA as a percentage of dwelling exceeding a threshold value; however, in this case, the number of the people affected has not been considered. The main issue is as follows: without people involvement the concept of risk cannot be discussed.

The transition from geogenic hazard to geogenic risk is a fundamental step in defining the RPAs, as required by European regulations and necessary for radiation protection. In this regard, the radiation protection objectives are twofold: (i) to protect individuals from high exposure, to reduce the individual risk; (ii) to avoid high exposure to the collective: the detriment (i.e., number of lung cancer fatalities) to society is proportional to the collective exposure (Bossew and Petermann, 2021; Elio et al., 2023).

Starting from all these considerations and given the absence of an unambiguous approach for RPAs identification at European level, in this thesis the mapping of the collective risk areas (or detriment, CRAs) as a complement for the mapping of individual risk areas (IRAs) linked to IRC (i.e., “classical” RPA) has been proposed. This first step may lead to recovery actions of these areas as required by legislation. To reduce the detriment, the Rn abatement policy must prioritise these areas and at the same time, also considering regions with high individual risk.

1.2.5. The Geogenic Radon Potential

As geologists, we considered the measure and mapping of the Geogenic Radon (GR, i.e., radon with a natural origin) in the shallow environment as a fundamental starting point to understand the hazard over an area. Indeed, the concentration of radon gas in the environment can vary depending on the geological characteristics of an area. When radon is produced within the Earth, it can migrate through permeable rocks and soil, eventually reaching the surface. Once at the surface, radon can be released into the air or dissolved in water, or entering buildings.

As already mentioned, an optimal hazard indicator is represented by the Geogenic Radon Potential (GRP) regarding the radon released from the Earth, starting from the geogenic sources (e.g.,

radionuclides content, faults and fractures) towards the atmosphere (Bossew, 2015; Bossew et al., 2020). In particular, the GRP is characterised by the interaction of three natural processes:

• the Background Radon Source (BRS), the process that produces Rn through the decay of the principal radionuclides in rocks (e.g. ^{238}U, ^{232}Th);

• the Tectonically Enhanced Radon (called TER, from Benà et al., 2022), the additional process allowing radon to migrate through permeable pathways to the surface (e.g., faults and fractures);

• the Surface Radon Exhalation (SRE), the process allowing radon release from the ground surface toward the atmosphere. This radon quantity, which has not measured in the frame of this project, represents the amount of radon that could potentially enter buildings. However, BRS and TER represent the dominant geological radon sources.

1.2.6. GRP mapping

Over the years, several approaches have been applied to estimate the GRP over an area (e.g., Neznal et al., 2004; Bossew et al., 2015; Pasztor et al., 2016; Ciotoli et al., 2017; Giustini et al., 2019; Petermann et al., 2021; Coletti et al., 2021) as precise as possible.

The first and easiest method to define the GRP was proposed by Neznal et al. (2004). Neznal approach was based on the measure of two quantities: the Rn concentration in the soil and the soil permeability. Equation 1 reports the Neznal formula to calculate the GRP (dimensionless):

$$GRP_{Neznal} = \frac{SGRC}{-\log_{10} k - 10} \quad (1)$$

where *SGRC* is the Soil Gas Radon Concentration (kBq·m^{-3}) measured at a depth of about 0.8 m, and *k* is the soil gas permeability in m^2.

More recently, Pasztor et al. (2016) and Ciotoli et al. (2017) applied multivariate geospatial analysis (regression kriging and geographical weighted regression, respectively) for GRP modelling by using selected environmental proxies for the first time.

In the past three years, researchers have developed more advanced multivariate techniques, such as regression kriging (Coletti et al., 2021) and machine learning (ML) algorithms (e.g., random forest, etc.), which include several predictors or proxy variables associated with the geogenic Rn component (Petermann et al., 2021). However, it is important to emphasise that all these techniques require the measurement of SGRC or IRC as a response variable (variable to predict).

An issue is that many European countries do not dispose of sufficient SGRC and permeability data to allow the modelling of a GRP map; for this reason, in 2010 was conceptualised a comparatively

new concept is the Geogenic Radon Hazard Index (GRHI, Bossew et al., 2020). The origin of the GRHI concept arose from the necessity to determine a specific measure using the geogenic variables regionally available. The difficulty lies in maintaining consistency between GRHI assessments in neighbouring regions when utilizing different predictors. In other words, GRHI values should be equivalent among regions with similar geogenic factors but varying data sources. For instance, one region may have data on uranium concentration in topsoil and soil granulometry, while another region may have information on SGRC, soil type, and ambient dose rate.

A first way to avoid this issue has been proposed by Cinelli et al. in 2015. The proposal was to to assign weights to classified continuous or categorical input variables (covariates) based on their importance in contributing to the index. These weights aim to reflect the relevance of each covariate in relation to the calculated index. The weighted "mean class," normalised from 0 to 1, is then used to determine the Geogenic Radon Hazard Index (GRHI), conceived as a dimensionless quantity. The weights assigned to each covariate are based on the correlations observed with the GRP in regions where the GRP data are effectively available.

Another way to avoid the issue is the application of other techniques which does not require the response variable: The Spatial Multi Criteria Decision Analysis (SMCDA, Ciotoli et al., 2020). This approach does not require the presence of a response variable directly measured in the soil (e.g. SGRC) allowing the estimation of the GRP using the predictor variables regionally available.

Among all the cited techniques, in this thesis the multivariate geospatial analysis (regression kriging) and a multivariate machine learning technique (forest regression) have been applied to create the ^{222}Rn, ^{220}Rn and CO_2 contour maps and the GRP map respectively.

1.2.7. Radon as environmental tracer

As explained in the previous paragraphs, soil Rn is usually utilised as the most important spatial predictor for the IRC, but it is also an important tracer of geogenic processes (e.g. volcanic activity, earthquake precursor, tracer of buried faults, interaction between ground water and surface water), as Rn concentrations in geogenic environments react sensitively to changes of their physical-chemical state.

Among all the geological process, the relationship between radon and faults and the idea of radon gas as a seismic precursor has always fascinated researchers. Over the past decades, radon in soil gas and dissolved gases has received considerable attention as an earthquake precursor and to this aim a large number of studies spanning from geology and geochemistry to nuclear engineering have been conducted to better understand Rn variation in response to seismic events (see for example Wakita et al., 1980; Wakita, 1996; Ghosh et al., 2009; Koike et al., 2009; Jordan et al., 2011; Wang et al., 2014,

Iwata, 2018; Liu et al., 2023; Walia et al., 2023). However, unambiguous and systematic data and observations of a possible correlation between Rn and precursory activity of such natural hazards are still lacking.

In this framework over the years, laboratory experiments had a fundamental role in understanding the possible relationship between Rn behaviour and rock fracture and deformation dynamics (see for example Tuccimei et al., 2010; Mollo et al., 2011; Scarlato et al., 2013; Cannelli et al., 2016, Li et al., 2022, 2023). The experiments offer a unique opportunity to reproduce natural conditions in a controlled environment at the laboratory scale (micro-scale), to have a direct access to the Rn source (the rocks) and isolate either one or group of variables at time. However, also in this case, results are not conclusive on a systematic correlation between radon migration through fault and fractures and this topic requires deepest investigation.

2. PhD PROJECT

2.1. Motivations

The main goal of this project is to investigate the tectonic control (role of the fault zones) on enhancing geogenic radon (TER component) as fundamental factor in radon hazard (and risk) assessment.

To address this goal, the project has been developed following two different scale: (i) macro-scale: to investigate the potential Rn degassing processes along an aseismic fault system; the role of fault degassing as an additional component for the GRP; a clear definition of this additional component; in terms of radioprotection, propose a definitive transition toward the more comprehensive Rn risk concept in order to define a clear methodology to define the RPAs in the European Rn community is still missing; (ii) micro-scale: to find clear evidences of the relationships between Rn migration dynamics (i.e., Rn geochemical behaviour) and rock deformation mechanisms (seismic cycle) at the laboratory scale since the experiments allow a direct access to the Rn source.

Behind this main goal there are many questions that remains unanswered around the complex relationship between radon and faults and this project aimed to addressed in particular three main questions that can be summarise as follow:

1. What is the potential degassing process along an aseismic fault system and its role in increasing the GRP at surface? (macro-scale)
2. What is the effectiveness of mapping the geological hazard to define the collective radon risk exposure? (macro-scale)

3. What is the potential relationship between radon migration dynamics and rocks deformation? (micro-scale)

Each question corresponds to one of the three chapters and aimed to find the answer related to the proposed issue. In details, the first and second chapters have been developed at the macro-scale, while the third chapter at the micro-scale.

In chapter 1 "Evaluation of tectonically enhanced radon in fault zones by quantification of the radon activity index", the tectonic control on enhanced geogenic radon at surface has been investigated along an aseismic fault system (the Pusteria fault system). This investigation arose since numerous studies in literature show examples of radon migration along faults that may be ascribed to the TER concept but specific studies aimed at quantifying this geogenic radon component are still lacking. Furthermore, most of these studies deal with seismic faults, and aseismic fault systems had never been investigated before. In the first chapter, I focused on the one hand on the evaluation of the potential degassing process along the selected fault system, by the analysis of the distribution and the magnitude of radon, thoron and CO_2 soil gas anomalies. On the other hand, I aimed to quantify the TER component in terms of a new Radon Activity Index (RAI) explaining the geochemical activity of the fault.

In chapter 2 "A new perspective in radon risk assessment: mapping the geological hazard as a first step to define the collective radon risk exposure" I aimed to give a new perspective in the radon risk mapping introducing the concept of the Collective Risk Areas (CRAs). This study arose from the above proposed issue highlighting that in the Rn community, at the moment, a uniform and clear methodology to map the Rn risk and, as a consequence, to define the RPAs as required by the European regulation is still missing. In this chapter, the simple risk equation, which combines hazard, vulnerability and exposure factors, has been introduced to map the Rn risk. The fundamental starting point is mapping the GRP (the geology) as precise as possible by applying a robust multivariate machine learning technique using as a response variable the soil gas radon directly measured in the field and other geological variables strictly correlated to Rn. In this way, a new geological-based method to define the Rn risk and, as a consequence, the RPAs has been proposed.

In chapter 3 "Rock deformation vs. radon emission: some constraints from shear stress-controlled experiments" the potential relationship between radon migration dynamics and rock deformation has been investigated in a simplified, closed and controlled environment. The reason that prompted this specific study arose from the previous two chapters which highlighted the relevance of using

predictive variables to map the soil radon and define the GRP for an informed formulation of radon risk. Additionally, previous chapters demonstrated that the TER component (i.e. due to the presence of faults and fractures) is the most influencing factor for radon migration in the atmosphere among all the variables influencing radon migration (e.g. TGDR, faults and fractures density, presence of carrier gas, soil permeability, elevation). For this reason, a more detailed investigation of radon migration in the presence of pre-existing faults under close to natural tectonic deformation conditions is desirable at a microscopic scale. In chapter three, I carried out an experimental investigation aimed at understanding the instantaneous variation of radon counts due to frictional instabilities induced on the rock sample. To do this, a new experimental setup has been designed on the rotary shear apparatus named SHIVA (Slow to High Velocity Apparatus, Di Toro et al., 2010) to reproduce natural conditions at the laboratory scale.

2.2. The study area

The chosen test area (~60 km^2) is geographically located in the Pustertal/Pusteria Valley, in Bolzano province (Italy) and embraces part of the municipalities of Terento/Terenten, Chienes/Kiens and Falzes/Pfalzen. There are several reasons behind the choose of this study area and many questions remain unanswered about radon behaviour in this zone. In particular, in the early 90s the Environmental Protection Agency (*Agenzia per la protezione dell'ambiente*) carried out detailed indoor radon concentration (IRC) surveys in 1900 dwellings belonging to all the municipalities (116) in the entire Bolzano province (Minach et al., 1999; Verdi et al., 2004). As a result of this intense study, each municipality was allocated an average IRC value and the province was divided into four different classes of potential risk according to the current legislation at that time (90/143/EURATOM).

The resultant map (Fig. 3) shows that the municipalities falling into the classes between 200-400 $Bq \cdot m^{-3}$ and >400 $Bq \cdot m^{-3}$ are located in the highest part of the Venosta Valley and in the Pusteria Valley, in particular in the municipalities of Terento, Chienes and Falzes displaying average values are equal of 300 $Bq \cdot m^{-3}$, 358 $Bq \cdot m^{-3}$ e 535 $Bq \cdot m^{-3}$ respectively.

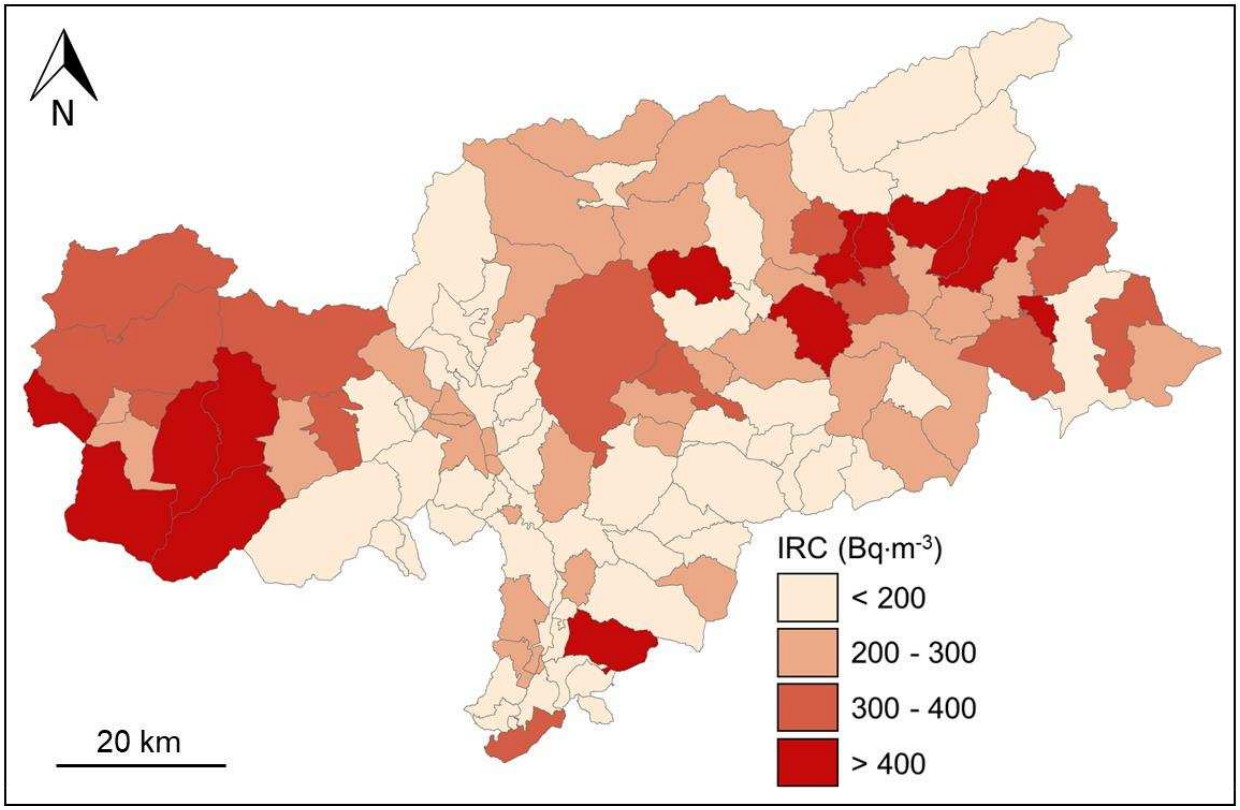

Figure 3. IRC concentration in Bolzano province. (Modified after Minach et al., 1999 and Verdi et al., 2004).

The studies at the time ascribed these high IRC values to the geological formations under the "high risk" municipalities. An apparently good correlation between the high IRC values and the presence of granitoids rocks (e.g. granite, orthogneiss) has been observed. However, the role of the tectonic factor has not been considered at all. In particular, the study area is located across a wide fractured zone which could potentially enhanced gas permeability and, as a consequence, Rn availability at surface which can potentially influx within buildings.

For this reason, in this project the role of the tectonic factor in enhancing Rn emission, has been analysed into depth as a first order factor in radon hazard and risk assessment. The test site is located across the complex Pusteria fault system (PL, KV and DAV) which originates a wide fractured zone (minor faults) viewable from the elaborated structural model (see chapter 1, Methods section).

This fault system represents and ideal geological scenario and the first case study aim to investigate the role of a non-seismically active fault on enhancing radon gas at surface.

2.2.1. Geological and structural setting of the Pusteria Valley

The Pusteria Valley is located in the Italian sector of Eastern Alps (NE Italy). The crystalline basement of the Eastern Alps consists of the Penninic, Austroalpine and Southalpine domains (from the deepest to the shallowest) (Schmid et al., 2004). Before the Alpine orogenesis, the Penninic metamorphic basement was part of the southern margin of the European plate, which collided in late-

Mesozoic to Cenozoic times with a promontory of the African plate (the Adria microplate) leading to the closure of the Penninic-Tethyan Ocean. The Austroalpine and the Southalpine metamorphic basements were located on the northern margin of the Adria microplate. The Periadriatic Lineament, an East-West trending, dextral transpressive strike-slip fault, separates the Austroalpine crystalline basement to the north from the Southalpine one to the south (Schmidt et al. 1989). The Austroalpine crystalline basement in the Eastern Alps consists of pre-Variscan sequences. These were mainly affected by a Variscan (320-350 Ma) metamorphic event covering the whole temperature range of the amphibolite and greenschist facies at metamorphic thermal gradients of about 40°C·km^{-1}, partly affected by Alpine metamorphic overprint (see review in: Sassi et al., 2004; Spiess et al., 2010). It is mainly made up by paragneisses and micashists (locally grading to migmatites), in which orthogneisses, amphibolites, quartzites and marbles are interlayered. Eclogites, metabasites and metaultramafics locally occur. The Southalpine crystalline basement in the Eastern Alps consists of a thick phyllitic sequence affected by Variscan metamorphism under greenschist facies conditions and thermal gradient of about 40°C·km^{-1} (Spiess et al. 2010).

The Austroalpine block is cut by two major E-W trending tectonic lines: the DAV (Defferegggen-Antholz/Anterselva-Vals/Valles (DAV) fault and the Kalkstein-Vallarga (KV) fault. The DAV is a ~80 km long mainly mylonitic shear zone with dominant sinistral strike slip delimiting towards the south the Alpine metamorphic overprint (Muller et al. 2000). The KV is a transpressive strike-slip fault (Borsi et al., 1978). These two faults merge westwards close to the Periadriatic Lineament (PL) (i.e., Insubric Line). Lammerer et al. (2011) show a composite geologic section through the Tauern Window with seismic reflectors from the TRANSALP line (Lüschen et al., 2006). In this area, the Bündner schists formation, containing serpentinites, is folded and the southward limb outcrops extensively on the north facing side of Wurmtaler whereas it is buried under the Austroalpine domain area, the DAV and PL considered in this thesis.

References

Associazione Italiana Registro TUMori, I numeri del cancro in Italia (2022)

Benà, E., Ciotoli, G., Ruggiero, L. Coletti, C., Bossew, P., Massironi, M., Mazzoli, C., Mair, V., Morelli, C., Galgaro, A., Morozzi P., Tositti, L., Sassi, R. Evaluation of tectonically enhanced radon in fault zones by quantification of the radon activity index. Sci Rep 12, 21586 (2022). https://doi.org/10.1038/s41598-022-26124-y

Borsi S., Del Moro A., Sassi F.P., Zanferrari A., Zirpoli G. (1978). New geopetrologic and radiometric data on the Alpine his-tory of the Austridic continental margin south of the Tauern Window Eastern Alps). Mem Sci Geol Univ Padova, 32, 1 -17.

Bossew, P., 2015. Mapping the geogenic radon potential and estimation of radon prone areas.

Bossew P. 2018 Radon priority areas definition, estimation and uncertainty Nucl. Technol. Radiat. Prot. 33 286–92 (2018)

Bossew, P., Cinelli, G., Ciotoli, C., Crowley, Q. G., De Cort, M., Medina, J. E., Gruber, V., Petermann, E., Tollefsen, T. Development of a Geogenic Radon Hazard Index – Concept, History, Experiences. Int. J. Environ. Rs. Public Health, 17, 4134 (2020).

Bossew, P., Petermann E. What is the objective of radon abatement policy? Revisiting the concept of radon priority areas. 15th GARRM. International workshop on the geological aspects of radon risk mapping. 21 – 24 Sept 2021, Prague, Czech Republic

Bossew P., Suhr N. European radon abatement policy: state and ongoing discussion. Brazilian Journal of Radiation Sciences 11-1A (Suppl.) (2023) DOI: https://doi.org/10.15392/2319-0612.2023.2162; https://bjrs.org.br/revista/index.php/REVISTA/article/view/2162

Cannelli, V., Piersanti, A., Spagnuolo, E. Galli, G. Preliminary analysis of radon time series before the MI=6 Amatrice earthquake: possible implications for fluid migration. Annals of Geophysics, 59, fast track 5 (2016). doi:10.4401/ag-7166

Cinelli, G., Tositti, L., Capaccioni, B. et al. Soil gas radon assessment and development of a radon risk map in Bolsena, Central Italy. Environ Geochem Health 37, 305–319 (2015). https://doi.org/10.1007/s10653-014-9649-9

Cinelli, G., Tollefsen, T., Bossew, P., Gruber, V., Bogucarskis, K., De Felice, L., De Cort, M., 2019. Digital version of the European Atlas of natural radiation. J. Environ. Radioact. 196, 240–252. https://doi.org/10.1016/J.JENVRAD.2018.02.008.

Ciotoli, G., Voltaggio, M., Tuccimei, P., Soligo, M., Pasculli, A., Beaubien, S.E., Bigi, S. Geographically weighted regression and geostatistical techniques to construct the geogenic radon potential map of the Lazio region: a methodological proposal for the European atlas of natural radiation. J. Environ. Radioact. 166, 355–375 (2017).

Ciotoli, G., Procesi, M., Etiope, G. et al. Influence of tectonics on global scale distribution of geological methane emissions. Nat Commun 11, 2305 (2020). https://doi.org/10.1038/s41467-020-16229-1

Coletti C., Ciotoli G, Benà E., Brattich E., Cinelli G., Galgaro A., Massironi M., Mazzoli M., Mostacci M., Mozzi P., Nava J., Ruggiero L., Sciarra A., Tositti L., Sassi R. The Geogenic Radon Potential by using the Empirical Bayesian Regression Kriging. The Euganean Hills district (Italy). Science of Total Environment 808, 152064, (2022). doi: 10.1016/j.scitotenv.2021.152064.

Decreto Legislativo 31 luglio 2020, n. 101 (Attuazione Direttiva 2013/59/EURATOM), Gazzetta Ufficiale della Repubblica Italiana, Serie Generale n. 201 del 12-08-2020- Suppl. Ordinario n. 29.

Di Toro, G., Niemeijer, A., Tripoli, A., Nielsen, S., Di Felice, F., Scarlato, P., Spada, G., Alessandroni, R., Romeo, G., Di Stefano, G., Smith, S., Spagnuolo, E., Mariano, S. From field geology to earthquake simulation: a new state-of-the-art tool to investigate rock friction during the seismic cycle (SHIVA). Rend. Fis. Acc. Lincei, 21 (Suppl 1): S95-S114 (2010). doi 10.1007/s12210-010-0097-x.

Elio J, Janik M., Bossew P. A contribution to the current debate about the adequacy of the linear-no threshold hypothesis (LNT). Rap Conference Proceedings, Vol. 8, pp. 1–4, 2023. ISSN 2737-9973 (online). doi: 10.37392/rapproc.2023.00. Rap-proceedings.org

Environmental Protection Agency. Radon Reference Manual. 1987. Report No.: EPA 520/1-87-20.

Environmental Protection Agency, 2023. Available from: https:// www.epa.gov/radiation/radiation-sources-and-doses

European Union, Council Directive 2013/59/Euratom of 5 December 2013 laying down basic safety standards for protection against the dangers arising from exposure to ionising radiation, and repealing Directives

89/618/Euratom, 90/641/Euratom, 96/29/Euratom, 97/43/Euratom and 2003/122/Euratom. Official J. Eur. Union, OJ L13, 17.01.2014 (2013) 1–73. Official J. Eur. Union, OJ L13, 17.01.2014 (2013) 1–73.

Ferlay J., Colombet M., Soerjomataram I., Mathers C., Parkin D.M., Piñeros M., Znaor A., Bray F. Estimating the Global Cancer Incidence and Mortality in 2018: GLOBOCAN Sources and Methods. Int. J. Cancer. 2019; 144:1941–1953. doi: 10.1002/ijc.31937.

Gaskin J, Coyle D, Whyte J, Krewksi D. Global Estimate of Lung Cancer Mortality Attributable to Residential Radon. Environ Health Perspect. 2018 May 31;126(5):057009. doi: 10.1289/EHP2503. PMID: 29856911; PMCID: PMC6072010.

Ghosh, D., Deb, A., Sengupta, R. Anomalous radon emission as precursor of earthquake. Journal of Applied Geophysics. 69, 67-81 (2009) https://doi.org/10.1016/j.jappgeo.2009.06.001

Giustini F., Ciotoli G., Rinaldini A., Ruggiero L., Voltaggio M. (2019) Mapping the geogenic radon potential and radon risk by using Empirical Bayesian Kriging regression: A case study from a volcanic area of central Italy. Science of the Total Environment, vol. 661, 449-464. DOI: 10.1016/j.scitotenv.2019.01.146.

Radon. In: IARC Monogr Eval Carcinog Risk Hum. Lyon, France: International Agency for Research on Cancer; 1988. P. 43: 173-259. (Monographies Evaluating Carcinogenic Risks to Humans)

Istituto Superiore di Sanità (2019) Effects on human health: https://radon.iss.it/category/effetti-sulla-salute/

Iwata, D., Nagahama, H., Muto, J. et al. Non-parametric detection of atmospheric radon concentration anomalies related to earthquakes. Sci Rep 8, 13028 (2018). https://doi.org/10.1038/s41598-018-31341-5

Jordan, T.H., et al. Operational earthquake forecasting: state of knowledge and guidelines for utilisation. Ann. Geophys. - Italy, 54, 319-391 (2011).

Koike, K., Yoshinaga, T. & Asaue, H. Radon concentrations in soil gas, considering radioactive equilibrium conditions with application to estimating fault-zone geometry. Environ. Geol., 56, 1533-1549 (2009)

Lammerer B., Selverstone J., Franz G. (2011). Field trip to the Tauern Window region along the TRANSALP seismic profile, Eastern Alps, Austria. The Geological Society of America, Field Guide 22.

Li P., Sun Q., Xue L., Geng J., Jia H., Luo T., Zheng X. (2023). Pore structure evolution and radon exhalation characteristics of sandstone after loading and unloading. International Journal of Rock Mechanics and Mining Sciences, Vol. 170, 105502, ISSN 1365-1609, https://doi.org/10.1016/j.ijrmms.2023.105502.

Li, P., Sun, Q., Hu, J. et al. Effect of the pore structure of granite and gabbro after heat treatment on the radon emission rate. Environ Sci Pollut Res 29, 36801–36813 (2022). https://doi.org/10.1007/s11356-021-18152-4

Liu, L., Chen, Z., Li, Y., Liu, Z., Hu, L., Wang, X., et al. (2023). Emission of Rn and CO2 from soil at fault zones caused by seismic waves. Earth and Space Science, 10, e2023EA003012. https://doi.org/10.1029/2023EA003012

Lüschen E., Borrini D., Gebrande H., Lammerer B., Millahn K., Neubauer F., Nicolich R. (2006). TRANSALP–deep crustal Vibroseis and explosive seismic profiling in the Eastern Alps: Tectonophysics, 414, 9–38.

Minach, L., Verdi, L., Marchesoni, C., Amadori, C. Radon in Alto Adige. Agenzia per la Protezione dell'Ambiente di Bolzano, Laboratorio di chimica fisica, (1999).

Mollo, S., Tuccimei, P., Heap, M.J., Vinciguerra, S., Soligo, M., Castelluccio, M., Scarlato, P. & Dingwell, D.B. Increase in radon emission due to rock failure: an experimental study. Geophys. Res. Lett., 38, L14304, (2011) doi:10.1029/2011GL047962.

Müller W., Mancktelow Ns., Meir M. (2000). Rb-Sr microchrons of synkinematic mica in mylonites: an example from the DAV fault in Eastern Alps. Earth Planet. Sci. Lett., 1880, 385-397.Nazaroff, W. W.: Radon transport from soil to air, Rev. Geophys., 30, 137–160, 1992. https://doi.org/10.1029/92RG00055

Nazaroff, W.W. and Nero Jr., A.V. (Eds.) (1988) Radon and Its Decay Products in Indoor Air. Wiley, New York, 65-69.

M., Neznal, M., Matolin, M., Barnet, I., Miksova, J., 2004. The new method for assessing the radon risk of building sites. Czech Geol. Survey Special Papers. 16. Czech Geol. Survey.

Pásztor, L., Szabó, K.Z., Szatmári, G., Laborczi, A., Horváth, Á., 2016. Mapping geogenic radon potential by regression kriging. Sci. Total Environ. 544, 883–891.

Perko T., Martell M., Rovenska K., Fojtikova I., Paridaens J., Geysmansr. (2022): Report on review and analysis of national radon action plans and their implementation, updated intermediate report, D2 (updated): SCK CEN, MERIENCE, SURO for EC DG Energy; EU-RAP project, Ref. Ares (2020)2496502 (no public access).

Petermann, E., Bossew, P., Hoffmann, B. Radon hazard vs. radon risk – on the effectiveness of radon priority areas. Journal of Environmental Radioactivity 244-245, 106833 (2022).

Petermann, E., Meyer, H., Nussbaum, M., Bossew, P. Mapping the geogenic radon potential for Germany by machine learning. Science of Total Environment, 754 – 142291, 2021. https://doi.org/10.1016/j.scitotenv.2020.142291

Riudavets, M.; Garcia de Herreros, M.; Besse, B.; Mezquita, L. Radon and Lung Cancer: Current

Trends and Future Perspectives. Cancers 2022, 14, 3142. https://doi.org/10.3390/cancers14133142

Ruano-Ravina, A., Martin-Gisbert, L., Kelsey, K. et al. An overview on the relationship between residential radon and lung cancer: what we know and future research. Clin Transl Oncol 25, 3357–3368 (2023). https://doi.org/10.1007/s12094-023-03308-0

Sassi F.P., Cesare B., Mazzoli C., Peruzzo L., Sassi R., Spiess R. (2004). The crystalline basements of the Italian Eastern Alps: a review of the metamorphic features. In: Castelli D. and Cesare B. (Eds.) "Advances in Metamorphic Petrology: browsing through Italian classic areas, case studies, and approaches", Per. Mineral. Special Issue 2, 23-42. ISSN: 0369-8963.

Scarlato, P., Tuccimei, P., Mollo, S., Soligo, M., and Castelluccio, M. Contrasting radon background levels in volcanic settings: Clues from 220Rn activity concentrations measured during long-term deformation experiments, Bull. Volcanol., 75, 751 (2013). doi:10.1007/s00445-013-0751-0, 2013.

Schmid S.M., Aebli H.R., Heller F., Zinng A. (1989). The role of the Periadriatic Line in the tectonic evolution of the Alps. Geol. Soc. London, Spec. Publ., 45, 153-171.

Schmid S.M., Fügenschuh B., Kissling E., Schuster R. (2004). Tectonic map and overall architecture of the Alpine orogen. Eclogae Geol. Helv., 97, 93-117.

Spiess R., Cesare B., Mazzoli C., Sassi R., Sassi F.P. (2010). The crystalline basement of the Adria microplate in the eastern Alps: a review of the palaeostructural evolution from the Neoproterozoic to the Cenozoic. Rend. Fis. Acc. Lincei, 21, (Suppl 1), 31-50, doi:10.1007/s12210-010-0100-6

The Cancer Atlas (2019), AIRC, WHO, ISBN 978-1-60443-265-7, Rdited by Jemal A, Torre L, Soerjomataram I, Bray F, editors.

Tuccimei, P., Mollo, S., Vinciguerra, S., Castelluccio, M., Soligo, M. Radon and thoron emission from lithophysae-rich tuff under increasing deformation: an experimental study. Geophys. Res. Lett., 37, L05305 (2010). doi:10.1029/2009GL042134.

Verdi, L. Weber, A. Stoppa, G. Indoor radon concentration forecasting in South Tyrol. Radiation Protection Dosimetry, 111(4), pp. 435 438 (2004)

Walia, V., Kumar, A., Chowdhury, S. et al. Earthquake precursory study using decomposition technique: time series soil radon monitoring data from the San-Jie Station in Northern Taiwan. J Radioanal Nucl Chem (2023). https://doi.org/10.1007/s10967-023-09187-7

Wakita H., Nakamura Y., Notsu K., Noguchi M, and Asada T. (1980). Radon Anomaly: A Possible Precursor of the 1978 Izu-Oshima-kinkai Earthquake. Science, Vol 207, Issue 4433, pp. 882-883. DOI: 10.1126/science.207.4433.882

Wakita, H. Geochemical challenge to earthquake prediction. Proc. Natl. Acad. Sci. U.S.A., 93, 3781-3786 (1996)

Wang, X., Li, Y., Du, J., Zhou, X. Correlations between radon in soil gas and the activity of seismogenic faults in the Tangshan area, North China. Radiat. Meas., 60, 8-14 (2014)

Zeeb, H. & Shannoun, F. (eds.). WHO handbook on indoor radon - a public health perspective (2009). ISBNS 978 92 4 154767. https://www.who.int/publications/i/item/9789241547673

3. Chapter 1:

Evaluation of tectonically enhanced radon in faulted zone by quantification of the radon activity index

Abstract

This work highlights the importance of the Geogenic Radon Potential (GRP) component originated by degassing processes in fault zones. This Tectonically Enhanced Radon (TER) can increase radon concentration in soil gas and the inflow of radon in the buildings (Indoor Radon Concentrations, IRC). Although tectonically related radon enhancement is known in areas characterised by active faults, few studies have investigated radon migration processes in non-active fault zones. The Pusteria Valley (Bolzano, north-eastern Italy) represents an ideal geological setting to study the role of a non-seismic fault system in enhancing the geogenic radon. Here, most of the municipalities are characterised by high IRC. We performed soil gas surveys in three of these municipalities located along a wide section of the non-seismic Pusteria fault system characterised by a dense network of faults and fractures. Results highlight the presence of high Rn concentrations (up to 800 kBq·m^{-3}) with anisotropic spatial patterns oriented along the main strike of the fault system. We calculated a Radon Activity Index (RAI) along north-south profiles across the Pusteria fault system and found that TER is linked to high fault geochemical activities. This evidence confirms that TER constitutes a significant component of GRP also along non-seismic faults.

Benà, E.[1], Ciotoli, G.[2,3], Ruggiero, L.[3], Coletti, C.[1], Bossew, P.[4], Massironi, M.[1], Mazzoli, C.[1], Mair, V.[5], Morelli, C.[5], Galgaro, A.[1], Morozzi, P.[6], Tositti, L.[6], Sassi, R.[1]

[1]Department of Geosciences, University of Padova, Italy
[2]Istituto di Geologia Ambientale e Geoingegneria (IGAG-CNR), Rome, Italy
[3]Istituto di Geofisica e Vulcanologia (INGV), Rome, Italy
[4]Federal Office for Radiation Protection (BfS), Section Radon and NORM, Berlin, Germany (retired)
[5]Office for Geology and Building Materials Testing, Autonomous Province of Bolzano, Italy
[6]Department of Chemistry "G. Ciamician", University of Bologna, Italy

A slightly different version of this chapter is published in *Scientific Reports* (Benà et al., 2022).

Authorship contribution statement:
E.B. Conceptualization, RAD7 analysis, data curation, mapping, writing - original draft preparation, reviewing and editing; **G.C.** conceptualization, geostatistics and mapping, RAD7 analysis, writing - reviewing and editing; **L.R.** mapping, conceptualization, RAD7 analysis, reviewing and editing; **C.C.** RAD7 analysis, reviewing and editing; **P.B.** conceptualization, reviewing and editing; **M.M**. reviewing and editing; **C.M.** reviewing and editing; **V.M.** reviewing and editing; **C.M.** conceptualization, reviewing and editing; **A.G.** reviewing and editing; **P.M.** gamma spectrometry; **L.T.** gamma spectrometry, reviewing and editing; **R.S.** Project administration, Supervision, Funding acquisition, RAD7 analysis, Reviewing and Editing.

3.1. Introduction

Radon (^{222}Rn) is considered the dominant source of human exposure to ionising radiation. Being a natural radioactive gas, epidemiological studies provided evidence for a marked increased risk of lung cancer associated with long-term exposure also to relatively low Indoor Radon Concentrations (IRC), as well as to its decay products (Field, 2018). As a consequence, the World Health Organization (WHO) classified radon as the second leading cause of lung cancer after cigarette smoking (WHO, 2009). IRC in buildings is the main target variable of current regulations (EURATOM/59/2013; Coletti et al., 2020); however, this parameter is controlled by soil-gas radon concentration, which is commonly assumed to be primarily correlated to the amount of uranium content in soils and rocks (geogenic radon; GR).

GR is usually quantified by the Geogenic Radon Potential (GRP) that represents "what Earth delivers in terms of radon" available to enter buildings, and it can be considered as an indicator of the susceptibility of an area to geogenic radon (Bossew, 2015). Additionally, IRC strongly depends on anthropogenic factors, namely building characteristics and usage patterns. GR is the result of two main components: Rn from the source, e.g. the radon produced from the natural radioactive decay of radionuclides in rocks, soil and groundwater (background); and migrated Rn, e.g. the radon derived from diffusion and migration processes in the subsurface, and their influence factors, mainly occurring along more permeable pathways, i.e. faults, fractures and cavities (e.g., in karst areas). Both components contribute to the amount of Rn in soil potentially available (e.g., GRP) to exhale from the ground and infiltrate into buildings (Bossew et al., 2020).

Radon transport over distance in fault zones may locally represent a significant additional contribution to the Rn background originated by radionuclide decay in the source rocks; this quantity can be defined as Tectonically Enhanced Radon (TER). TER measures the "strength" of the tectonic factor that can potentially increase the radon originated from the local lithology (and, as a consequence, can affect the potential increase of the IRC), due to:

- the action of carrier gases (e.g. CO_2, CH_4) migrating from deep sources by advection along faults (Ciotoli et al., 2007);
- the increase of rock permeability in the damage zones enveloping active faults (Fu et a., 2009; Ghosh et al., 2009; Seminsky and Demberel, 2013; Seminsky et al., 2014; Koike et al., 2014; Chen et al., Coletti et al., 2022).

Numerous studies report examples of radon migration along faults that may be ascribed to the TER concept but specific studies aimed at quantifying this geogenic component of radon are missing. However, most of these studies deal with seismic faults, in contrast to the aseismic fault system discussed in our work. Both seismic and aseismic faults can still be expected to have certain features

in common; while aseismic faults can be supposed to lack the temporal dimension of seismic faults which lead to temporally variable gas transport and exhalation. This effect is used for diagnosis and forecast in volcanology and seismic science, but not further discussed here.

For example, Ciotoli et al. (2007) investigated radon distribution in the Fucino Plain (central Italy), a tectonically active intermontane basin bordered and crossed by a complex network of deeply buried and/or shallow faults and fractures characterized by high seismic activity (e.g., magnitude 7.0, Avezzano earthquake of 13 January 1915, Oddone, 1915). In this area, radon anomalies up to 5 times the background soil production (25 $kBq \cdot m^{-3}$), occur along the main faults of the basin even when buried under thick sedimentary covers (up to 900m). Fault-related anisotropy affects radon distribution at the surface, and provides a clear correlation between the shape and orientation of radon anomalies and the geometry of the recognised damage zones in the area.

Seminsky et al. (2014) studied the variations of radon activity in the crustal fault zone of the Baikal-Mongolian seismic belt and revealed that the radon anomalies occurring along the investigated profiles crossing the Khustai fault are five times higher than the background value (3.9 $kBq \cdot m^{-3}$).

Wang et al. (2014) found radon concentrations in soil gas eight times higher than the background value (4.7 $kBq \cdot m^{-3}$) along the active Tangshan fault (Northern China). In particular, radon enhanced values in the area showed close relation with the seismic activity along fault zones. Active segments of faults and associated damage zones along which larger earthquakes nucleated may act as preferential paths for enhanced radon migration. These studies suggest that the anisotropic spatial distribution of radon anomalies along fault zones is strictly related to their orientation, geometrical complexity (i.e. single fault density vs complex fault system), seismic activity and the relation between width of the core zone and extension of the damage zone (e.g., presence of transverse faults, i.e. relay ramp, Fossen, 2016) (Fig. 1).

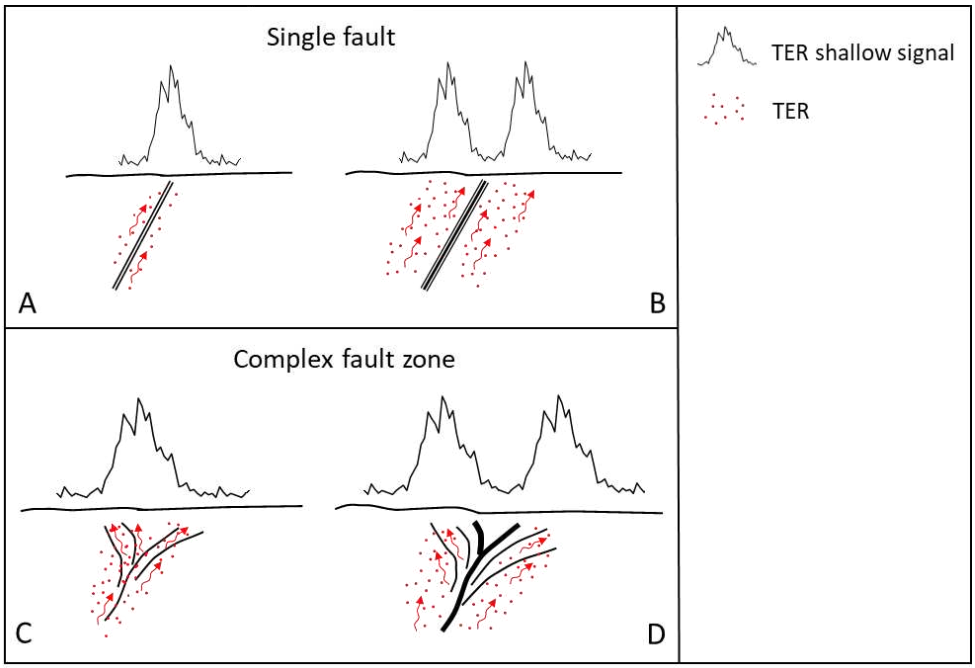

Figure 1. The figure represents the two different cases of a single fault and complex fault zone: (**A**) single fault with permeable core and damage zone, TER shallow signal is represented by a single-peak anomaly; (**B**) single fault with non-permeable core and wide and permeable damage zone, TER signal may show a double-peak anomaly; (**C**) complex fault zone with permeable core and damage zone, TER signal occurs as a single-peak; (**D**) complex fault zone with non-permeable core, and wide and permeable damage zone; TER is represented by a double-peak signal.

In this work, we focus on the analysis of the distribution and the magnitude of radon, thoron and CO_2 soil gas anomalies in the Pusteria/Pustertal Valley (north-eastern Italy, Fig. 2). This area is characterised by the Periadriatic fault system which is the aseismic tectonic boundary between the Austroalpine orogenic wedge and the Southalpine indenter in the Eastern Alps. In the study area, this non-seismic fault system is composed of three main E-W trending faults: (i) the Pusteria/Pustertal fault (PF), a sub vertical fault system that accommodated a dextral transpressive kinematics during the Alpine orogenesis since late Oligocene (Schmid and Haas, 1989; Schmid et al., 1996; Bistacchi et al., 2010; Reiter et al., 2018); (ii) the Kalkstein-Vallarga/Weitental fault (KV), a minor fault still pertaining to the same Periadriatic fault system (Sassi et al., 2004); (iii) the Deffereggen-Anterselva/Antholz-Valles/Vals line (DAV), a mylonitic shear zone marking the southern boundary of the Alpine (Paleogenic) metamorphic overprint within the Austroalpine basement (Müller et al., 2000). In the study area, the outcropping crystalline basement is composed of orthogneiss and paragneiss (Austroalpine domain) to the north of the PF, and phyllites intruded by granites (Southalpine domain) to the south of the PF (Fig. 2).

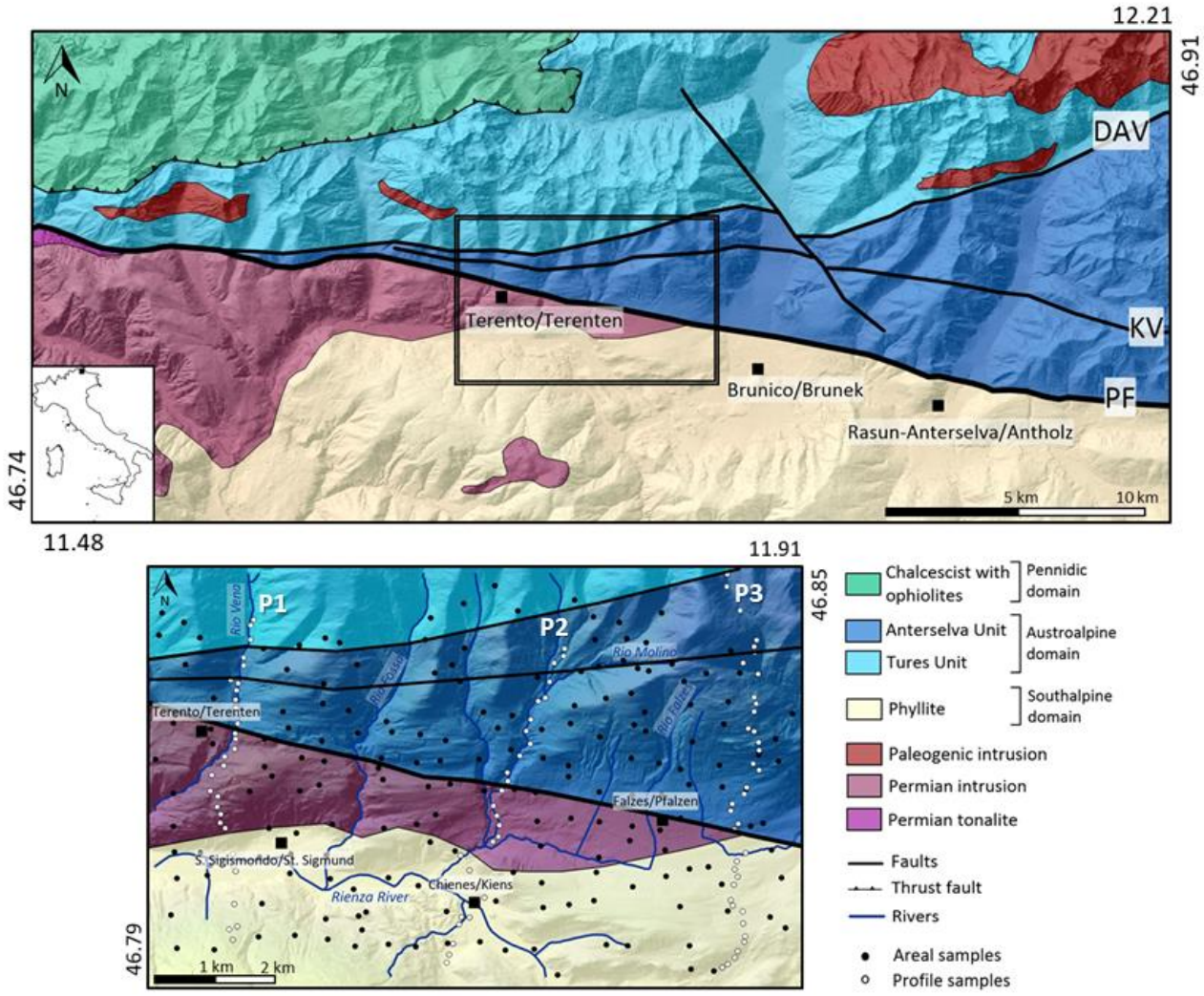

Figure 2. Geological sketch map of the Eastern Alps (**a**) (modified from Reiter et al., 2018). The study area shows the location of the soil gas samples: areal samples (in black); and profiles samples (from W to E, P1, P2, P3, in white). PF = Pusteria/Pustertal fault, KV = Kalkstein-Vallarga/Weitental fault (Schmid et al., 1996), DAV = Defferegger-Anterselva/Antholz-Valles/Vals mylonitic zone.

The main objectives of our work are: (*i*) to evaluate the potential degassing processes along a non-seismically active fault (i.e., the Pusteria fault system), (*ii*) to quantify TER in terms of a Radon Activity Index (RAI) and (*iii*) to compare RAI magnitude with those calculated for seismically active fault systems from the literature. The obtained results highlight that TER may constitute an important additional component to GRP also along aseismic fault systems, thus potentially enhancing influx of radon into buildings.

3.2. Methods

3.2.1. Structural model

The geological map (Hofmann et al., 1983) and the location of the main faults (Keim et al., 2013) are available from the Geological catalogue of Bolzano Province. The structure of the fault zone was reconstructed based on the geomorphological analysis of the Digital Terrain Model (DTM) at the resolution of 2.5 m. In particular, a detailed structural interpretation has been carried out on the hillshade derived from the DTM using ArcGIS Pro. We reclassified the recognised structures in three different classes: (*i*) main faults: including the PF and the KV faults; (*ii*) DAV: the mylonitic zone; (*iii*) minor faults (Fig. 3). The shapefile of the faults was then transformed in fault/fracture density map by using the Kernel Density algorithm (O'Sullivan, 1986) of the Spatial Analyst tools in ArcGIS Pro.

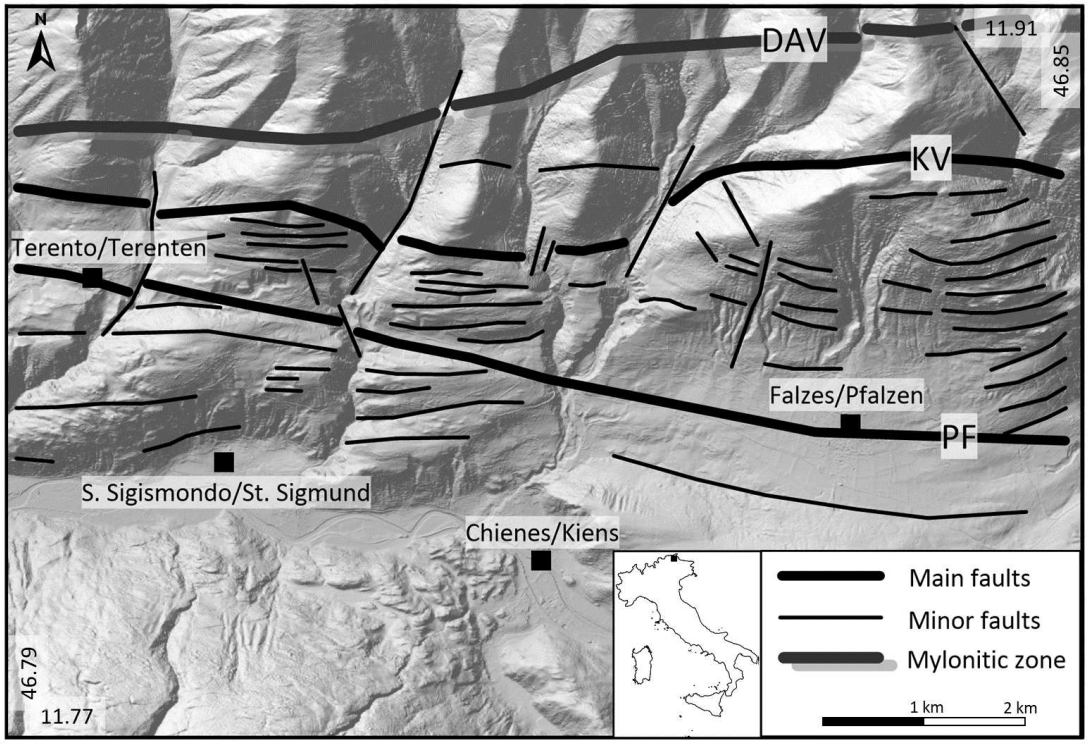

Figure 3. The structural model of the study area of the hillshade derived from the digital terrain model (DTM, 2.5 m/pixel). PF=Pusteria/Pustertal Fault; KV=Kalkstein-Vallarga/Weitental fault; DAV = Deffereggen-Anterselva/Antholz-Valles/Vals mylonitic zone.

3.2.2. Radionuclide content

A total of 14 rock samples of the main outcropping lithologies in the study area were collected as follow: gneiss (7 samples) from the Austroalpine unit; phyllite (3 samples) and Brixen granite (4 samples) from the Southalpine unit. Prior to radioactivity measurement, the rock samples were ground and mechanically sieved (<4 mm) to determine the activity concentration of natural radionuclides (^{238}U, ^{232}Th, ^{40}K) using high-resolution gamma-ray spectrometer in a suitable configuration.

Rock samples were analysed using two p-type coaxial Hyper Pure Germanium crystal detector (HPGe), a PROFILE (Ortec-Ametek Inc.) with an extended energy range (20-2000 keV) and a GEM model (Ortec-Ametek Inc.) with an energy range 80-2000 keV. These detectors have relative efficiency of 20% and 38%, and resolution (FWHM) at 1322.5 keV of 1.9 keV and 1.8 keV, respectively. Both systems were calibrated for energy and efficiency using liquid standard solutions (Eckert and Ziegler Multi-nuclide standard solution 7501) in a jar geometry (diameter = 56 mm; thickness = 10 mm). Spectra of the rock samples were acquired for one day to optimize peak analysis and subsequently processed and analysed using the Gamma Vision-32 software package (version 6.07, Ortec-Ametek). ^{226}Ra was determined at 186 keV correcting the peak area by the ^{235}U interference according to the method proposed by Gilmore (2008), under the hypothesis of secular equilibrium between ^{226}Ra-^{238}U and natural ^{235}U/^{238}U isotopic ratio. ^{238}U and ^{232}Th were then determined using the emission of their radioactive daughters ^{226}Ra and ^{228}Ac. Data validation and quality control was carried out analysing a series of certified reference materials (CRMs) in the same geometry as the unknown samples and calibration standard. The CRMs used, in the solid phase, were: IAEA-412 Pacific Ocean Sediment, UTS-3 (Canmet) and Dh1-a (Canmet). Minimum detectable activity (CRMDA) was determined using the Traditional ORTEC method (ORTEC, 2003) with a peak cut-off limit of 40%. Conversion from specific activity (Bq·kg^{-1}) to bulk elemental weight fraction was obtained with the following conversion factors (Stromswold, 1995):

- 1% K = 309.7 Bq·kg^{-1}
- 1 ppm U = 12.35 Bq·kg^{-1}
- 1 ppm Th = 4.072 Bq·kg^{-1}

The radon background production (as well as the geochemical anomaly threshold) has been calculated using the ^{222}Rn activity at equilibrium with parent radionuclides (^{226}Ra) in collected rock samples, using the Akerblom formula (Eq. 1, Akerblom, 1993):

Eq. 1

$$C_{Rn} = C_{Ra}\varepsilon\rho n^{-1}$$

where C_{Rn} and C_{Ra} are radon in soil gas (Bq·L^{-1}) and radium in soil (Bq·kg^{-1}), respectively, ε is the emanation power coefficient (dimensionless), ρ is soil density (kg·L^{-1}), and n is the effective porosity coefficient (dimensionless). The emanation power coefficient has been calculated as one minus the ratio between the mean activity concentration of radon decay products ^{214}Pb and ^{214}Bi with respect to the parent ^{226}Ra (Nuccetelli, 2008; Capaccioni et al., 2012). We have assumed that ρ = 2.7 g·cm^{-3} and n = 0.4.

3.2.3. Soil gas sampling

Soil gas surveys were performed in July 2021 to ensure stable meteorological conditions. A total of 278 soil gas samples have been collected in an area of about 60 km^2 according to a 500m x 500m grid and along 3 north-south profiles (from W to E, P1, P2, P3) crossing the fault zone with a sampling step of about 100 m, in the municipalities of Terento/Terenten (western sector), Chienes/Kiens (central sector) and Falzes/Pfalzen (eastern sector).

We collected the soil gas samples using a 6.4 mm thick-walled stainless-steel probe pounded in the ground by a co-axial hammer at a depth of about 0.8-1 m to minimise as much as possible the influence of meteorological parameters that may affect the air exchange at the soil-atmosphere boundary. Soil gas measurements were conducted using a portable multi-gas analyser (Draeger X-am 7000, Drägerwerk AG&Co. KGaA) connected to the probe with a silicon tube for the simultaneous analyses of carbon dioxide (CO_2, range 0-100%), methane (CH_4, range 0-100% LEL), hydrogen (H_2, range 0-600 ppm), hydrogen sulphide (H_2S, range 0-1000 ppm) and oxygen (O_2, range 0-21%).

Radon (^{222}Rn) and thoron (^{220}Rn) measurements were conducted using RAD7 (Durridge Company, Inc) alpha detector (±5% absolute accuracy, and a sensivity of 0.25 cpm/(pCi/L) 0.0067 cpm/(Bq·m^{-3}). The alpha detector is connected with the sampling probe and with a drying tube (filled with $CaSO_4$, drierite) for maintaining the relative humidity (HR) below 10%. Results were managed and correct for relative humidity (HR) by means the specific RAD7 Data Acquisition and Analysis Software Capture® (Durridge). Each measurement of radon and thoron activity is performed with 5-min integration time, and is repeated until the difference between the last two measurements is at least below 5-10%. The final result was determined by taking the average of the last two integrations (Ciotoli et al., 2016).

3.2.4. Statistical and Geospatial analyses

Collected data have been processed using: Exploratory Data Analysis (EDA) and Geostatistical Analysis (GA).

EDA was performed to evaluate the basic characteristics of the data and their statistical distribution by using numerical (i.e., calculation of summary statistics and statistical distribution of each variable) and graphical methods (i.e., histograms, box plots and normal probability plots). In particular, we used the Normal Probability Plots (NPP) to determine the occurrence of different overlapping geochemical populations and define threshold values by approximating linear segments on the point

distribution in the graph (Nuccetelli, 2008). The identification of sharp deviations or gaps in the NPP may indicate the presence of subpopulations (e.g., background and/or anomalies) separated by a threshold value (Sinclair, 1991; Ascione et al., 2018; Giustini et al., 2022).

GA was performed to understand and reconstruct the natural phenomena that govern the spatial behaviour of the studied variables. In particular, we used GA to visualise the samples distribution and the distribution of the measured values compared to their nearest neighbours, to study the spatial autocorrelation of the variables and elaborate a spatial model in order to estimate the variable values at unsampled locations and construct final prediction maps. We accomplished this process according to the following steps:

1. Construction of experimental variograms of the studied variables. In particular experimental variograms and variogram surfaces were used to check the spatial continuity of the data distribution values and the presence of anisotropic phenomena (i.e., fault-related) acting along preferential directions;
2. Determination of the anisotropy (where present) which is important for defining parameters for the kriging estimation (i.e., directions and anisotropy ratio);
3. Construction of a spatial model, i.e., calculation of the main variogram parameters (nugget, range, sill) to be used in the kriging algorithm;
4. Preparation and validation of prediction maps (i.e., contour maps) by using Ordinary Kriging (OK) algorithm (Ciotoli et al., 2014).

Collected data were processed using the following software: ArcGIS Pro 2.7.0 (copyright 2020@Esri Inc.) and Surfer 23.1.162 (copyright 1993-2021, Golden Software, LLC) for the mapping process; Grapher 19.1.288 (copyright 1992-2021, Golden Software, LLC) and Statistica12 (copyright Statsofts. Inc.) software for the numerical and graphical statistics.

3.2.5. RAI Calculation

To quantify the Tectonically Enhanced Radon (TER) we have applied the concept of Radon Activity Index (RAI). Over the years, many systems for classification radon concentration in soil gas have been elaborated to mathematically explain the geochemical activity of a fault zone. Seminsky et al. (2014) proposed the relative index of radon activity K_Q calculated as the ratio of the maximum ^{222}Rn concentration (Q_{max}) to the minimum ^{222}Rn concentration outside the fault zone (Q_{min}) for the classification of fault activity. Then, the values have been divided into five different levels of activity. Inspired by this study, we have modified the concept of the index of radon activity, considering a Radon Activity Index (RAI) calculated as the ratio between the maximum ^{222}Rn value along the measured or estimated radon profiles to the background value (50 $kBq \cdot m^{-3}$) estimated over the area

with the NPP method (see section geostatistical and spatial analysis in methods). We have calculated the RAI considering only the radon peaks (radon values above the background threshold) relative to 21 (P4 to P24) estimated profiles, obtained by intersecting the radon grid map with 6 km long N-S sections (using Profile, Map Tools in Surfer 23.1.162) with a sampling step of 10 m and spaced 500 m from each other. Applying this method, each profile is composed of 600 estimated points of measurement ensuring good statistic representativeness.

Based on the results obtained by RAI calculation (see Appendix 1, Table A1), the values have been divided into four classes of geochemical activity:

i. RAI < 2: low activity;
ii. 2 < RAI < 3: medium activity;
iii. 3 < RAI < 6 high activity;
iv. RAI > 6 very high activity;

The location of the RAI values is reported as classed post in a bivariate colour map (summary sketch map in Fig. 5) obtained using the bivariate colours option in ArcGIS Pro. The different colours in the bivariate map represent different values of the first (RAI) and the second (fault density) variable simultaneously.

3.3. Results

^{222}Rn and thoron (^{220}Rn) activities, CO_2 and O_2 concentrations were measured directly in the field at 278 sites according to a regular grid and along three N-S profiles crossing the aseismic Pusteria fault system, over an area of about 60 km^2.

Table 1 shows descriptive statistics (i.e., main numerical indexes) of all the studied gases. The significance of Kolmogorov-Smirnov test ($p<0.01$) confirms the non-normal distribution of all the variables (measured on the grid and along the three profiles), especially those of ^{222}Rn, ^{220}Rn and CO_2 which showed a skewed distribution (see Appendix 1, Fig. A1a).

Descriptive statistics on the total dataset (A) highlights that ^{222}Rn ranges between 1.54 and 815.96 $kBq \cdot m^{-3}$. We considered the similarity between median (36.52 $kBq \cdot m^{-3}$) and geometric mean (GM) (35.16 $kBq \cdot m^{-3}$ as a representative indicator of the approximately log-normal distribution of the variables, since median is not influenced by the presence of outliers and GM is the mean value of the log-transformed data. ^{220}Rn values range between 1.04-102.07 $kBq \cdot m^{-3}$ with a median of 15.46 $kBq \cdot m^{-3}$ and a GM of 14.55 $kBq \cdot m^{-3}$. CO_2 measurements range between 0.20% v/v and 16.00% v/v with a median of 1.71% v/v and GM equal to 1.78% v/v.

Descriptive statistics of the three profiles showed that ^{222}Rn varies between 7.65-253.24 kBq·m^{-3} (P1), 13.71-186.20 kBq·m^{-3} (P2) and 6.76-448.76 kBq·m^{-3} (P3). The GM values are 29.74 kBq·m^{-3} (P1), 50.88 kBq·m^{-3} (P2) and 33.80 kBq·m^{-3} (P3), respectively. ^{220}Rn values range 5.70-37.02 kBq·m^{-3} (P1), 5.23-41.66 kBq·m^{-3} (P2) and 1.04-47.54 kBq·m^{-3} (P3). The GM values are 18.57 kBq·m^{-3} (P1), 15.79 kBq·m^{-3} (P2) and 9.79 kBq·m^{-3} (P3). CO_2 concentrations range between 0.60-10.80% v/v (P1), 0.60-6.20% v/v (P2), and 0.30%-5.80% v/v (P3). The respective GM are equal to 2.03% v/v (P1), 2.43% v/v (P2) and 1.29% v/v (P3).

It is worth noting that maximum ^{222}Rn value (815.96 kBq·m^{-3}), as well as values measured along the three profiles (253.24 kBq·m^{-3}, 186.20 kBq·m^{-3} and 448.76 kBq·m^{-3} for P1, P2 and P3, respectively) are among the highest values measured in active tectonic areas in Italy, based on more than 30,000 data collected in Central and Southern Italy (Ciotoli et al., 2016).

The normal probability plots (see Appendix 1, Fig. A1b) describe both the background values and the anomaly thresholds of the different gas species: 50 kBq·m^{-3} for ^{222}Rn, 15 kBq·m^{-3}for ^{220}Rn and 4% v/v for CO_2.

	Soil data	N	Mean	CI-95%	CI+95%	GM	Min	Max	LQ	UQ	Std.Dev	SK	Median
A	^{222}Rn	278	67.44	55.15	79.74	35.16	1.54	815.96	15.36	78.61	104.11	4.46	36.52
	^{220}Rn	272	17.60	16.21	18.98	14.55	1.04	102.07	9.78	22.82	11.62	2.70	15.46
	CO_2	277	2.51	2.24	2.79	1.78	0.20	16.00	1.00	3.40	2.30	2.13	1.71
	O_2	236	18.06	17.70	18.43	17.71	3.10	20.60	17.30	19.85	2.85	-2.43	19.10
P1	^{222}Rn	17	55.78	20.33	91.22	29.74	7.65	253.24	10.33	53.78	68.94	1.84	24.73
	^{220}Rn	17	21.00	15.95	26.05	18.57	5.70	37.02	14.59	30.88	9.81	0.18	20.59
	CO_2	17	2.79	1.41	4.17	2.03	0.60	10.80	1.00	3.20	2.68	2.15	1.80
	O_2	17	17.76	16.14	19.38	17.38	7.60	20.20	16.80	19.80	3.15	-2.42	19.10
P2	^{222}Rn	21	66.10	45.37	86.83	50.88	13.71	186.20	33.54	87.39	45.53	0.97	54.51
	^{220}Rn	20	18.19	13.54	22.85	15.79	5.23	41.66	10.97	22.17	9.95	1.02	15.92
	CO_2	21	2.89	2.19	3.59	2.43	0.60	6.20	1.40	3.80	1.54	0.32	3.00
	O_2	21	17.29	16.24	18.34	17.13	12.10	20.20	16.40	19.10	2.31	-0.84	17.50
P3	^{222}Rn	24	68.83	24.63	113.04	33.80	6.76	448.76	16.05	75.11	104.69	2.68	27.54
	^{220}Rn	23	12.44	8.34	16.54	9.79	1.04	47.54	6.61	15.74	9.48	2.43	9.75
	CO_2	24	1.68	1.11	2.25	1.29	0.30	5.80	0.80	2.30	1.35	1.79	1.20
	O_2	24	19.15	18.50	19.80	19.08	13.20	20.40	18.90	20.05	1.53	-2.83	19.65

Table 1. Descriptive statistics of soil gas data. A = Total dataset; P1, P2, P3 = profiles; N = Number of samples; Mean; CI (-95% – +95%) = Confidence interval of the mean; GM = Geometric mean; Min = Minimum value; Max = Maximum value; LQ = Lower quartile; UQ = Upper quartile; Std.Dev. = Standard deviation; SK = Skewness; Median.

We applied the Akerblom formula (Akerblom, 1993) to calculate the radon at equilibrium with the activity concentration of the ^{226}Ra (its direct parent radionuclide) in the main outcropping lithologies. The formula provides ^{222}Rn mean values of 83.5 kBq·m^{-3} for the Austroalpine gneiss, 68.3 kBq·m^{-3} for the Permian granite and 27.7 kBq·m^{-3} for the Southalpine phyllite, respectively (see Appendix 1, Table A2). The mean value of 59.8 kBq·m^{-3} agrees with that obtained by the NPP (Normal Probability Plots; see Appendix 1, Fig. A1b).

Variogram analysis has been performed on ^{222}Rn, ^{220}Rn and CO_2 data which were log-transformed to minimise the effect of outliers (Beaubien et al., 2002; Astorri et al., 2002; Annunziatellis et al., 2008). The experimental variograms were calculated along four directions to highlight the presence of anisotropies (e.g., fault related gas anomalies) in the spatial distribution of the data. In general, all gases showed a clear anisotropic behaviour along the E-W direction. The experimental variograms calculated along the maximum axes of the anisotropy ellipse showed correlations consistent with the main directions of faults and fractures. In particular, the main anisotropy directions are about 90° for ^{222}Rn, 50° for ^{220}Rn and 95° for CO_2 (see Appendix 1, Fig. A2). Variogram models were used within the ordinary kriging algorithm to predict values at unsampled locations and construct gas distribution maps. According to the maximum anisotropy axis discussed above, ^{222}Rn anomalies well fit the E-W trend of the Periadriatic system from the DAV line, to the north, to the PF, to the south (Fig. 4a). This trend also follows the direction of the brittle fracture zone between the main faults, which includes conjugate minor faults and fractures roughly parallel to the main faults (Massironi et al., 2011; Bistacchi et al., 2012).

The highest anomalous values (> 100 kBq·m^{-3} and up to 800 kBq·m^{-3}) occur in the eastern sector (municipality of Falzes/Pfalzen). This area shows the highest radon values up to 815.96 kBq·m^{-3}. In contrast, the plain area south of the PF displays the lowest radon values, below the background (< 50 kBq·m^{-3}). The lowest ^{220}Rn values (< 30 kBq·m^{-3}) have been measured in the fracture zone between the DAV and PF, while the highest ones occur to the south of PF corresponding to the western sector (Terento/Terenten municipality) (Fig. 4b).

The distribution of CO_2 anomalies (> 4% v/v) also follows the E-W trend of the PF (maximum anisotropy axis = 95°) (Fig. 4c). The area south of the PF shows a CO_2 anomaly greater than 4% in the municipality of Chienes/Kiens; in contrast, the easternmost sector of the study area only reports low CO_2 concentration values.

In general, the most fractured sector between DAV and PF shows higher values of ^{222}Rn with respect to neighbouring zones. It is worth noting that ^{222}Rn and CO_2 anomalies coincide along the PF, whereas CO_2 displays high values also south of the PF.

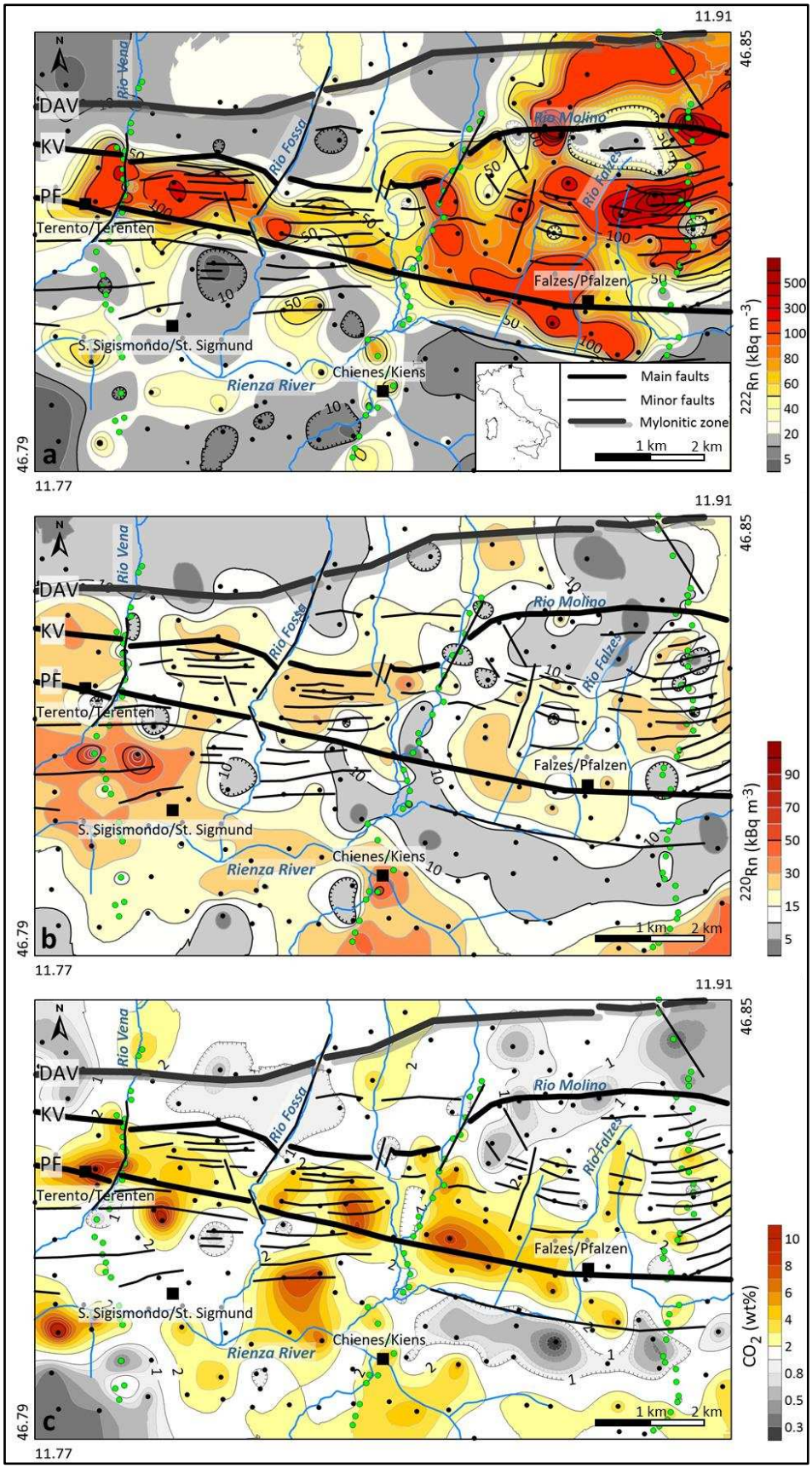

Figure 4. Contour maps of (**a**) ^{222}Rn, (**b**) ^{220}Rn and (**c**) CO_2 of the study area. In the maps the structural model of the study area is also reported, with the interpreted structures divided into: main faults (PF = Pusteria/Pustertal Fault and KV = Kalkstein-Vallarga/Weitental fault); minor faults; Mylonitic zone (DAV = Defferegger-Anterselva/Antholz-Valles/Vals mylonitic zone). The coloured points represent the location of the soil-gas measurements: areal sampling in black and the three profiles (from W to E, P1, P2, P3) in green.

3.4. Discussion

We performed morphological analysis from the DTM (2.5 × 2.5 m Digital Terrain Model) in order to reconstruct a structural model of the area. The model highlights a series of minor faults and fractures located among the main faults in the area (PF, KV line and DAV). This structural network includes the potentially permeable pathways for gas advection.

As widely reported in the literature, radon generated by ^{238}U decay in rocks and soil can escape by diffusion from the surface and accumulate/disperse at shallow depth in soils, or migrate by advection upwards at greater distance from deeper sources along preferential pathways, such as faults and fractures, transported by gas carriers (CO_2, CH_4, etc.) (Baubron et al., 2002; Yanga et al., 2005; Ciotoli et al., 2007, 2016). Meteorological parameters (e.g., pressure, humidity, temperature) can also affect the distribution of radon in shallow soil, but they cannot explain the sharp anisotropy of the radon distribution along the fault strike (Walia et al., 2009; Cinelli et al., 2019).

In this study area, ^{222}Rn and CO_2 anomalies generally well fit with the main orientation of the Periadriatic fault system. However, despite both gases show the same anisotropy ratio (R = 2), as observed in the experimental variograms (see Appendix 1, Fig. A2), ^{222}Rn anomalies show higher spatial continuity compared to CO_2. As a result, the spatial distribution of ^{222}Rn and CO_2 concentrations show different patterns characterised by elongated anomalies, and aligned spot anomalies, respectively, as also elsewhere observed by Ciotoli et al. (2007).

The extent and the elongation of radon anomalies spatially changes from a sharp (narrowly elongated anomalies) pattern in the western sector (from Terento/Terenten to Chienes/Kiens municipalities) to a more diffuse pattern in the eastern sector (Falzes/Pfalzen municipality), where the KV is displaced by secondary orthogonal NNE-SSW trending faults and width of the fractured area between KV and PF increases. It is worth noting that the distance (≈ 2 km) among these secondary faults is consistent with the range of the experimental variogram of the radon data measured along the major axis of the anisotropy ellipse. This parameter represents the distance at which Rn migration along the fault system shows a continuous behaviour, and thus indicates the extension of the permeable sectors along the PF system that can be dissected by minor faults according to a series of relay ramps that may interrupt the continuity of this tectonic system. Accordingly, the length of the minimum anisotropy axis (≈ 1000 m) well fit with the N-S extension of the elongated radon anomaly occurring from Terento/Terenten to Chienes/Kiens municipalities. Furthermore, though CO_2 anomalies show a spotty distribution pattern, they are also consistent with the orientation of the PF and confirms the role of CO_2 as carrier gas for ^{222}Rn from deeper sources. A scatterplot between radon and CO_2 values (see Appendix 1, Fig. A3), occurring in correspondence of the anomalous area along the Pusteria Fault,

shows that there is a significant linear relationship between the two-gas species (p value < 0.0001) with coefficients R = 0.723 and R^2 = 0.523. This result confirms that CO_2 acts as a carrier gas for radon along the main fault. In the southern sector (Chienes/Kiens municipality and S. Sigismondo/ St. Sigmund village), low ^{222}Rn (below the background value of 50 kBq·m^{-3}) and high ^{220}Rn activities suggest the presence of high permeable soils in the shallow environment, considering the very short half-life of ^{220}Rn (55.6 s). According to this hypothesis, in this area CO_2 anomalies can be linked to shallower factors (e.g., soil humidity, organic matter) caused by the presence of the Rienza/Rienz river and farmed fields.

The eastern sector (Falzes/Pfalzen municipality) displays the highest ^{222}Rn activities (from 100 to 800 kBq·m^{-3}) measured in the area; these values are comparable with maximum ^{222}Rn activity (order of magnitude 102 kBq·m^{-3}) measured in different seismic intermontane basins in Italy (Ciotoli et al., 2016) and in China (Chen et al., 2018).

In this sector, ^{222}Rn anomalies show a more diffuse pattern though they are also characterised by local E-W anisotropy due to the presence of minor faults and according to the direction of the main fault system. In contrast, CO_2 spatial distribution does not show anomalous concentrations. This might be due to an increase in soil ventilation (i.e., CO_2 dilution) caused by the higher elevation of this zone (> 1800 m.a.s.l.), the reduced soil thickness and rock weathering (Cinelli et al., 2019) (i.e., the diffused presence of slope deposits consisting of large loose rock blocks). However, all these factors do not seem to affect ^{222}Rn emission in terms of TER.

In contrast, in the western sector (Terento/Terenten municipality) ^{222}Rn anomalies show a more defined anisotropic pattern extending towards the central sector (Chienes/Kiens municipality) where the ^{222}Rn anomalies are mainly restricted between the PF and the KV. However, this area is characterised by a less pervasive large-scale fracturing and thus radon measurements show lower values than those measured in the eastern sector (mean ^{222}Rn activities of 75 kBq·m^{-3} and 130 kBq·m^{-3}, respectively).

Despite the calculated mean value of ^{222}Rn activity at equilibrium with ^{226}Ra is slightly higher than that observed in the NPP, the contribution of the lithology is not high enough to justify the magnitude of the anomalies measured in the eastern sector (Falzes/Pfalzen area) and along the whole Pusteria fault. Therefore, we can conclude that all values above the anomaly threshold of 50 kBq·m^{-3} are reasonably supported by an upward migration along the fracture zone associated to the PF that promotes tectonically enhanced radon at the surface thus contributing to the increase of the GRP in terms of TER.

Based on the above considerations, we can confirm that the study area shows different pattern of ^{222}Rn, CO_2 and ^{220}Rn spatial distribution of the gas anomalies at the surface, primarily related to the

extension of the fracture zone and the length of the dislocation, and secondarily to local geological factors. These parameters mainly govern the pattern and the magnitude of the observed fault-linked Rn anomalies, thus suggesting a different geochemical activity (i.e., the gas-bearing property) of the fault segments that makes up the PF system (Seminsky and Demberel, 2013; Seminsky et al., 2014). In order to evaluate the correlation between TER and geometry of the PF system, we firstly investigated the relationship between radon anomalies and fault/fracture density map obtained by Kernel density algorithm in order to identify TER zones. Then we tried to quantify the TER zones in terms of radon activity index (RAI) (Seminsky et al., 2014).

Figure 5 shows a summary sketch map of the areas characterised by fault-linked Rn anomalies (e.g., TER). The map was obtained by reclassifying and overlaying radon anomalies (above 50 kBq·m^{-3}) and fault/fracture density map (> 1.5 fault·km^{-2}). The figure also highlights the distribution of the main and minor faults reported in the structural model.

In particular, the map shows 4 zones characterised by different radon sources and magnitude:

- the zone of lithological background (white area), statistically and geochemically defined by radon values below 50 kBq·m^{-3}; this zone (about 34 km^2) is characterised by Rn mean value of 20.5 kBq·m^{-3};
- the zone of high fault/fracture density (> 1.5 fault·km^{-2}) but with radon values below the background (pale grey area); this zone (about 14 km^2), where the presence of non-permeable fault segments is supposed, is characterised by Rn mean value of 22.3 kBq·m^{-3};
- the zone with radon activity higher than the background (silver grey area); this area, apparently not correlated to zones with high fault density, mostly occurs in the fractured area recognised within the fault system. This zone (about 8 km^2) is characterised by high Rn mean value of 111.5 kBq·m^{-3} that suggests the presence of radon advection processes which change toward the surface in a more diffusive (even laterally) character; this may explain the more pervasive distribution of radon anomalies;
- the TER zone (about 12 km^2) (dark grey area) is characterised by very high fault-linked radon anomalies with mean value of 154 kBq·m^{-3} mainly occurring in the area comprised between the KV and PF.

As TER represents the radon contribution from faulted areas, the quantitative evaluation of the contrast between the magnitude of the soil-radon anomalies (Rn_{Max}) near the fault and the lithological background (Rn_{BG}) was carried out by calculating the RAI for each fault-related radon concentration peak recognised along 21 N-S profiles (P4-P24) extrapolated from the estimated Rn grid map (Fig. 4a). The ratio between these two values can be considered as a function of the geochemical activity of the fault, as well as of the degree of fracturing in the damage zone. In general, high RAI values

correspond to high Rn absolute concentration values in the soil-gas. They are located above damage fault zones, and have great practical interest for the assessment of radon hazard in populated areas. The RAI values obtained in the study area provide a quantification of the geochemical activity of the PF system within the recognised TER zones. RAI values were grouped according to the classification procedure described in the RAI calculation section of the methods, and displayed as classed post map (Fig. 4).

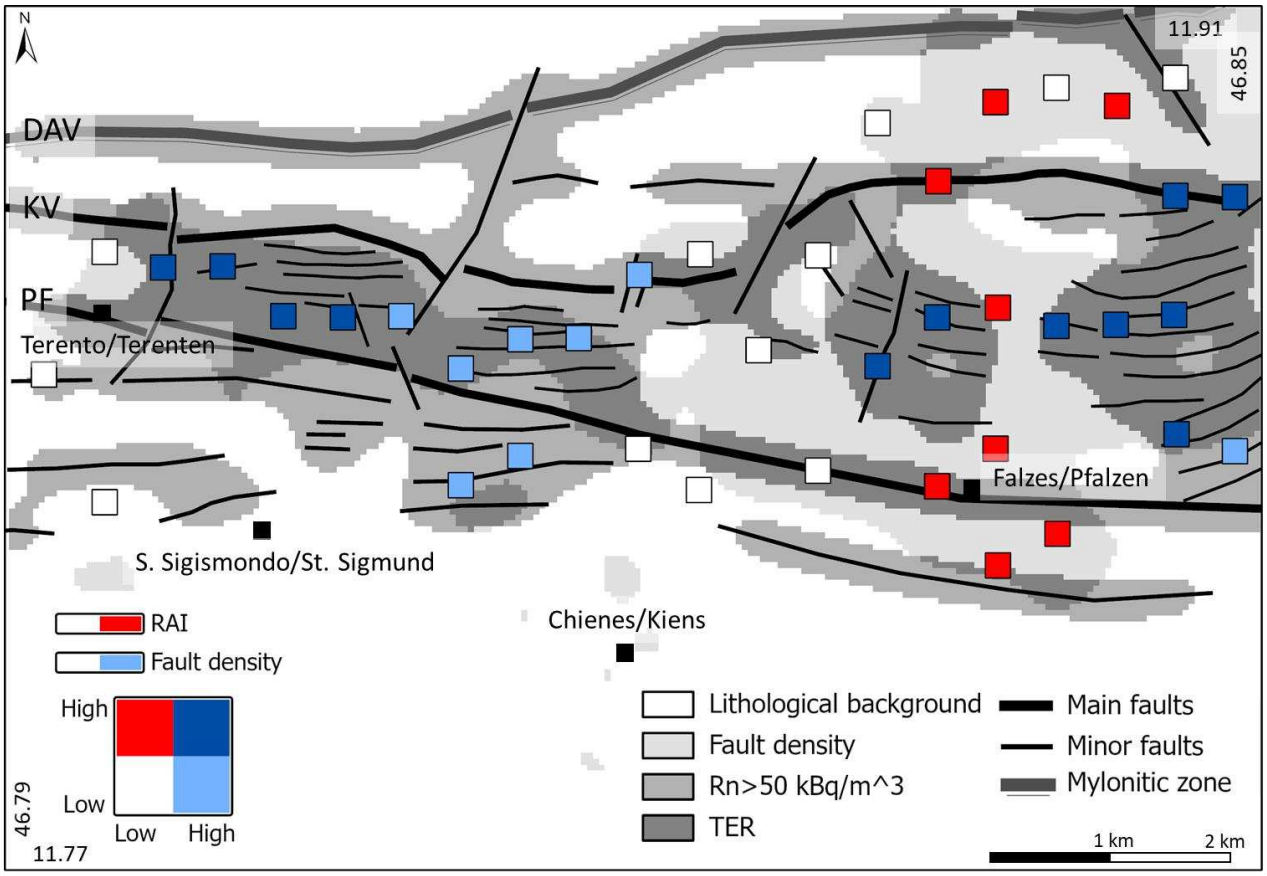

Figure 5. Summary sketch map of the areas characterised by radon fault-linked anomalies. The figure shows four different zones: (1) the lithological background (white area); (2) the fault density (pale grey area); (3) the area with radon activity higher than the background (> 50 kBq·m^{-3}) (silver grey area); (4) the zones with high fault-linked radon values (e.g., TER) (dark grey areas). The coloured square represents the location of RAI values related to the profile peaks and have been divided as follows: (i) white squares: low RAI value, low fault density; (ii) light-blue squares: low RAI value, high fault density; (iii) red squares: high RAI values, low fault density; (iv) blue squares: high RAI values, high fault density (strictly related to the TER zones). PF = Pusteria/Pustertal fault; KV = Kalkstein-Vallarga/Weintal fault; DAV = Defferegggen-Anterselva/Antholz-Valles/Vals mylonitic zone.

Calculated RAI values (see Appendix 1, Table A2) range from 1.08 to 13.86 and are grouped in four classes according to the following classification (Seminsky et al., 2014) scheme: low geochemical activity (RAI < 2), moderate geochemical activity (2 < RAI < 3), high geochemical activity (3 < RAI < 6) and very high geochemical activity (RAI > 6).

The classed post map of the RAI values highlights that 25 fault-related radon concentration peaks out of 40 (about 62%) are localized in the fracture zone between the two main faults (PF and KV), most of the values falling in the moderate (9), high (5) and very high (5) geochemical activity groups; values below 2 only occur in the area of Chienes/Kiens municipality and to the south of the PF. The distribution of the RAI values in Fig. 5 describes a specific pattern which follows the fault strike direction and extends over the fracture zone which is 5 km wide to the east and 2 km wide to the west, where the two main faults PF and KV tend to converge.

High to very high RAI values mainly occur in the eastern sector (Falzes/Pfalzen municipality). In this area, the highest RAI values (mean value = 4.8) correspond to high radon concentration peaks aligned along the direction of minor faults in the middle of the TER area (dark grey zones in Fig. 5) between the PF and the DAV fault.

The western sector (Terento/Terenten municipality) displays medium to high RAI values (mean value = 2.9) and the associated radon peaks are strictly located within the TER area occurring between the PF and KV. In this sector, RAI values of the Rn peaks show a good spatial continuity as suggested by the variogram model, and the radon anomaly in this case is controlled by increased gas permeability of the damage zone along this fault segment of the PF.

The central sector (Chienes/Kiens municipality) displays low RAI values (mean value = 1.6). Although located within the TER zone (dark grey TER area in Fig. 5), this area is characterised by a patchy pattern of the radon anomalies with fault segments along the main structure of the PF with radon activity slightly above the background values (< 100 $kBq \cdot m^{-3}$). These fault segments, bordered by secondary NNE-SSW tending transfer faults with sinistral relay ramp geometry, are characterised by relatively unfractured rocks covered by weathered soil that lowers the gas permeability thus having a high impact on the intensity of radon anomalies near the fault zone. These conditions determine the patchy character of soil gas anomalies (including radon) at the surface (Fig. 1D), and confirm that in this sector of the valley the PF system, despite of the high fracture density (pale grey area in Fig. 4), gas permeability is highly variable along its entire extension (Ciotoli et al., 2007, 2016).

DAV mylonitic zone does not show any specific Rn peak pattern because it is characterised by a very low gas permeability due to its massive mylonitic microstructure. Furthermore, since this fault is located along the northern sector of the study area, boundary effects due to the low sample density makes the estimate less robust due to the lack of neighbouring points (Ciotoli et al., 1999; Cressie 1993; Burt and Barber, 2009). According to the distribution of the TER zones and their RAI values, the Pusteria fault system displays different distribution patterns of the anomalies and variable geochemical activity. In particular, in the western sector, where the different fault lines of the PF system tend to converge the fault system behaves as a simple single fault (e.g., A and B in Fig. 1),

whereas in the eastern sector the PF system acts as a complex fault system (e.g., C and D in Fig. 1). The distribution of the TER zones, explained in terms of RAI, confirms that they are characterised by high to very high radon values when associated with high fault/fracture density.

The relative RAI values obtained along different N-S profiles reflect the contrast between the radon anomalies and the background. According to the described data, RAI values can vary along fault strike within an order of magnitude depending on the type and fracture density of the fault zone. The individuation of contrasting anomalies and the calculation of the Radon Activity Index (i.e. RAI) is crucial to quantify TER in a fault zone and interpret the data in terms of geochemical activity. The obtained results are in line with the RAI calculated for some seismically active faults reported in the literature confirming that also non-active faults may increase the GRP (Table 2).

We can establish that the collection of soil gas radon measurements for mapping the TER zones, as well as the calculation of RAI values in fault areas, are of practical interest for local authorities in the assessment of radon hazard, especially in urban areas.

Author	Area	Fault type	Maximum value	Background value	RAI
This study	Pusteria Valley – Periadriatic fault system	Transpressive fault	816 kBq m^{-3}	50 kBq m^{-3}	16
Ciotoli et al., 2007	Fucino Plain - SBGMF	Normal fault	119 kBq m^{-3}	25 kBq m^{-3}	5
Zhou et al., 2007b	Tibet - Lhasa	Normal fault	87.4 kBq m^{-3}	7.6 kBq m^{-3}	11
Li et al., 2009	Yanhuai basin, Hebei		57.8 kBq m^{-3}	8.1 kBq m^{-3}	7
Yao and Wang, 2009	Jixian Mountain, Tianjing		58.6 kBq m^{-3}	3.2 kBq m^{-3}	18
Zhou et al., 2011	Haiyuan, Ningxia		38.3 kBq m^{-3}	5.8 kBq m^{-3}	7
Seminsky et al., 2014	Baikal-Mongolian sesismic belt – Khustai fault	Normal fault	20.2 kBq m^{-3}	3.9 kBq m^{-3}	5
Wang et al., 2014	North China – Tangshan area	Normal fault	38.4 kBq m^{-3}	4.7 kBq m^{-3}	8
Chen et al., 2018	Capital of China - KQF fault		206.7 kBq m^{-3}	11.6 kBq m^{-3}	18
Xuan et al., 2020	Thua Thien Hue (Vietnam) - Dak Rong-Hue fault		144.5 kBq m^{-3}	24.8 kBq m^{-3}	6

Table 2. Values of RAI obtained by the ratio between the maximum value measured in case study the area and the background value over different areas in the world.

3.5. Conclusions

The main goal of this study was to evaluate the potential degassing processes along an aseismic fault system, the Pusteria fault system, in north-eastern Italy. To accomplish this objective, we have defined a further geogenic radon component (Tectonically Enhanced Radon, TER) that represents the contribution of tectonics to the Geogenic Radon Potential (GRP) of an area. Then, we have quantified the TER component by calculating the Radon Activity Index (RAI) that defines the geochemical activity of a fault in terms of Rn emission. The obtained results highlight the following conclusions:

- the fracture zone of the Pusteria fault system, including the main faults PF and KV, and other minor faults, plays a fundamental role for gas (^{222}Rn and CO_2) migration towards the surface thus providing TER as an additional contribution to the Rn diffusing from the source rocks (i.e., lithological background); both these components account for the GRP of an area;
- the summary map of the TER zones (Fig. 5) confirms that most of the areas characterised by high radon values are also associated with high fault/fracture density;
- radon activity index (RAI) calculated at Rn peak values along N-S profiles represents a good proxy to quantify the geochemical activity (e.g., gas-bearing properties) of a fault zone. We recognised that TER areas are characterised by medium to very high RAI values. However, although the central sector of the PF system shows high fault/fracture density, the low RAI values suggest the presence of less permeable segments along the fault system;
- the comparison of the calculated RAI with those calculated from seismic areas with active faults, reported in the literature, highlights that also aseismic faults can provide conduits for Rn migration towards the surface with the same order of magnitude of seismic faults;
- since the radon high activity generated from source rocks represents background areas of potential radon risk for inhabitants, the quantification and mapping of the TER areas are important to better evaluate the potential risk due to the increased radon availability to influx within buildings;
- the knowledge of these two components of the GRP is fundamental for the mapping of susceptibility of the territory at different spatial scales and in different geological scenarios, and can help policy makers to plan monitoring activities and take mitigation actions reducing the damage for the society. The future developments of TER concept will have important implications on the identification of radon priority areas (RPAs) as required by the European Directive 59/2013 (EURATOM/59/2013).

References

Akerblom, G. Ground radon: Monitoring procedure in Sweden, paper presented at the ‘‘JAG’’ Disc. Meeting on Radon Workshop, Geology, Environment, Technology, R. Astron. Soc., London, 12 Feb (1993).

Annunziatellis, A., Ciotoli, G., Lombardi, S., Nolasco, F. Short- and long-term gas hazard: The release of toxic gases in the Albani Hills volcanic area (central Italy). Journal of Geochemical Explorations. 77, 93-108 (2003). https://doi.org/10.1016/S0375-6742(02)00272-8.

Ascione, A., Ciotoli, G., Bigi, S., Buscher, J., Mazzoli, S., Ruggiero L., et al. Assessing mantle versus crustal sources for non-volcanic degassing along fault zones in the actively extending southern Apennines mountain belt (Italy). Geol. Soc. Am. Bull. 130, 1697-1722(2018). https://doi.org/10.1130/B31869.1.

Astorri, F., Beaubien, S. E., Ciotoli, G., Lombardi, S. An assessment of gas emanation hazard using geographic information system and geostatistics. Health Physics. 83(3), 358-366 (2002). DOI:10.1097/00004032-200203000-00008.

Baubron, J. C., Rigo, A., Toutain, J. P. Soil gas profiles as a tool to characterise active tectonic areas: the Jaut Pass example (Pyrenees, France). Earth and Planetary Science Letters. 196, 1-2, 28, Pages 69-81, (2002). https://doi.org/10.1016/S0012-821X(01)00596-9.

Beaubien, S. E., Ciotoli, G., Lombardi, S. Carbon dioxide and radon gas hazard in the Alban Hills area (central Italy). Journal of volcanology and geothermal research. 123, 63-80 (2002). https://doi.org/10.1016/S0377-0273(03)00028-3.

Bistacchi, A., Massironi, M., & Menegon, L. Three-dimensional characterization of a crustal-scale fault zone: The Pusteria and Sprechenstein fault system (Eastern Alps). Journal of Structural Geology. 32, 2022- 2041 (2010). https://doi.org/10.1016/j.jsg.2010.06.003.

Bistacchi, M. Massironi, L. Menegon, F. Bolognesi, V. Donghi. On The Nucleation of Non-Andersonian Faults Along PhyllosilicateRich Mylonite Belts. Geological Society Special Publication. 367, 1 (2012) https://doi. org/10.1144/SP367.13.

Bossew, P. et al. Development of a Geogenic Radon Hazard Index—Concept, History, Experiences. International Journal of Environmental Research and Public Health. 17, 4134 (2020). doi:10.3390/ijerph171141345.

Bossew, P. Mapping the Geogenic Radon Potential and estimation of Radon Prone Areas in Germany. Radiation Emergency Medicine. 4, 2, 13-20 (2015).

Burt, J. E.; Barber, G. M. (2009). Elementary statistics for geographers (3rd ed.). Guilford Press. ISBN 978-1572304840.

Capaccioni, B., Cinelli, G., Mostacci, D., Tositti, L. Long-term risk in a recently active volcanic system: evaluation of doses and indoor radiological risk in the quaternary Vulsini Volcanic District (Central Italy). Journal of Volcanololgy and Geothermics. 247 - 248, 26 - 36 (2012). https://doi.org/10.1016/j.jvolgeores.2012.07.01.

Chen, Z., Li, Y., Liu, Z., Wang, J., Zhou, X., & Du, J. Radon emission from soil gases in the active fault zones in the Capital of China and its environmental effects. Scientific Report. 8,16772 (2018). Doi: 10.1038/s41598-018-35262-1.

Cinelli, G., De Cort, M., Tollefsen, T. (Eds.). European Atlas of Natural Radiation. Publications Office of the European Union 190 pp, 2019. https://doi.org/10.1016/j.jenvrad.2018.02.008

Ciotoli, G. et al. Soil gas distribution in the main coseismic surface rupture zone of the 1980, M_S=6.9, Irpinia earthquake (southern Italy). Journal of Geophysical Research: Solid Earth. 119, 2440-2461 (2014). https://doi.org/10.1002/2013JB010508.

Ciotoli, G., Lombardi, S., Annunziatellis, A. Geostatistical analysis of soil gas data in a high seismic intermontane basin: Fucino Plain, central Italy. Journal of Geophysics. 112, B05407 (2007). http://dx.doi.org/10.1029/2005JB004044.

Ciotoli, G., Sciarra, A., Ruggiero, L., Annunziatellis, A., Bigi, S. Soil gas geochemical behaviour across buried and exposed faults during the 24 August 2016 central Italy earthquake. Annals of geophysics. 59, Fast Track 5 (2016). DOI: 10.4401/ag-7242.

Ciotoli, G; Etiope, G.; Guerra, M.; Lombardi, S. The detection of concealed faults in the Ofanto Basin using the correlation between soil-gas fracture surveys. Tectonophysics. 301, 321–332 (1999). https://doi.org/10.1016/S0040-1951(98)00220-0.

Coletti C., Brattich E. Cinelli G., Cultrone G., Maritan L., Mazzoli C., Mostacci D. Tositti L. Sassi R. Radionuclide concentration and radon exhalation in new mix design of bricks produced reusing NORM by-products: the influence of mineralogy and texture. Construction and Building Materials 260, 119820 (2020). doi: 10.1016/j.conbuildmat.2020.119820.

Coletti C., Ciotoli G, Benà E., Brattich E., Cinelli G., Galgaro A., Massironi M., Mazzoli M., Mostacci M., Mozzi P., Nava J., Ruggiero L., Sciarra A., Tositti L., Sassi R. The Geogenic Radon Potential by using the Empirical Bayesian Regression Kriging. The Euganean Hills district (Italy). Science of Total Environment 808, 152064, (2022). doi: 10.1016/j.scitotenv.2021.152064.

Cressie, Noel A. C. (1993). Statistics for Spatial Data. Wiley Series in Probability and Statistics. doi:10.1002/9781119115151. ISBN 9781119115151.

European Union, Council Directive 2013/59/Euratom of 5 December 2013 laying down basic safety standards for protection against the dangers arising from exposure to ionising radiation, and repealing Directives 89/618/Euratom, 90/641/Euratom, 96/29/Euratom, 97/43/ Euratom and 2003/122/Euratom. Official J. Eur. Union, OJ L13, 17.01.2014 (2013) 1–73. Official J. Eur. Union, OJ L13, 17.01.2014 (2013) 1–73.

Field, R.W. Radon: A Leading Environmental Cause of Lung Cancer. American Family Physician. 98, 280–282 (2018). www.aafp.org/afp.

Fossen, H. Structural Geology (2nd edition). Cambridge University Press, Cambridge (2016). Hardback, 524 pages, ISBN 9781107057647.

Fu, C.C., Yang, T.F., Du, J., Walia, V., Chen, Y.G. Variations of helium and radon concentrations in soil gases from an active fault zone in Southern Taiwan. Radiation Measurements. 43, S348-S352 (2009). https://doi.org/10.1016/j.radmeas.2008.03.035.

Ghosh, D., Deb, A., Sengupta, R. Anomalous radon emission as precursor of earthquake. Journal of Applied Geophysics. 69, 67-81 (2009). https://doi.org/10.1016/j.jappgeo.2009.06.001.

Gilmore, G.R. Practical Gamma-ray Spectrometry, second ed. John Wiley & Sons, New York (2008).

Giustini, F.; Ruggiero, L.; Sciarra, A.; Beaubien, S.E.; Graziani, S.; Galli, G.; et al. Radon Hazard in Central Italy: Comparison among Areas with Different Geogenic Radon Potential. Int. J. Environ. Res. Public Health. 19, 666 (2022). https://doi.org/10.3390/https://doi.org/10.3390/ ijerph19020666.

Hofmann, K.H., Kleinschrodt, R., Lippert, R., Mager, D. & Stoeckhert, B.: Geologische Karte des Altkristallins südlich des Tauernfensters zwischen Pfunderer Tal und Tauferer Tal (Südtirol). - Der Schlern, 57, 572-590, Bozen (1983).

Keim, L., Mair, V., Morelli, C. Inquadramento geologico regionale in: Guida ai percorsi geologici Foglio 026 Appiano. Ufficio Geologia e prove materiali, Provincia Autonoma di Bolzano, LAC Firenze. ISBN978-88-7914-678-4 (2013).

Koike, K., Yoshinaga, T.,Yoshinaga, T., Ueyama, T., & Asaue, H. Increase radon-222 in soil gas because of cumulative seismicity at active faults. Earth Planets and Space. 66(57),1-9 (2014). doi: 10.1186/1880-5981-66-5710.1186/1880-5981-66-57.

Li, Y., et al. Geochemical characteristics of soil gas in Yanhuai basin, North China. Earthquake Science. 22, 93-100 (2009). https://doi.org/10.1007/s11589-009-0093-3.

Massironi, M., Bistacchi, A., Menegon, L. Misoriented Faults in Exhumed Metamorphic Complexes: Rule or Exception? Earth and Planetary Science Letters. 307 (1-2). (2011). https://doi.org/10.1016/j.epsl.2011.04.041.

Müller, W., Mancktelow, N. S., Meier, M. Rb-Sr microchrons of synkinematic mica in mylonites: an example from the DAV fault of the Eastern Alps. Earth and Planetary Science Letters. 180, 385-397 (2000). https://doi.org/10.1016/S0012-821X(00)00167-9.

Nuccetelli, C. In situ gamma spectrometry in environmental research and monitoring. Applied Radiation and Isotopes (2008). https://doi.org/10.1016/j.apradiso.2007.10.019.

O'Sullivan, F. A Statistical Perspective on Ill-Posed Inverse Problems. Statistical Science. 1, 4, (1986). https://www.jstor.org/stable/2245801.

Oddone, G. Gli elementi fisici del grande terremoto marsicano fucense del 13 gennaio 1915, Bollettino Società Sismologica Italiana. 19, 71– 215 (1915).

Reiter, F., Freudenthaler, C., Hausmann, H., Ortner, H., Lenhardt, W., Brandner, R. Active Seismotectonic Deformation in Front of the Dolomites Indenter, Eastern Alps. Tectonics. 37 (12), 4625-4654 (2018). https://doi.org/10.1029/2017TC004867.

Sassi, F. P., Cesare, B., Mazzoli, C., Peruzzo, L., Sassi, R. & Spiess, R. The crystalline basement of the Italian eastern Alps: a review of the metamorphic features. Periodico di Mineralogia. Special issue 2: A showcase of the Italian research in metamorphic petrology. 73, 23-42 (2004).

Schmid, S. M. & Haas, R. Transition from near-surface thrusting to intra-basement decollement, Schlinig Thrust, Eastern Alps. Tectonics. 8, 4, 697-718 (1989). https://doi.org/10.1029/TC008i004p00697.

Schmid, S. M., Pfiffner A., Froitzheim, N., Schönborn, G., & Kissling, E..& Kissling, E.. Geophysical-geological transect and tectonic evolution of the Swiss-Italian Alps. Tectonics. Vol. 15, Issue 5, 1036-1064 (1996). https://doi.org/10.1029/96TC00433.

Seminsky, K. Zh, & Demberel, S. The first estimation of soil-radon activity near faults in Central Mongolia. Radiation Measurements. 49,19-34(2013). https://doi.org/10.1016/j.radmeas.2012.12.013.

Seminsky, K. Zh., Bobrov, A. A., Demberel, S. Variations in Radon Activity in the Crustal Fault Zones: Spatial Characteristics. Physics of the Solid Earth. 50, 6, 795–81 (2014). https://doi.org/10.1134/S1069351314060081.

Sinclair, A. J. A fundamental approach to threshold estimation in exploratory geochemistry: probability plot revisited. Journal of Geochemical Exploration. 41, 1-22 (1991). https://doi.org/10.1016/0375-6742(91)90071-2.

Stromswold, D.C. Calibration facilities for borehole and surface environmental radiation measurements. Journal of Radioanalytical Nuclear Chemistry. 194 (2), 393 - 401 (1995). Doi: https://doi.org/10.1007/bf02038439

Walia, V., et al. Continuous temporal soil-gas composition variations for earthquake precursory studies along Hsincheng and Hsinhua faults in Taiwan. Radiation Measurements. 44, 934–939. (2009). https://doi.org/10.1016/j.radmeas.2009.10.010

Wang, X., Li, Y., Du, J., & Zhou, X. Correlations between radon in soil gas and the activity of seismogenic faults in the Tangshan area, North China. Radiation Measurements. 60, 8-14 (2014). https://doi.org/10.1016/j.radmeas.2013.11.001.

Xuan, P. T., et al. Soil gas radon measurement for identify active faults in Thua Thien Hue (Vietnam), Journal of Geoscience and Environment Protection. 8, 44-64 (2020). Doi:10.4236/gep.2020.87003.

Yanga T. F. et al. Variations of soil radon and thoron concentrations in a fault zone and prospective earthquakes in SW Taiwan. Radiation Measurements. 40, 496-502 (2005). https://doi.org/10.1016/j.radmeas.2005.05.017.

Yao, H.M., & Wang, Z.G. Research on the relationship between the soil radon density and fault and geotherm at the foreland of Jixian mountain, Tianjing. Geological Survey Research. 33 (3), 221-227 (2009) (in Chinese with English abstract). https://doi.org/10.1016/j.radmeas.2013.11.001.

Zeeb, H. & Shannoun, F. (eds.). WHO handbook on indoor radon - a public health perspective (2009). ISBNS 978 92 4 154767. https://www.who.int/publications/i/item/9789241547673

Zhou, X.C., et al. Geochemical characteristics of radon and mercury in soil gas in Lhasa, Tibet, China. Environmental Science. 28 (3), 659-676 (2007b) (in Chinese with English abstract).

Zhou, X.C., Wang, C.Y., Chai, C.Z., Si, X.Y., Lei, Q.Y., Li, Y., Xie, C., Liu, S.C., 2011. The geochemical characteristics of soil gas in the southeastern part of Haiyuan fault. Seismol. Geol. 33 (1), 123 - 132 (in Chinese with English abstract). doi: 10.11939/jass.2017.01.008.

4. Chapter 2:

A new perspective in radon risk assessment: Mapping the geological hazard as a first step to define the collective radon risk exposure

Abstract

Radon is a radioactive gas and a major source of ionising radiation exposure for humans. Consequently, it can pose serious health threats when it accumulates in confined environments. In Europe, recent legislation has been adopted to address radon exposure in dwellings; this law established national reference levels and guidelines for defining Radon Priority Areas (RPAs). This study focuses on mapping the Geogenic Radon Potential (GRP) as a foundation for identifying RPAs and, consequently, assessing radon risk in indoor environments. Here, GRP is proposed as a hazard indicator, indicating the potential for radon to enter buildings from geological sources. Various approaches, including multivariate geospatial analysis and the application of artificial intelligence algorithms, have been utilised to generate continuous spatial maps of GRP based on point measurements. In this study, we employed a robust multivariate machine learning algorithm (Random Forest) to create the GRP map of the central sector of the Pusteria Valley, incorporating other variables from census tracts such as land use as a vulnerability factor, and population as an exposure factor to create the risk map. The Pusteria Valley in northern Italy was chosen as the pilot site due to its well-known geological, structural, and geochemical features. The results indicate that high Rn risk areas are associated with high GRP values, as well as residential areas and high population density. Starting with the GRP map (e.g., Rn hazard), a new geological-based definition of the RPAs is proposed as fundamental tool for mapping Collective Radon Risk Areas in line with the main objective of European regulations, which is to differentiate them from Individual Risk Areas.

Benà, E.[1], Ciotoli, G.[2,3], Petermann, E.[4], Bossew, B.[4*], Ruggiero, L.[5], Verdi, L.[6], Huber, P.[7], Mori, F.[2], Mazzoli, C.[1] and Sassi, R.[1]

[1]Dipartimento di Geoscienze, Università di Padova, Padova, Italy
[2]Istituto di Geologia Ambientale e Geoingegneria (IGAG), Consiglio Nazionale delle Ricerche (CNR), Rome, Italy
[3]Istituto Nazionale di Geofisica e Vulcanologia (INGV), Rome, Italy
[5]Federal Office for Radiation Protection (BfS), Section Radon and NORM, Berlin, Germany (*retired)
[4]Istituto Nazionale per la Ricerca e la Protezione Ambientale (ISPRA), Roma
[6]Provincia Autonoma di Bolzano, Laboratorio analisi aria e radioprotezione, Bolzano, Italy
[7]Azienda Sanitaria dell'Alto Adige, Bressanone, Italy

A slightly different version of this chapter is published in *Science of the Total Environment* (Benà et al., 2024).

Authorship contribution statement:

E.B. Conceptualisation, *in-situ* analyses, data curation, methodology, writing - original draft preparation, reviewing and editing. **G.C.** conceptualisation, *in-situ* analyses, methodology, writing - reviewing and editing. **E.P.** methodology, software, reviewing and editing. **P.B.** conceptualisation, reviewing and editing. **L.R.** *in-situ* analyses, reviewing and editing. **L.V.** reviewing and editing. **P.H.** water springs sampling. **F.M.** software, Python code. **C.M.** conceptualisation, reviewing and editing. **R.S.** conceptualisation, *in-situ* analyses, project administration, supervision, funding acquisition, reviewing and editing.

Graphical abstract

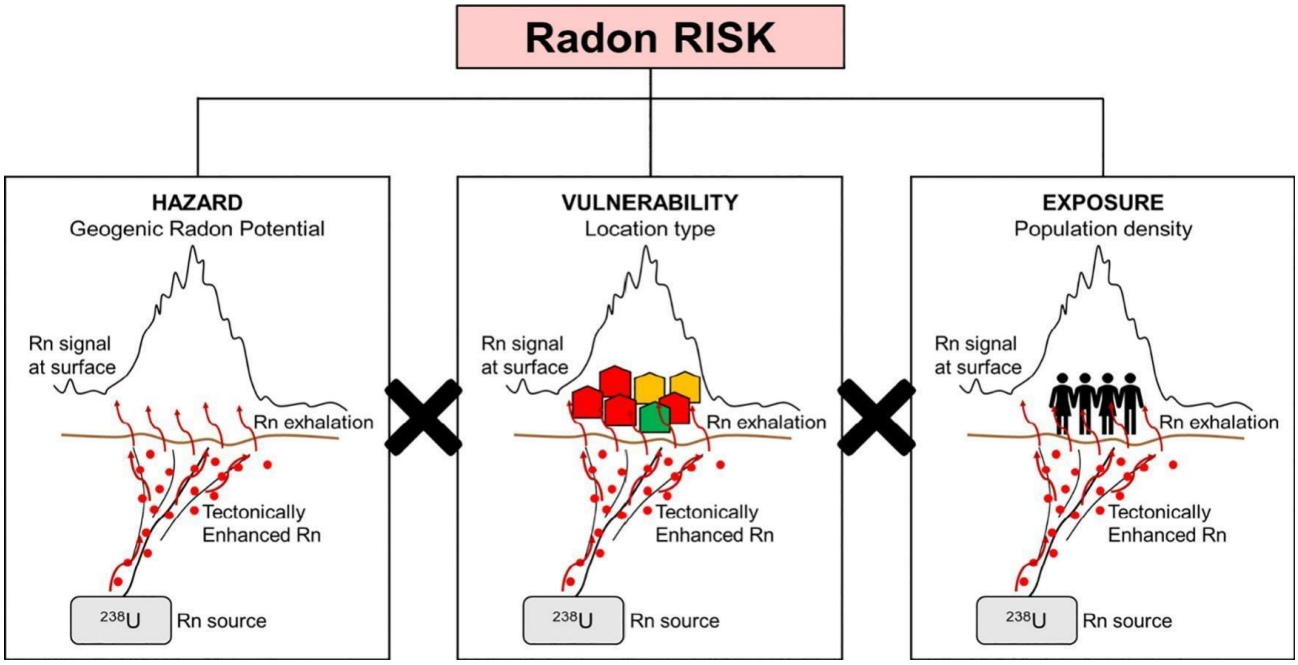

Highlights

- Mapping the Geogenic Radon Potential using a robust machine learning technique.
- Apply the risk definition to define the Collective Radon Risk Areas.
- Construction of the geological-based Collective Radon Risk Areas map.
- Mapping the Collective Risk to define areas subject of territorial planning.

Abbreviations: GRP = Geogenic Radon Potential; RPAs = Radon Priority Areas; IRC = Indoor Radon Concentration; BRS = Background Radon Source; TER = Tectonically Enhanced Radon; SRE = Surface Radon Exhalation; CRAs = Collective Risk Areas; IRAs = Individual Risk Areas; SGRC = Soil Gas Radon Concentration; TGDR = Terrestrial Gamma Dose Rate; ML = Machine Learning; FD = Fault density

4.1. Introduction

Radon (^{222}Rn, hereafter referred to as Rn) is a radioactive gas considered the primary source of ionizing radiation exposure for the population. Its potentially harmful effects on human health have been extensively documented (WHO, 2009). Rn gas represents a significant hazard when it accumulates in indoor environments, such as residential houses and workplaces (Indoor Radon).

Exposure to indoor radon is a serious issue that has prompted Europe to introduce legislation (Basic Safety Standards Directive 2013/59/EURATOM). This legislation, on one hand, establishes maximal national reference levels aimed at reducing Indoor Radon Concentration (IRC) exposure. On the other hand, it encourages public administrations to define Radon Priority Areas (RPAs). Therefore, it is essential to identify areas characterised by the highest Rn hazard for the population.

Rn gas has a natural origin and its concentration in the environment can vary depending on the geological characteristics of an area. In particular, the Geogenic Radon Potential (GRP) can be considered an optimal Rn hazard indicator as it conceptualises "*what Earth delivers in terms of radon*" from geogenic sources (e.g., radionuclides content in rocks and soils, faults and fractures) to the atmosphere (Bossew, 2015; Bossew et al., 2020).

The GRP is characterised by the interaction of three natural processes:

• Background Radon Source (BRS) represents the process that produces Rn through the natural decay of uranium (U) and thorium (Th) (^{220}Rn), which are present in rocks and soils.

• Tectonically Enhanced Radon (TER, Benà et al., 2022) accounts for processes that allow radon to migrate more easily towards the surface through permeable pathways (e.g., faults and fractures in the crust) from deeper sources, caused by increased stress and pressure conditions associated with tectonic activity.

• Surface Radon Exhalation (SRE) is the process by which radon gas is released from the ground into the atmosphere. SRE considers variables affecting radon movement in the shallow soil up to the soil/atmosphere interface (e.g., land morphology, soil permeability, atmospheric pressure, humidity, and temperature). This quantity of radon represents the amount that could potentially enter buildings, although BRS and TER are the dominant geological radon sources.

Over the years, several approaches have been applied to estimate the GRP over an area (e.g., Neznal et al., 2004; Bossew et al., 2015; Pasztor et al., 2016; Ciotoli et al., 2017; Giustini et al., 2019; Petermann et al., 2021; Coletti et al., 2021).

A widely used method to define the GRP, due to its simplicity, was proposed by Neznal et al. (2004). Neznal's approach is based on the measurement of two quantities: Rn concentration in the soil and soil permeability.

More recently, Pasztor et al. (2016) and Ciotoli et al. (2017) applied multivariate geospatial analysis (regression kriging and geographical weighted regression, respectively) to model GRP, using Soil Gas Radon Concentration (SGRC) and selected environmental proxies for the first time.

In the past three years, researchers have developed more advanced multivariate techniques, such as regression kriging (Coletti et al., 2021) and Machine Learning (ML, Petermann et al., 2021) algorithms which include several predictor variables associated with the geogenic Rn component.

However, it is important to emphasise that all these techniques require the measurement of SGRC or IRC as a response variable.

An issue faced by many European nations is the lack of sufficient SGRC measurements to support GRP mapping. As a consequence, the Geogenic Radon Hazard Index was proposed (Bossew et al., 2020). The Geogenic Radon Hazard Index concept arose from the need to determine a particular indicator using regionally accessible geological variables. The Geogenic Radon Hazard Index values for regions with consistent geogenic factors but different data sources should be comparable.

Cinelli et al. (2015) proposed a method for achieving consistency. It involved assigning weights to continuous or categorical input variables (covariates) based on their contribution to the index. Another way to enhance data consistency is the application of techniques that do not require a response variable (i.e., Spatial Multi Criteria Decision Analysis, Ciotoli et al., 2020).

It is crucial to map GRP as accurately as possible using a robust methodology, as GRP represents the amount of radon that could potentially enter buildings and is considered the most significant spatial predictor of IRC. In this context, the Basic Safety Standards European Directive 59/2013, transposed into Italian law by Legislative Decree n.101/2020, further emphasises the importance of identifying RPAs. Originally, RPAs were defined as areas where the annual average IRC in a significant number of dwellings is expected to exceed the reference level of 300 $Bq \cdot m^{-3}$. However, the concept and interpretation of "significant number of buildings" in the European Directive remained unclear.

Recently, Petermann et al. (2022) highlighted that the interpretation of "significant number" of buildings is factually based on the concept of geogenic hazard, and it relates to a relevant percentage of buildings within an area, regardless the number of houses or people affected. This concept does not encompass the collective concept of geogenic risk.

On the other hand, there is no uniform decision at the regional scale regarding the selection of the reference level and the threshold of probability percentage (p_0) of buildings exceeding the reference level. In general, the majority of European nations (including Finland, Germany, Greece, Montenegro, and Spain) adhere to the European Directive, adopting the recommended reference level of 300 $Bq \cdot m^{-3}$and a probability threshold of 10% (Bossew, 2018). For instance, Italy has a reference level of 300 $Bq \cdot m^{-3}$ and a p_0 of 15% (D. Lgs. n. 101/2020). A map illustrating the confusing diversity of RPA definitions across Europe has been compiled in Bossew and Suhr (2023, see Fig. 2 in the cited paper).

As reported in Bossew et al. (2021), the goals of the legislation in term of radiation protection from Rn indoor are twofold: (*i*) protect people from high Rn exposure to reduce individual risk (even if few people are involved); (*ii*) avoid high exposure to the community: the harm to society is proportional to the collective risk.

European legislation aims to reduce the detriment from Rn exposure (i.e., the number of lung cancer deaths) and, as a consequence, reduce collective exposure. Collective exposure can be assessed by introducing the concept of collective risk, which complements the individual risk concept (the "classical" RPA). Collective risk can be understood as consisting of many small individual risk zones. Based on these considerations, we propose mapping Collective Radon Risk Areas (CRAs) by applying the definition of risk, which combines hazard, vulnerability and exposure factors. We use this concept as complementary to mapping Individual Risk Areas (IRAs) associated with IRC (i.e., "classical" RPAs).

The main goal of this research is to demonstrate in a test area the efficacy of CRAs maps in defining Rn risk areas. We base this on the GRP map (the hazard factor) elaborated using a ML technique (i.e., Random Forest, RF). The test area chosen is the Pusteria Valley, which has been selected because of its well-known geological, structural, and geochemical characteristics, and the availability of numerous additional data (Benà et al., 2022). The obtained GRP map (hazard) was merged with the land use type (vulnerability) and population (exposure) data from census tracts available from the ISTAT (*Istituto Nazionale di Statistica*) website to identify CRAs.

4.2. Methods

4.2.1. Test area

The test area is located in the Pustertal/Pusteria Valley in the Italian Eastern Alps (Bolzano province, see Fig.1 in Benà et al., 2022) and it has been selected because of its well-known geological and structural characteristics. Into details, the study area is located across the complex Pusteria Fault System which comprises three main faults: the Deffereggen-Anterselva-Valles (DAV) mylonitic zone (Muller et al., 2000); the Kalkstein-Vallarga (KV) fault (Borsi et al., 1978) and the Pusteria fault (Schmidt et al., 1989). The Pusteria fault separates two different domains in the study area: (*i*) the Austroalpine crystalline basement (to the north) that is mainly composed by micashists and paragneiss (locally grading to migmatites) (Sassi et al., 2004); (*ii*) the Southalpine crystalline basement (to the south) which consists of a thick phyllitic sequence (Spiess et al., 2010) with Permian granite intrusions. The test area and the fault system are also well known from a geochemical point of view since its high degassing has been previously documented in Benà et al., (2022).

Geographically, the study area includes a part of three main municipalities: Terenten/Terento (~1800 inhabitants) to the western part, Kiens/Chienes (~3000 inhabitants) to the central part and Pfalzen/Falzes (~2900 inhabitants) to the eastern part. In the mentioned municipalities, the population is mainly grouped in residential areas and housing units; however, most of the study area is

mountainous and sparsely populated. In general, the residential houses have 3 to 4 floors spanning from the basement (-1) and the second floor (2) where present; the building materials are mainly brick and concrete, occasionally local rocks and wood (Verdi et al., 2004).

The test zone has been also chosen due to the availability of numerous additional data (see for example the *in-situ* measurements from Benà et al., 2022; the primary base maps available online in the Bolzano Province Geo-catalogue; the census variables and the demographic data available on the online ISTAT – *Istituto Nazionale di Statistica* website; indoor radon surveys reported in Minach et al., 1999 and Verdi et al., 2004, but not utilised in the current work to define the CRAs).

4.2.2. Experimental strategy

A dataset including different variables (e.g., response and predictors) was used to elaborate the GRP map for the study area. This was achieved by employing a ML technique, specifically the Random Forest (Breiman, 2001), to predict radon values at grid points. The resulting GRP map served as the hazard factor in the risk equation (Eq. 2, as detailed in section 2.4) and was multiplied by census tract data for land use and population density, representing the vulnerability and the exposure factors, respectively.

Figure 1 shows the flowchart of the applied procedures. Data processing was carried out using ArcGIS Pro 3.1.2 (copyright 2023@ESRI Inc.) and Scikit-learn library in Python PyCharm 2023.1.2 (Copyright © 2010–2023 JetBrains s.r.o.).

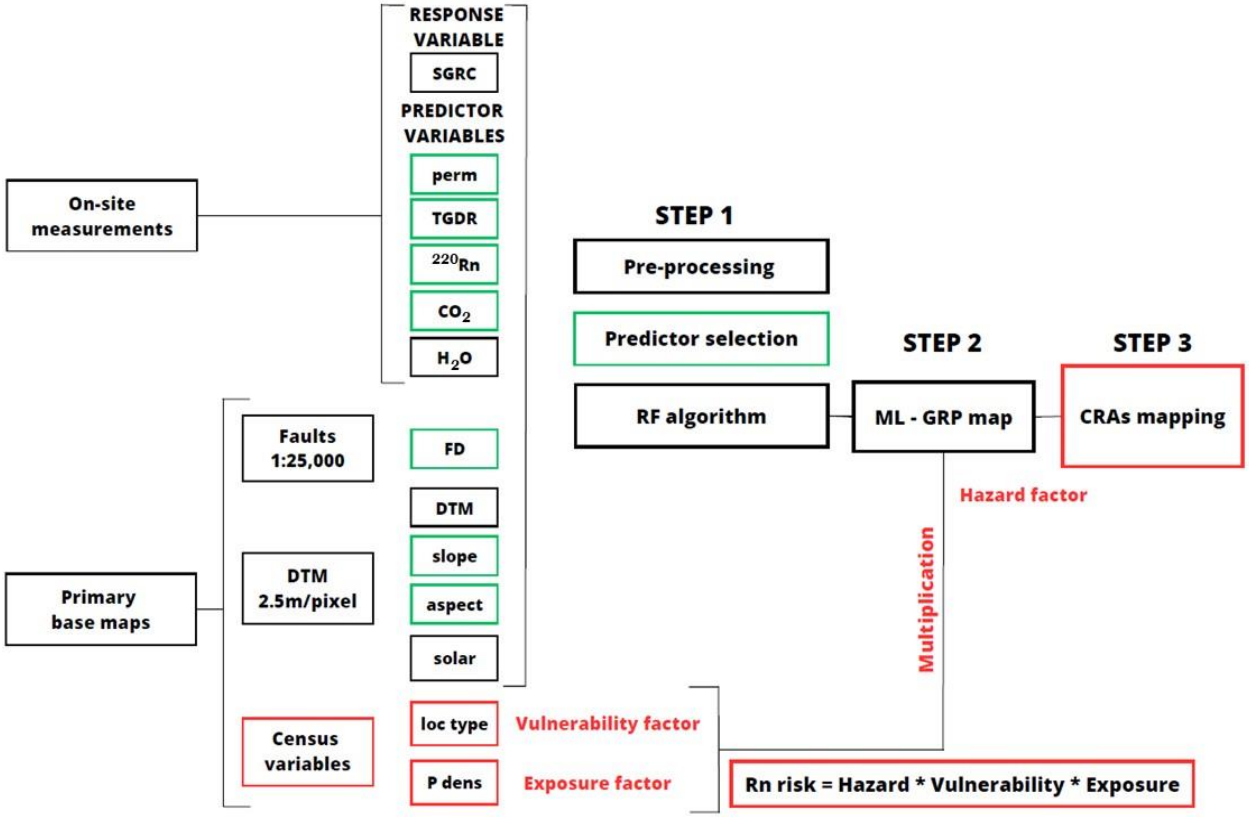

Figure 1. Flowchart of the mapping process and procedures. SGRC = Soil Gas Radon Concentration; perm = soil permeability; TGDR = Terrestrial Gamma Dose Rate; ^{220}Rn = thoron; CO_2 = carbon dioxide concentration in soil gas; H_2O = concentration of radon dissolved in water; FD = fault density; DTM = digital terrain model; slope = slope; solar = solar radiation; loc type = location type: P dens = population density; GRP map = Geogenic Radon Potential map; RPAs = Radon Priority Areas. SGRC, permeability, TGDR, thoron, carbon dioxide, radon dissolved in water, faults, DTM were pre-processed in order to apply the RF (Random Forest) algorithm (first step) to construct the GRP map (hazard factor). The GRP map was then multiplied by the location type (vulnerability factor) and population density (exposure factor) to construct the CRAs map.

4.2.3. Dataset

The dataset comprises one response variable (SGRC) and ten independent variables, which were either measured on-site or derived from primary base maps available online through the Bolzano Province Geo-catalogue (http://geokatalog.buergernetz.bz.it/geokatalog/#!). These ten variables were selected as potential predictors for ML regression models.

Soil gas surveys (^{222}Rn, ^{220}Rn, CO_2) (Benà et al., 2022), Terrestrial Gamma Dose Rate (TGDR), and permeability measurements were collected on-site during two separate field campaigns in the summers 2021 and 2022, conducted under similar and stable climatic conditions. The Digital Terrain Model (DTM) at a 2.5 m resolution and fault density data were obtained from the base maps available in the Bolzano Province Geo-catalogue.

The potential predictors underwent pre-processing using geospatial analysis to generate 50x50 m raster maps (refer to Fig. A1 in Appendix 2). We used the "Extract multi-value to point" tool in ArcGIS Pro to assign values of the predictors to each node of the raster maps, ensuring that we had a

value for each predictor variable for each Rn observation. The resulting dataset, containing the predictors and the response variable (SGRC), was used to train the Random Forest (RF) model. Once the best model was identified, it was applied to a regular 50x50m point fishnet, corresponding to the centroids of the predictor raster grid. The final dataset consists of 27,758 points, encompassing complete information for all predictors. The following sections provide a detailed description of the response variable and the predictors.

4.2.3.1. Response variable

SGRC ($kBqm^{-3}$) was used as the response (dependent) variable in the Random Forest Regression algorithm to create the GRP map. The original Rn dataset is composed by soil gas radon surveys obtained in the field according to the methodology and sample pattern described in detail by Benà et al. (2022). In particular, 278 SGRC values have been collected in the study area (~60 km^2) and correspond to a sampling density of 4-5 points of measurements per km^2. This sampling density, in case of SGRC measurements, is perfectly in line with other known studies in the literature carrying out a similar methodological approach (see for example: Ciotoli et al., 2007, 2017; Pasztor et al., 2016; Iovine et al., 2018; Coletti et al., 2021; Petermann et al., 2021).

4.2.3.2. On-site predictor variables

Five predictors were measured in the field: thoron (^{220}Rn) and carbon dioxide (CO_2) concentration in soil gas, TGDR, permeability, and ^{222}Rn dissolved in groundwater. Thoron and carbon dioxide (CO_2) were measured using the same method and at the same sampling locations as described in Benà et al. (2022).

TGDR measurements

The TGDR has been utilised as a proxy for the BRS contribution in the geogenic radon component. In particular, this variable is referred to the Rn produce by the decay of the principal radionuclides content in rocks (^{238}U, ^{232}Th) and it simulates the lithological background; in fact, terrestrial radiation also varies according to the lithology, genesis and age of rocks and by adsorption at the Earth's surface (Cinelli et al., 2019).

TGDR measurement were performed *in-situ* at 76 sampling points using a NaI γ-ray portable scintillometer (Scintrex GRS-500) pre-set to a total count rate window corresponding to the energy interval range between 80-3000 keV. The device was held 1 m above the ground for a measuring time required to achieve a 3% accuracy. The sensitivity factor of the Scintrex GRS-500 is 3.40 cps/nGyh,

allowing the counting rates to be converted into the International System unit of gamma dose rate (μSv/h, Giustini et al., 2019, 2022). Geostatistical analysis, including experimental variogram calculation, modelling, and kriging, was employed to generate a prediction map of the TGDR (see Fig. A2a and A2b in the Appendix 2).

Permeability

Soil gas permeability directly affects the migration of radon gas from the ground, primarily through advection along fractures and faults, as well as in the shallow soil primarily through diffusion mechanisms (Nuhu et al., 2021; Neznal et al., 2005). The radon concentration in soil gas is directly dependent on the geological characteristics of the area, such as the radionuclides concentration in rocks and soils, and the presence of fractures and faults. It can also be strongly influenced by soil permeability, which relates to soil pore dimensions and soil moisture content (Benavente et al., 2019; Lara et al., 2015). Additionally, other physical characteristics of soils, including soil texture and grain size, significantly impact the mechanisms of radon emanation and exhalation in the soil environment (Huynh Nguyen et al., 2018; Yang et al., 2019).

In the study area, soil permeability was measured at 76 sampling points using a custom permeameter developed by the University of Roma Tre, designed to connect directly to the same probe used for soil gas sampling (Castelluccio et al., 2015). The soil is assumed to be homogeneous and isotropic, and standard state conditions are considered. Air is assumed to be incompressible. The calculation of the soil permeability (k) is based on Darcy's equation and expressed in square meters (m^2). Geostatistical analysis, including experimental variogram calculation, modelling and kriging, was applied to obtain the prediction map of soil permeability (see Fig. A3a and A3b in the Appendix 2).

Radon dissolved in groundwater

Dissolved ^{222}Rn was measured at 22 water springs in the study area. Water samples from the selected springs had already undergone chemical-physical analysis by the *Agenzia provinciale per l'ambiente e la tutela del clima – Laboratorio analisi acque e cromatografia* (Bolzano Province) in 2022.

Rn in groundwater is significant since an amount of the indoor radon concentrations derive from the groundwater through the drinking water supply systems. This variable has the potential to affect the IRC, especially in cases where groundwater levels are close to the surface. In Italy, the reference level regarding the radon dissolved in groundwater intended to serve as drinking water is 100 $Bq \cdot L^{-1}$ (see 59/2013/EURATOM and the transposed D. Lgs. n. 101/2020 in the Italian regulations). In the study area, all the municipalities use drinking water from captured springs located at high altitude (>1600 m.a.s.l.) and these are therefore analysed for the study. Water was directly sampled from the springs

using glass bottles. Rn concentrations were measured using the RAD7 system (Durridge Company Inc.) in sniff mode, connected to the Big Bottle RAD H_2O and drystick (drierite desiccant) accessories. Before measurements, the system was purged to ensure that the moisture content inside the system was reduced to less than 10% humidity. The sampled bottle was then connected in a closed air-loop mode to the RAD7 system. During system operation, continuous circulation gradually enriched the air within the closed loop with the dissolved Rn from the water sample. Each measurement was conducted with a 5-minute integration period and repeated until the difference between the last two readings was less than 5-10%. The final result was calculated by averaging the previous two integrations. Thiessen polygons were constructed to create a map of areas of influence around the water springs. The water springs represented the centroid of the Thiessen polygons, where the measured dissolved radon value (i.e., the centroid) was assumed to be representative of the entire area underlying the polygon.

4.2.3.3. Derived predictor variables

Fault density

Faults and fractures serve as the primary pathways for the migration of radon and other gases, such as CO_2 and methane (CH_4), in the subsoil from deep sources (Ciotoli et al., 2007, 2014, 2017, 2020; Giustini et al., 2019). Therefore, the network of the fractured zones characterising the study area has been used as a proxy for secondary permeability. The distribution of the main faults in the study area (Keim et al., 2013) was converted into a fault density (FD) map using the quadratic kernel density function (Silverman, 1986), as described in Benà et al. (2022).

Digital terrain model (DTM)

DTM of the study area, representing elevation, was used as a proxy for meteorological conditions that can strongly affect radon migration and exhalation mechanisms. The Radon mobility can be impacted by the presence of slopes, hills, and depressions, which can alter air flow and soil pressure (Gundersen et al., 1992). Radon may not accumulate as much in areas with rough terrain because air circulation and groundwater drainage may be higher in such terrains. Conversely, low-lying areas and depressions may act as radon traps, resulting in higher concentrations in soil gas (Sukanya et al., 2021). Furthermore, Griffiths et al. (2014) emphasised the importance of considering topographic interactions when estimating radon concentrations across different geographical areas. The DTM (2.5 m/pixel) of the Bolzano Province is available from the Geo-catalogue of the Bolzano Province (http://geokatalog.buergernetz.bz.it/geokatalog/#!). The "Surface Parameters tool of Spatial Analyst" in ArcGIS Pro was applied to the DTM to create maps of additional potential proxies: slope, solar

radiation (e.g., Areal Solar Radiation) and aspect. Slope can be used as a proxy for soil moisture and shallow soil meteorological conditions, while solar radiation serves as a proxy for microclimate and temperature. Aspect (i.e., slope exposure) refers to the compass direction of the downhill slope faces in relation to the sun. In detail, slope conditions, such as the angle, aspect, and elevation of a land surface, can strongly influence local weather patterns and microclimates, acting as proxies for various meteorological conditions (e.g., sun exposure, rainfall distribution, wind patterns, temperature gradients), all of which may impact radon generation and movement (Zalloni et al., 2018).

4.2.4. Predictor selection

Predictor selection was carried out using Least Absolute Shrinkage and Selection Operator (LASSO) regression. LASSO regression is an extension of ordinary least squares (OLS) regression used in statistical modelling and ML to estimate the relationships between variables and make predictions (Tibshirani, 1996, 2011; Durrant et al., 2021). This technique aims to strike a balance between model simplicity and accuracy by introducing a penalty term into the traditional linear regression model, which enables sparse solutions in which some coefficients are forced to be exactly zero. LASSO is especially useful for variable selection because it can automatically identify only the most relevant variables while discarding irrelevant or redundant ones, particularly when we assume that many of the features do not significantly contribute to the target variable (Durrant et al., 2021; Handorf et al., 2020). It also helps prevent overfitting by removing variables with low predictive value, potentially making the model more robust across datasets. Furthermore, because it can choose between correlated explanatory variables, it can aid in optimising models with high multicollinearity. In simple terms, LASSO regression adds a penalty term to the Mean Squared Error (MSE) used in linear regressions. This penalty term is proportional to the sum of the absolute values of the variable coefficients. LASSO regression seeks coefficient values that minimize the sum of the MSE and the penalty.
The LASSO regression cost function is defined as follows (Eq. 1):

$$J(\beta) = \left(\frac{1}{n}\right) * \sum(y_i - \hat{y}_i)^2 + l * \sum|\beta_j| \quad (1)$$

where

- J(β) is the cost function
- n is the number of data or physical samples (statistically, the sample size)
- y_i is the actual output for the i-th sample
- $\hat{y}_i$ is the predicted output for the i-th sample

- βj represents the coefficients (weights) associated with each feature
- l is the regularization parameter that controls the amount of regularization applied to the model. Higher values of l lead to more regularization, resulting in a more pronounced feature shrinkage and potentially some coefficients becoming exactly zero.

In this work, LASSO regression was implemented in Python code using the Scikit-learn module (sklearn.linear_model.Lasso).

4.2.5. Machine learning and Geogenic Radon Potential mapping

ML algorithms enable the solution of highly complex problems. They involve the creation of a model by processing a dataset and subsequently predicting the values of new input data points by executing the established model, typically referred as supervised ML (Rebala et al., 2019). In recent literature within the field of environmental science, ML techniques have gained prominence for spatial prediction tasks. These applications include landslide prediction (Micheletti et al., 2014; Tehrani et al., 2022), soil mapping (Hengl et al., 2017), GRP mapping (Petermann et al., 2021) and time series analysis (Janik et al., 2018). ML can effectively handle complex, multi-dimensional, non-linear relationships and often does not make strong assumptions about the underlying data distribution (Fouedijo and Klump, 2019). Moreover, ML-based approaches have demonstrated superior performance compared to classical geostatistical models in various prediction tasks involving highly complex systems (e.g. Nussbaum et al., 2018; Hengl and MacMillan., 2019; Li et al., 2019).

ML models excel in capturing the influence and interplay of numerous factors. In this specific study, we applied a supervised ML method, Random Forest (RF), to model the relationships between the SGRC (the response variable) and the seven selected predictors described in the section 2.1.2 (^{220}Rn, CO_2, TGDR, permeability, fault density, slope, and aspect). Random Forest (RF) is an ensemble classifier algorithm developed by Breiman (2001), commonly used for classification and regression problems. It provides an output based on Decision Trees. A Decision Tree is a regression model built through a series of decisions based on variable values, with splitting values chosen to best separate subsets of data along various paths. Random Forest mitigates overfitting by combining multiple Decision Trees created from bootstrap samples of the full training dataset, using subsets of predictors at each split (Rebala et al., 2019).

In this study, we implemented the Random Forest algorithm by using the Scikit-learn module in the Python code.

4.2.6. Radon risk mapping

4.2.6.1. Risk concept

The risk is commonly defined as the product of three factors: hazard, vulnerability and exposure, as expressed Equation 2:

(2) $$Risk = Hazard * Vulnerability * Exposure$$

Hazard represents a specific property that can potentially cause harm or damage to humans. Vulnerability refers to the susceptibility to experience harm due to the stress induced by an event of a certain intensity. Exposure quantifies the number of elements or individuals exposed to the risk (e.g., the number of individuals).

In this study, we identify the GRP as the hazard factor, while land use and population density serve as vulnerability and exposure factors, respectively. Notably, we focus on the concept of collective risk, which pertains to the risk faced by the general public due to geological factors. Applying this risk definition to map CRAs represents an initial and straightforward method to assess collective Rn exposure in the study area. Initially, the GRP mapping serves as a valuable tool for hazard assessment. Furthermore, merging the GRP map with vulnerability and exposure factors, is crucial for evaluating the collective risk.

4.2.6.2. Construction of Collective Risk Areas (CRAs) map

Following Equation 2, we designated the GRP as the hazard factor, while location types and the total population of the census tracts within the study area served as vulnerability and exposure factors, respectively.

In the ISTAT dataset, location types are denoted by numbers representing specific type of building areas, ranging from 1 (residential areas) to 4 (sparse houses). To standardise these location types, reclassified them to assign the highest weight (4) to the area with the highest expected mean population density. The reclassification was as follows: (*i*) location type 4 = residential areas; (*ii*) location type 3 = housing unit; (*iii*) location type 2 = industrial areas; (*iv*) location type 1 = sparse houses.

Next, we utilised the total population and the location type information to compute population density. This involved calculating the ratio of the total population living in a specific location type to the total area (in km^2) of the census tract. Subsequently, we converted the location type and population

density maps into a 50x50 m raster grid and normalised them to their respective maximum value. The GRP map was also normalised similarly.

These three factors were then multiplied using the Raster Calculator tool in ArcGIS Pro, following Equation 2. The resulting risk map underwent further standardisation. To assign a risk value to each polygon of the census tract, we applied the Zonal Statistic tool in Spatial Analyst within ArcGIS Pro. We considered the maximum risk value assigned to the polygon to visualise the risk map and create risk classes. The final risk map is categorised into three risk classes (i.e., low, medium and high) using the natural breaks method and it is numerically expressed as a percentage of risk.

4.3. Results

4.3.1. Selected Predictors, RF Modelling and Predictors Importance

The LASSO regression successfully identified 7 predictors out of the initial 10 candidates: TGDR, CO_2, FD, ^{220}Rn, slope, aspect and soil permeability. These selected predictors, along with their coefficients, are presented in table A1 in the Appendix 2. Notably, three predictors – DTM, solar radiation and Rn dissolved in groundwater – were excluded from the model due to their coefficients equalling 0, indicating their non-informative nature. The final set of predictors includes a geophysical parameter (TGDR), geochemical parameters (^{220}Rn and CO_2), geological parameters (fault density and soil permeability), and geomorphological parameters (slope and aspect). Each of these parameters plays a crucial role in understanding the processes underlying Rn production, migration, and behaviour in shallow soil, as well as interactions at the soil-atmosphere interface.

To ensure there was no redundancy among the selected predictors, we calculated the Variance Inflation Factor (VIF) with all the selected predictors showing VIF < 7 (refer to table A2 in the Appendix 2).

Before executing the RF model, we set the number of decision trees to 1000. The model performance analysis yielded an R^2 value of 0.93 for training data and 0.47 for the test data. The Root Mean Square Error (RMSE) was found to be 0.30 for the training data and 0.83 for the test data. These results are visualised in Figure S4 in the supplementary materials, which displays predicted vs. observed values for training and test data.

To understand the relative influence of individual predictors on model performance, we assessed predictor importance using the RF model (see Figure 2). The variable importance shows that TGDR, CO_2, fault density, ^{220}Rn, slope, aspect and soil permeability have progressively decreased influence on the model performance. In particular, TGDR, a proxy for the Rn source in rocks and soils, and

CO_2, the main carrier gas in the study area (Benà et al., 2022), have importance exceeding 30%, emerging as the most influential predictors. Fault density (FD), a proxy for secondary permeability, showed importance in 10-15% range. ^{220}Rn and slope had an importance of less than 10%, followed by aspect and soil permeability, with less than 5% importance.

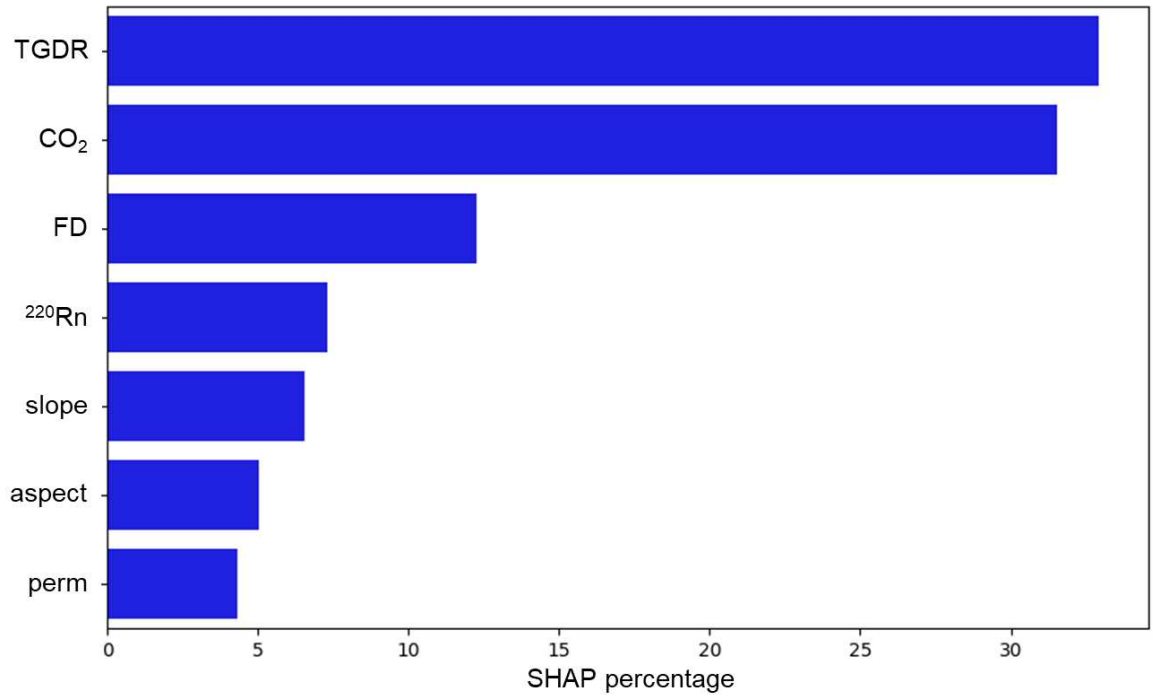

Figure 2. Feature importance based on SHAP value percentage in the RF model. The predictors are ordered by decreasing importance.; X-axis: SHAP percentage; Y-axis = selected predictors. TGDR = Terrestrial Gamma Dose Rate; CO_2 = carbon dioxide; FD = fault density; ^{220}Rn = Thoron; perm = soil permeability.

Furthermore, we constructed SHAP diagrams (SHapley Additive exPlanations) using the "shap" library in Python code to highlight the impact of each selected predictor on model predictions (refer to Figure 3). These diagrams revealed that positive values of TGDR, CO_2, FD, ^{220}Rn, slope, and permeability had the most substantial influence on model output, while aspect was the sole variable exerting a negative impact on the model output.

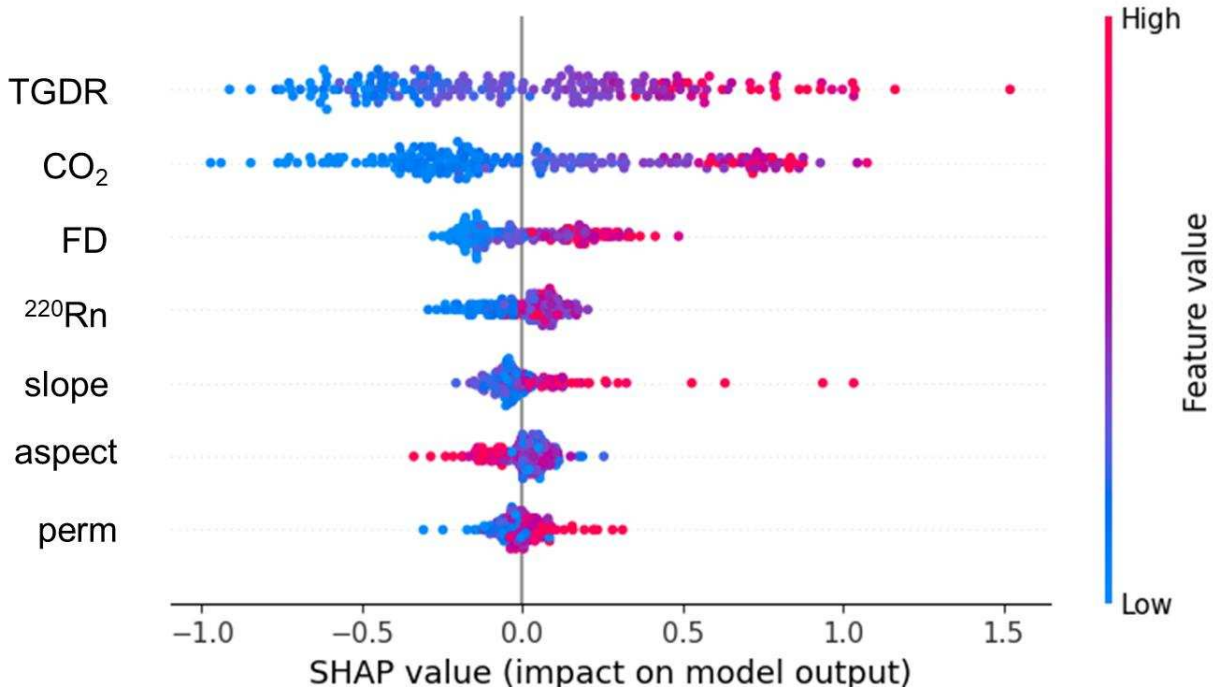

Figure 3. SHAP diagram. The Y-axis of the SHAP diagram reports the 7 selected predictors in descending order of importance in the RF model from TGDR (the most influent) to the soil permeability (the less influent). The X-axis of the SHAP diagram represents the SHAP values quantifying the impact of a single feature on the model's output: positive SHAP values indicate that the feature positively contributes to the output, while negative values suggest a negative contribution. Red and blue dots represent the contribution of individual features to the prediction compared to a reference value. Red dots represent positive contributions and indicate that the feature is increasing the predicted output. Blue dots represent negative contributions and indicate that the feature is decreasing the predicted output. TGDR = Terrestrial Gamma Dose Rate; CO_2 = carbon dioxide; FD = fault density; ^{220}Rn = Thoron; perm = soil permeability.

To examine the relationship between each predictor and the model output more deeply, we generated Partial Dependent Plots using the "pdpbox" library in Python (see Figure 5Aa-g and related explanation in the Appendix 2). PDPs allowed us to visualise the relationship between a target feature and the model outcome while holding all other features constant, aiding in interpreting how each predictor affected the model predictions. The PDPs considered the average effect of other predictors in the model when analysing the relationship of each predictor with the model outcome (Petermann et al., 2021).

4.3.2. Geogenic Radon Potential map

The RF algorithm was employed to create the GRP map of the study area, using SGRC as the response variable and the 7 selected predictors (i.e., TGDR, CO_2, fault density, ^{220}Rn, slope, aspect, soil permeability). The resultant GRP map exhibits a range of values, with a minimum of 7.21 kBq·m^{-3} and a maximum of 182 kBq·m^{-3} (as illustrated in Figure 4). In accordance with results presented in Benà et al. (2022), we consider high GRP values those exceeding 50 kBq·m^{-3}. This threshold corresponds to the local background level in the study area.

The high GRP values delineate a zone extending along the east-west direction from Falzes/Pfalzen to Terento/Terenten, aligning to the direction of the wide fracture zone associated with the Pusteria fault system. Within this area, the high GRP values are attributed to the presence of the Tectonically Enhanced Radon (TER) quantity, as elucidated by Benà et al. (2022).

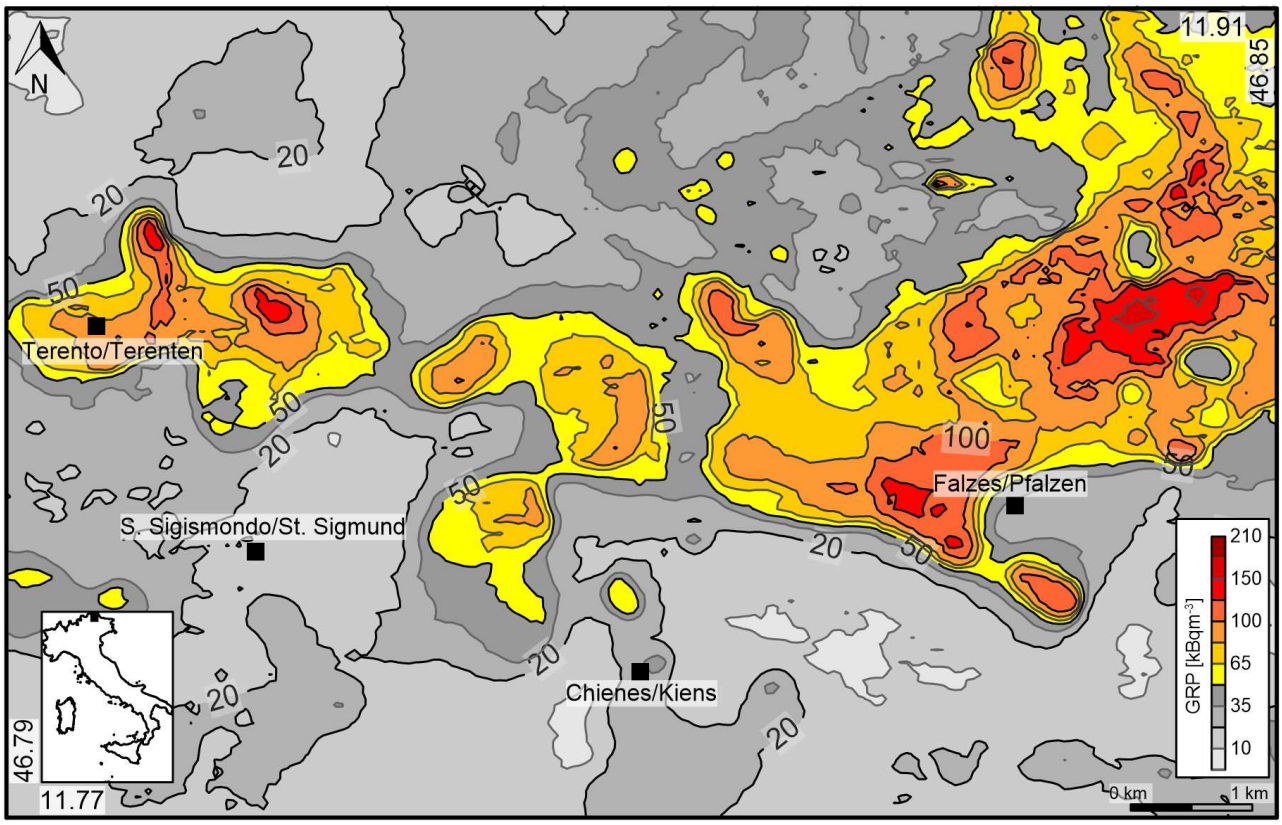

Figure 4. GRP (kBq·m^{-3}) map of the study area.

4.3.3. The Collective Risk Areas (CRAs) map

Figure 5 shows the CRA map of the study area, illustrating the density of collective risk obtained by multiplying the GRP map, the location type (vulnerability factor), and population density (exposure factor).

The map has been divided into three risk classes as follow: (*i*) Risk < 5% (depicted as low risk, indicated by white areas in Figure 5); (*ii*) Risk between 5% and 50% (designated as medium risk, represented in yellow in Figure 5); (*iii*) Risk >50% (considered as high risk, marked in red in Figure 5).

The CRA map is correlated with Table 1, which summarises certain parameters characterising the three defined risk classes: (*i*) the average GRP value in kBq·m^{-3}; (*ii*) the average population density expressed as the number of people per km^2; (*iii*) the location type (i.e., 4, 3, 2, 1); (*iv*) the total area covered by the respective risk class.

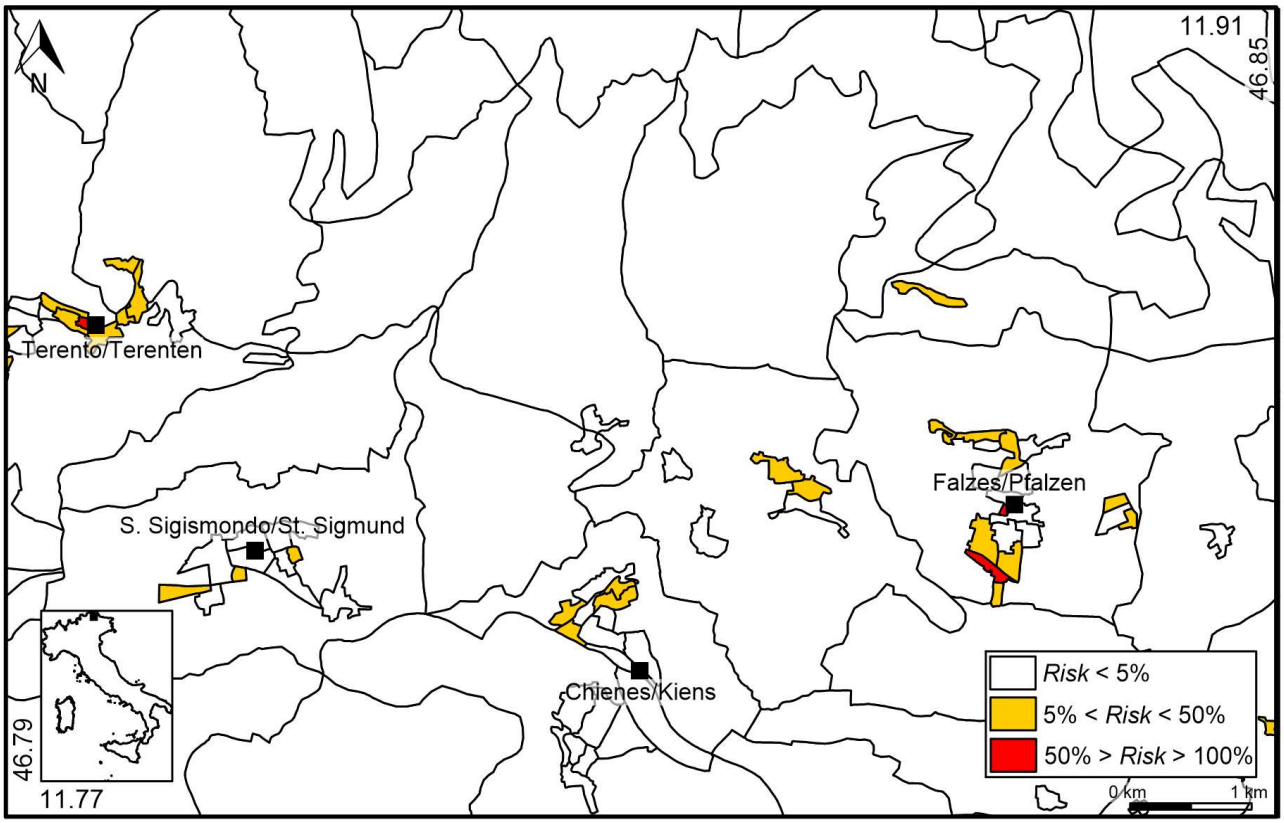

Figure 5. Map of the CRAs in the study area.

Collective risk class	Risk level (%)	GRP mean (kBq·m^{-3})	Population density (people km^{-2})	Population (people)	Location type	Area (km^2)
Low	< 5	63	546	5927	4, 3, 2, 1	68.51
Medium	5 – 50	65	6116	3072	4, 3, 2, 1	0.75
High	> 50	76	17549	622	4	0.05

Table 1. The table reports the risk class and the correspondent percentage of risk, the mean GRP value, the population density, the location type (denoted by numbers representing specific type of building areas,) and the extension of the area covered by the considered risk class.

Most of the study area (68.51 km^2) falls within the low-risk category, consistent with the mountainous terrain where the majority of the population resides in residential areas of the main municipalities, such as Terento/Terenten, Chienes/Kiens and Falzes/Pfalzen.

In general, the mean GRP values (indicating hazard) exceed the local background value of 50 kBq·m^{-3} in all the three risk classes, with a slight increase from low risk (63 kBq·m^{-3}) to high risk (76 kBq·m^{-3}). The progressive increase in mean population density (representing exposure) from low- to high-risk areas is closely related to the location type (reflecting the vulnerability factor): (*i*) in the low-risk areas, most of the census tracts (33) are described as residential areas (location type = 4) and sparse houses (location type = 1, 43 census tracts); (*ii*) in the medium-risk areas, the majority of the census tracts are designated as residential areas (location type 4, 22 census tracts); (*iii*) all census tracts falling

within high-risk areas are described as residential areas (location type = 4) with the highest population density. As a result, the population density increases proportionally from low- to high-risk areas.

4.4. Discussion

4.4.1. Interpretation of predictors in the RF model

The RF model demonstrates that all of the selected predictors influence Rn concentrations and movement in the subsoil. This result is consistent with the dependence of Rn on the geochemical and structural characteristics of the study area, mainly linked to the generation and transport of Rn in the geological environment (i.e., from deep sources toward the subsoil) (Benà et al., 2022). The variable importance clearly shows that GRP is primarily affected by TGDR (35%, Fig. 2), representing the BRS contribution, such as the content of ^{238}U and ^{232}Th radionuclides, from the main outcropping rocks, including gneiss, granite, and phyllite (Tchorz-Trzeciakiewicz et al., 2021; Giustini et al., 2019, 2022). Since the TGDR surveys were conducted at the ground level, its correlation with SGRC is stronger than with atmospheric concentrations. In the literature, also Bossew et al. (2017), Cinelli et al. (2019), Melintescu et al. (2018), and Sainz Fernández et al. (2017) have reported a positive correlation between TGDR and GRP.

The BRS contribution to the Rn amount in soil gas generates a relatively high spatial variability of Rn concentration in the soil gas, reflecting the homogeneous characteristics of the soil or rock environment at the local scale (BRS). However, Rn spatial variability can increase (in particular at local scale) near fault zones (TER), where Rn migration from deeper sources can be enhanced by intense fracturing and the presence of carrier gases, which play a dominant role in the advective transport and redistribution of trace gases at surface (Wilkening, 1980; Ciotoli et al., 2007, 2014; Prasetio et al., 2023, and reference therein). This is observable in the study area along the Pusteria fault system, where radon concentrations in soil gas have a positive correlation with CO_2 concentrations (importance of about 30%, Figure 2), suggesting a possible upward advective flow caused by pressure gradients.

The high importance (about 15%, Fig. 2) of the fault density (interpreted as secondary permeability due to the fault zone) in the RF model confirms the effect of the Pusteria fault system on Rn migration (as well as other gases); this predictor is strictly related to the TER component (Benà et al., 2022). Indeed, damage zones related to high fracturing zones (fault areas) often exhibit a high permeability compared to the surrounding rocks, which may facilitate the advective transport of fluids for SGRC, potentially increasing radon release towards the surface, and consequently, Rn availability to enter

buildings (IRC) (Ciotoli et al., 2007, 2014, 2016; Seminsky et al., 2014; Chen et al., 2018; Banrion et al., 2022; Zhou et al., 2023).

Similar importance of the other predictors (i.e., ^{220}Rn, slope, aspect and soil permeability) ranging from 4% to 8% can be explained by processes affecting Rn movement in the soil layer and at the soil-atmosphere interface (SRE) (Fig. 2). In the shallow environment, the influence of meteorological conditions can be complex, and the literature results are controversial. The influence of air temperature and pressure on soil radon concentration is small in comparison with the total seasonal variability of this gas. In any case, the influence of these two variables is further reduced by conducting soil gas measurement campaigns during periods of stable and good weather conditions (Ciotoli et al., 2014; Beaubien et al., 2013).

The principal drivers governing diurnal and seasonal changes in radon concentration in the soil are the water saturation and moisture retention in the soil pores (i.e., rainfall) (King and Minissale, 1994). These two parameters directly decrease soil permeability thus preventing radon gas diffusion in the shallow soil layers (Nazaroff, 1992; Alonso et al., 2019; Beltran-Torres, 2023). High soil permeability allows ^{220}Rn to be detected at surface despite its short decay time (55.6 seconds).

In addition, the slope can be used as a proxy for soil moisture and meteorological conditions in absence of any other meteorological variables. High slopes also constitute zones characterised by increased soil permeability because they do not promote the retention of water and moisture in the soil pores. On the contrary, flat zones are characterised by low soil permeability because they favour the accumulation of water and moisture in the soil pores. In this regard, the SHAP diagram shows that high values of ^{220}Rn, slope and soil permeability are positively correlated with high GRP (Fig. 3). Soil permeability may be linked to the ability of radon to migrate and escape towards the Earth surface. In fact, where permeability is low, radon escapes more easily; this variable is also linked to the fault density representing the secondary permeability.

All these predictors, except for the aspect, have an impact on the GRP values prediction for positive values and show an increasing trend up to the expected average radon value (see PDPs, in Figure S5 in the supplementary materials). On the contrary, low values of the GRP are correlated with high values of the aspect (i.e., inverse correlation). The aspect identifies the compass direction that the downhill slope faces for each location; therefore, radon accumulation is easier in flat areas.

The model confirmed the correlations between geology and GRP and also provided insight into the utility and significance of other predictors that reflect the physical, chemical, and hydraulic properties of soil, as well as climatic predictors.

4.4.2. Map of the Collective Risk Areas (CRAs)

The GRP map obtained through the RF regression represents the radon hazard due to geological features in a specific region. It is closely related to Rn gas directly measured in the soil and to all geological predictors that significantly influence its concentration in the shallow environment. GRP maps are essential for evaluating Rn risk, as they represent the most significant spatial predictor of IRC (Bossew, 2015; Bossew et al., 2020).

As previously mentioned, the European regulations aim to identify RPAs and implement mitigation plans to limiting radon exposure, thereby reducing the risk of lung cancer for the population. In undeveloped and uninhabited areas, high Rn values represent only a high hazard (i.e., GRP), but not an immediate risk. This concept is well-established and applied in the case of other natural phenomena, such as seismic micro zonation studies.

European legislation seeks to reduce the harm caused by Rn exposure (i.e., the number of lung cancer deaths) and, consequently, reduce collective exposure. Figure 6 illustrates how GRP is a key factor in recognising CRAs.

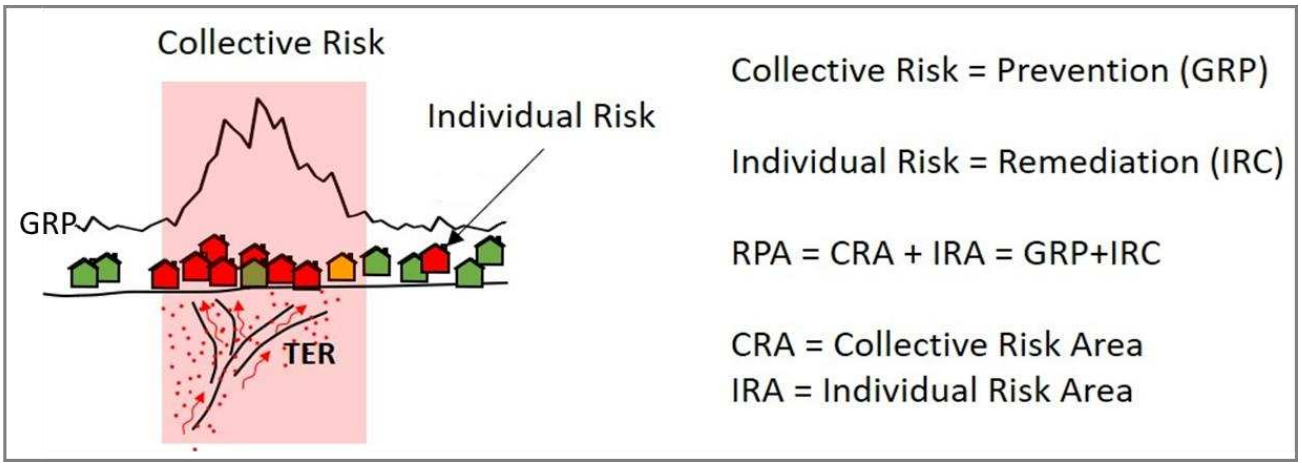

Figure 6. Summary sketch of the CRAs concept.

In this paper, for the first time, we introduce the concept and define CRAs by applying the risk definition (section 2.4). Mapping the GRP is undoubtedly the crucial first step in defining the Rn hazard, a specific property that cannot be mitigated. For this reason, it is important to map it as accurately as possible, considering multiple geological variables and employing robust mapping techniques.

As reported in Benà et al., 2022, Rn values exceeding the lithological background (50 kBq·m^{-3}) are considered anomalous and linked to the wide fracturing zone of the Pusteria fault system, which represents Rn enhanced due to tectonics (TER). However, in Benà et al. (2022), this aspect is not

discussed in terms of GRP, and it does not consider other important geological factors, such as gas permeability and indicators of deep circulation (e.g., Rn in groundwater), as well as the shallow effects governed by the morphological parameters (e.g., DTM).

The identification of a specific threshold value of GRP is not significant for delineating CRAs since the indoor radon risk exists even for "very low" concentrations of radon in the soil and, consequently, for very low GRP values. In fact, radon measured in the soil (GRP) is generally three orders of magnitude higher than indoor radon. It is evident that every area can be affected by potential indoor risk, and all dwellings are considered vulnerable.

However, GRP plays a key role in defining CRAs, primarily occurring along the Pusteria fault system where Rn degassing is enhanced by intense fracturing, resulting in high GRP values. This aligns with the fact that all the GRP values contribute to the risk. Therefore, the CRAs map highlights areas with low, medium and high collective risk, where IRC values may be high for residential areas.

4.5. Conclusions

The mapping and analysis of GRP (e.g., Rn hazard) serve as fundamental tools for delineating CRAs according to a new, more geological interpretation of RPAs, as compared to that outlined in the BSS directive (2013/59/EURATOM).

We used a risk formula to combine the GRP map, obtained through ML approaches, with characteristics of the census tracts as location type (the vulnerability factor) and population density (the exposure factor).

In alignment with a geological-based interpretation of RPAs, we can recognise hazard-based RPAs (CRAs) and detriment-based RPAs (IRAs) as complementary concepts within territorial planning and remediation actions, respectively, rather than alternatives.

Our findings lead to the following conclusions:

- The use of the random forest algorithm as a ML model proved to be robust and highly effective for generating a GRP map of the study area. This GRP map incorporated seven predictors, reflecting geological factors (BRS and TER), soil characteristics (groundwater circulation, soil permeability), and meteorological conditions (DTM derivatives). The variable importance analysis highlighted the dominant impact of the Rn source while still showing significant contributions from other predictors.

- Since GRP is considered the most critical spatial predictor of IRC, it is evident that an accurate mapping of this hazard factor effectively represents the total amount of radon that could potentially enter buildings.
- Given that GRP (e.g., soil gas concentration) values are three orders of magnitude higher than IRC, there is no reason to establish a specific GRP threshold. Indoor radon risk can exist even for "very low" concentrations of radon in the soil and, consequently, for very low GRP values. Qualitative GRP classes can serve as delineation of zones, akin to how they are used in seismic micro zonation studies, guiding land-use planning strategies, construction types, and remediation actions.
- The construction of GRP maps is a crucial tool for both Rn hazard and risk analysis. It forms the foundation for identifying RPAs, particularly under a new, more geological perspective. This is essential for collective risk assessment, including land-use planning and prevention, as well as individual risk assessment, aiding in strategic planning for indoor surveys, and specific remediation actions.
- The absence of clear guidelines for defining RPAs necessitates the geological-based conceptualization of a complementary approach to mapping both CRAs (for prevention), and IRAs (for building remediation actions).

This study may assist policymakers in implementing preventive measures in areas where new buildings are planned and in taking remediation actions in RPAs *sensu stricto*. Future studies could aim to define effective individual risk by constructing statistical models that also consider IRC measurements and anthropogenic factors.

References

Alonso, H., Rubiano, J. G., Guerra, J. G., Arnedo, M. A., Tejera, A., Martel, P. Assessment of radon risk areas in the Eastern Canary Islands using soil radon gas concentration and gas permeability of soils Sci. Total Environ., 664 (2019), pp. 449-460, 10.1016/j.scitotenv.2019.01.411

Banrion M.H., Elio J., Crowley Q.G. (2022). Using geogenic radon potential to assess radon priority area designation, a case study around Castleisland, Co. Kerry, Ireland. Journal of Environmental Radioactivity Volumes 251–252, October 2022, 106956, doi: 10.1016/j.jenvrad.2022.106956

Beaubien S.E.; Ruggiero L.; Annunziatellis A.; Bigi S.; Ciotoli G.; Deiana P.; Graziani S.; Lombardi S.; Tartarello C (2013). The importance of baseline surveys of near-surface gas geochemistry for CCS monitoring, as shown from onshore case studies in northern and southern Europe. Oil and Gas Science Technology Journal, Rev. IFP Energies nouvelles, Copyright © 2014, IFP Energies nouvelles, DOI: 10.2516/ogst/2014009

Beltran-Torres S., Szabo K.Z., Toth G., Bodrogi E.T., Tibor Kovacs T., Szabo C. (2023). Estimated versus field measured soil gas radon concentration and soil gas permeability. Journal of Environmental Radioactivity, 265, 107224.

Benà, E., Ciotoli, G., Ruggiero, L. Coletti, C., Bossew, P., Massironi, M., Mazzoli, C., Mair, V., Morelli, C., Galgaro, A., Morozzi P., Tositti, L., Sassi, R. Evaluation of tectonically enhanced radon in fault zones by quantification of the radon activity index. Sci Rep 12, 21586 (2022). https://doi.org/10.1038/s41598-022-26124-y

Benavente D., Valdés-Abellán J., Pla C., Sanz-Rubio E. (2019). Estimation of soil gas permeability for assessing radon risk using Rosetta pedotransfer function based on soil texture and water content. Journal of Environmental Radioactivity, 208-209, doi: 10.1016/j.jenvrad.2019.105992

Borsi S., Del Moro A., Sassi F.P., Zanferrari A., Zirpoli G. (1978). New geopetrologic and radiometric data on the Alpine history of the Austridic continental margin south of the Tauern Window (Eastern Alps). Mem. Sci. Geol. Univ. Padova, 32, 1 -17.

Bossew P. 2018 Radon priority areas definition, estimation and uncertainty Nucl. Technol. Radiat. Prot. 33 286–92 (2018)

Bossew P., Suhr N. European radon abatement policy: state and ongoing discussion. Brazilian Journal of Radiation Sciences 11-1A (Suppl.) (2023) DOI: https://doi.org/10.15392/2319-0612.2023.2162; https://bjrs.org.br/revista/index.php/REVISTA/article/view/2162

Bossew, P., Cinelli, G., Hernández-Ceballos, M., Cernohlawek, N., Gruber, V., Dehandschutter, B., Menneson, F., Bleher, M., Stöhlker, U., Hellmann, I., Weiler, F., Tollefsen, T., Tognoli, P.V., de Cort, M. Estimating the terrestrial gamma dose rate by decomposition of the ambient dose equivalent rate. J. Environ. Radioact. 166, 296–308. (2017). Doi: 10.1016/J.JENVRAD.2016.02.013.

Bossew, P., 2015. Mapping the geogenic radon potential and estimation of radon prone areas.

Bossew, P., Cinelli, G., Ciotoli, C., Crowley, Q. G., De Cort, M., Medina, J. E., Gruber, V., Petermann, E., Tollefsen, T. Development of a Geogenic Radon Hazard Index – Concept, History, Experiences. Int. J. Environ. Rs. Public Health, 17, 4134 (2020).

Bossew, P., Petermann E. What is the objective of radon abatement policy? Revisiting the oncept of radon priority areas. 15th GARRM. International workshop on the geological aspects of radon risk mapping. 21 – 24 Sept 2021, Prague, Czech Republic

Breiman, L., 2001. Random forests. Mach. Learn. 45, 5–32.

Castelluccio, M., De Simone, M., Lucchetti, C., Moroni, M., Salvati, F., Tuccimei, P. A new technique to measure in situ soil gas permeability. Journal of Geochemical Exploration. 148, 56–59 (2015). http://dx.doi.org/10.1016/j.gexplo.2014.08.002

Chen, Z. et al. Radon emission from soil gases in the active fault zones in the capital of China and its environmental effects. Sci. Rep. 8, 16772. https://doi.org/10.1038/s41598-018-35262-1 (2018).

Cinelli, G., Tollefsen, T., Bossew, P., Gruber, V., Bogucarskis, K., De Felice, L., De Cort, M., 2019. Digital version of the European Atlas of natural radiation. J. Environ. Radioact. 196, 240–252. https://doi.org/10.1016/J.JENVRAD.2018.02.008.

Cinelli, G., Tositti, L., Capaccioni, B. et al. Soil gas radon assessment and development of a radon risk map in Bolsena, Central Italy. Environ Geochem Health 37, 305–319 (2015). https://doi.org/10.1007/s10653-014-9649-9

Ciotoli, G., Lombardi, S., Annunziatellis, A. Geostatistical analysis of soil gas data in a high seismic intermontane basin: Fucino Plain, central Italy. Journal of Geophysics. 112, B05407 (2007). http://dx.doi.org/10.1029/2005JB004044.

Ciotoli, G., Procesi, M., Etiope, G. et al. Influence of tectonics on global scale distribution of geological methane emissions. Nat Commun 11, 2305 (2020). https://doi.org/10.1038/s41467-020-16229-1

Ciotoli, G., S. Bigi, C. Tartarello, P. Sacco, S. Lombardi, A. Ascione, and S. Mazzoli (2014), Soil gas distribution in the main coseismic surface rupture zone of the 1980, Ms = 6.9, Irpinia earthquake (southern Italy), J. Geophys. Res. Solid Earth, 119, 2440–2461, doi:10.1002/2013JB010508.

Ciotoli, G., Sciarra, A., Ruggiero, L., Annunziatellis, A. & Bigi, S. Soil gas geochemical behaviour across buried and exposed faults during the 24 August 2016 central Italy earthquake. Ann. Geophys. https://doi.org/10.4401/ag-7242 (2016).

Ciotoli, G., Voltaggio, M., Tuccimei, P., Soligo, M., Pasculli, A., Beaubien, S.E., Bigi, S. Geographically weighted regression and geostatistical techniques to construct the geogenic radon potential map of the Lazio region: a methodological proposal for the European atlas of natural radiation. J. Environ. Radioact. 166, 355–375 (2017).

Coletti C., Ciotoli G, Benà E., Brattich E., Cinelli G., Galgaro A., Massironi M., Mazzoli M., Mostacci M., Mozzi P., Nava J., Ruggiero L., Sciarra A., Tositti L., Sassi R. The Geogenic Radon Potential by using the Empirical Bayesian Regression Kriging. The Euganean Hills district (Italy). Science of Total Environment 808, 152064, (2022). doi: 10.1016/j.scitotenv.2021.152064.ù

Decreto Legislativo 31 luglio 2020, n. 101 (Attuazione Direttiva 2013/59/EURATOM), Gazzetta Ufficiale della Repubblica Italiana, Serie Generale n. 201 del 12-08-2020- Suppl. Ordinario n. 29.

Durrant J.T., Gee K.L., Anderson M.C., Cook M.R., Loubeau A. (2021). Preliminary lasso regression analysis of environmental effects on sonic boom metric variability. J Acoust Soc Am 150, A259 (2021). doi: 10.1121/10.0008215

European Union, Council Directive 2013/59/Euratom of 5 December 2013 laying down basic safety standards for protection against the dangers arising from exposure to ionising radiation, and repealing Directives 89/618/Euratom, 90/641/Euratom, 96/29/Euratom, 97/43/Euratom and 2003/122/Euratom. Official J. Eur. Union, OJ L13, 17.01.2014 (2013) 1–73. Official J. Eur. Union, OJ L13, 17.01.2014 (2013) 1–73.

Fouedjio, F., Klump, J., 2019. Exploring prediction uncertainty of spatial data in geostatistical and machine learning approaches. Environ. Earth Sci. 78 (1), 38. https://doi.org/10.1007/s12665-018-8032-z.

Fu, C. C., T. F. Yang, V. Walia, and C.-H. Cheng (2005), Reconnaissance of soil gas composition over the buried fault and fracture zone in southern Taiwan, Geochem. J., 39, 427–439.

Giustini F, Ruggiero L, Sciarra A, Beaubien S., Graziani S, Galli G, Pizzino L, Tartarello MC, Lucchetti C, Sirianni P, et al. Radon Hazard in Central Italy: Comparison among Areas with Different Geogenic Radon Potential. International Journal of Environmental Research and Public Health. 2022; 19(2):666. https://doi.org/10.3390/ijerph19020666Castelluccio, M., De Simone, G.,

Giustini, F., Ciotoli, G., Rinaldini, A., Ruggiero, L., Voltaggio, M., 2019. Mapping the geogenic radon potential and radon risk by using empirical Bayesian kriging regression: a case study from a volcanic area of Central Italy. Sci. Total Environ. 661, 449–464.

Giustini, F.; Ruggiero, L.; Sciarra, A.; Beaubien, S.E.; Graziani, S.; Galli, G.; et al. Radon Hazard in Central Italy: Comparison among Areas with Different Geogenic Radon Potential. Int. J. Environ. Res. Public Health. 19, 666 (2022). https://doi.org/10.3390/ijerph19020666.

Griffiths, A.; Conen, F.; Weingartner, E.; Zimmermann, L.; Chambers, S.; Williams, A.; Steinbacher, M. Surface-to-mountaintop transport characterised by radon observations at the Jungfraujoch. Atmos. Chem. Phys. 2014, 14, 12763–12779.

Gundersen, L.C.; Schumann, R.R.; Otton, J.K.; Dubiel, R.F.; Owen, D.E.; Dickinson, K.A. Geology of radon in the United States. Geol. Soc. Am. Spec. Pap. 1992, 271, 1–16.

Handorf E., Yin Y., Slifker M., Lynch S. (2020). Variable selection in social-environmental data: sparse regression and tree ensemble machine learning approaches. BMC Med Res Methodol 20, 302 (2020). doi:10.1186/s12874-020-01183-9

Hengl, T., MacMillan, R.A., 2019. Predictive Soil Mapping with R. OpenGeoHub foundation, Wageningen, the Netherlands, p. 370.

Hengl, T., Mendes de Jesus, J., Heuvelink, G.B.M., Ruiperez Gonzalez, M., Kilibarda, M., Blagotić, A., et al., 2017. Soil Grids 250m: global gridded soil information based on machine learning. PLoS One 12, e0169748.

Huynh Nguyen, P.T., Nguyen, V.T., Vu, N.B., Nguyen, V.D., Le Cong, H. Soil radon gas in some soil types in the rainy season in Ho Chi Minh City, Vietnam. J. Environ. Radioact., 193–194 (2018), pp. 27-35, 10.1016/j.jenvrad.2018.08.017

Iovine, G., Guagliardi, I., Bruno, C. et al. Soil-gas radon anomalies in three study areas of Central-Northern Calabria (Southern Italy). Nat Hazards 91 (Suppl 1), 193–219 (2018). https://doi.org/10.1007/s11069-017-2839-xJanik, M., Bossew, P., Kurihara, O., 2018. Machine learning methods as a tool to analyse incomplete or irregularly sampled radon time series data. Sci. Total Environ. 630, 1155–1167.

Keim, L., Mair, V., Morelli, C. Inquadramento geologico regionale in: Guida ai percorsi geologici Foglio 026 Appiano. Ufficio Geologia e prove materiali, Provincia Autonoma di Bolzano, LAC Firenze. ISBN978-88-7914-678-4 (2013).

King C.Y. & Minissale, A. (1994). Seasonal variability of soil-gas radon concentration in central California (San Andreas fault). Radiation measurements, 23, 683-692

Lara E, Rocha Z, Santos TO, Rios FJ, Oliveira AH. Soil Features and Indoor Radon Concentration Prediction: Radon in Soil Gas, Pedology, Permeability and (226) Ra Content. Radiat Prot Dosim. 2015; 167 (1–3):126–9.

Li, J., Siwabessy, P.J., Huang, Nichol, 2019. Developing an optimal spatial predictive model for seabed sand content using machine learning, geostatistics, and their hybrid methods. Geosciences 9, 180.

Lucchetti, C., Moroni, M., Salvati, F., Tuccimei, P. A new technique to measure in situ soil gas permeability. Journal of Geochemical Exploration, 148, 56-59, 2015. http://dx.doi.org/10.1016/j.gexplo.2014.08.002

Melintescu, A., Chambers, S.D., Crawford, J., Williams, A.G., Zorila, B., Galeriu, D., 2018. Radon-222 related influence on ambient gamma dose. J. Environ. Radioact. 189, 67–78. https://doi.org/10.1016/j.jenvrad.2018.03.012.

Micheletti, N., Foresti, L., Robert, S., Leuenberger, M., Pedrazzini, A., Jaboyedoff, M., et al., 2014. Machine learning feature selection methods for landslide susceptibility mapping. Math. Geosci. 46, 33–57.

Minach, L., Verdi, L., Marchesoni, C., Amadori, C. Radon in Alto Adige. Agenzia per la Protezione dell'Ambiente di Bolzano, Laboratorio di chimica fisica, (1999).
Müller W., Mancktelow Ns., Meir M. (2000). Rb-Sr microchrons of synkinematic mica in mylonites: an example from the DAV fault in Eastern Alps. Earth Planet. Sci. Lett., 1880, 385-397.Nazaroff, W. W.: Radon transport from soil to air, Rev. Geophys., 30, 137–160, 1992. https://doi.org/10.1029/92RG00055
Neznal M, Neznal M. Permeability as an important parameter for radon risk classification of foundation soils. Annals of Geophysics. 2005; 40(1):175–80.
Neznal, M., Neznal, M., Matolin, M., Barnet, I., Miksova, J., 2004. The new method for assessing the radon risk of building sites. Czech Geol. Survey Special Papers. 16. Czech Geol. Survey.
Nuhu H, Hashim S, Aziz Saleh M, Syazwan Mohd Sanusi M, Hussein Alomari A, Jamal MH, et al. (2021) Soil gas radon and soil permeability assessment: Mapping radon risk areas in Perak State, Malaysia. PLoS ONE 16(7): e0254099. https://doi.org/10.1371/journal.pone.0254099
Nussbaum, M., Spiess, K., Baltensweiler, A., Grob, U., Keller, A., Greiner, L., et al., 2018. Evaluation of digital soil mapping approaches with large sets of environmental covariates. Soil 4, 1–22.
Pásztor, L., Szabó, K.Z., Szatmári, G., Laborczi, A., Horváth, Á., 2016. Mapping geogenic radon potential by regression kriging. Sci. Total Environ. 544, 883–891.
Petermann, E., Bossew, P., Hoffmann, B. Radon hazard vs. radon risk – on the effectiveness of radon priority areas. Journal of Environmental Radioactivity 244-245, 106833 (2022).
Petermann, E., Meyer, H., Nussbaum, M., Bossew, P. Mapping the geogenic radon potential for Germany by machine learning. Science of Total Environment, 754 – 142291, 2021. https://doi.org/10.1016/j.scitotenv.2020.142291
Prasetio, R., Laksminingpuri, N., Satrio Satrio, Pujiindiyati, E.R., Pratikno, B., Sidauruk, P. (2023). The 222Rn and CO2 soil gas distribution at Lembang Fault Zone, West Java – Indonesia. Journal of Environmental Radioactivity, Volume 257, February 2023, 107079, doi: 10.1016/j.jenvrad.2022.107079
Rebala, G., Ravi, A., Churiwala, S. (2019). Machine Learning Definition and Basics. In: An Introduction to Machine Learning. Springer, Cham. https://doi.org/10.1007/978-3-030-15729-6_1.
Sainz Fernández, C., Quindós Poncela, L.S., Fernández Villar, A., Fuente Merino, I., Gutierrez-Villanueva, J.L., Celaya González, S., Quindós López, L., Quindós López, J., Fernández, E., Remondo Tejerina, J., Martín Matarranz, J.L., García Talavera, M., 2017. Spanish experience on the design of radon surveys based on the use of geogenic information. J. Environ. Radioact. 166, 390–397. https://doi.org/10.1016/j. jenvrad.2016.07.007.
Sassi F.P., Cesare B., Mazzoli C., Peruzzo L., Sassi R., Spiess R. (2004). The crystalline basements of the Italian Eastern Alps: a review of the metamorphic features. In: Castelli D. and Cesare B. (Eds.) "Advances in Metamorphic Petrology: browsing through Italian classic areas, case studies, and approaches", Per. Mineral. Special Issue 2, 23-42. ISSN: 0369-8963.
Schmid S.M., Aebli H.R., Heller F., Zinng A. (1989). The role of the Periadriatic Line in the tectonic evolution of the Alps. Geol. Soc. London, Spec. Publ., 45, 153-171.Seminsky, KZh., Bobrov, A. A. & Demberel, S. Variations in radon activity in the crustal fault zones: Spatial characteristics. Phys. Solid Earth 50(6), 795–881. https://doi.org/10.1134/S1069351314060081 (2014).
Silverman, B.W. (1986) Density Estimation for Statistics and Data Analysis. Chapman & Hall, London. http://dx.doi.org/10.1007/978-1-4899-3324-9
Spiess R., Cesare B., Mazzoli C., Sassi R., Sassi F.P. (2010). The crystalline basement of the Adria microplate in the eastern Alps: a review of the palaeostructural evolution from the Neoproterozoic to the Cenozoic. Rend. Fis. Acc. Lincei, 21, (Suppl 1), 31-50, doi:10.1007/s12210-010-0100-6
Sukanya, S.; Noble, J.; Joseph, S. Factors controlling the distribution of radon (222Rn) in groundwater of a tropical mountainous river basin in southwest India. Chemosphere 2021, 263, 128096
Tchorz-Trzeciakiewicz, D. E., Rysiukiewicz, M. (2021). Ambient gamma dose rate as an indicator of geogenic radon potential. Science of the Total Environment, 755, 142771, doi: 10.1016/j.scitotenv.2020.142771
Tehrani, F.S., Calvello, M., Liu, Z. et al. Machine learning and landslide studies: recent advances and applications. Nat. Hazards 114, 1197–1245 (2022). https://doi.org/10.1007/s11069-022-05423-7.
Tibshirani, R. (1996). Regression shrinkage and selection via the lasso. Journal of the Royal Statistical Society: Series B (Methodological), 58(1), 267–288.
Tibshirani, R. (2011). Regression shrinkage and selection via the lasso: a retrospective. J. R. Statist. Soc. B (2011) 73, Part 3, pp. 273–282
Verdi, L. Weber, A. Stoppa, G. Indoor radon concentration forecasting in South Tyrol. Radiation Protection Dosimetry, 111(4), pp. 435 438 (2004)

Wilkening, M. Radon transport processes below the Earth's surface. In The Natural Radiation Environment, III; US Department of Energy: Washington, DC, USA, 1980; pp. 90–104

Yang, J., Busen, H., Scherb, H., Hürkamp, K., Guo, Q., Tschiersch, J. Modeling of radon exhalation from soil influenced by environmental parameters. Science of The Total Environment, Volume 656, Pages 1304-1311 (2019). ISSN 0048-9697, https://doi.org/10.1016/j.scitotenv.2018.11.464.

Zalloni, E., Battipaglia, G., Cherubini, P. et al. Site conditions influence the climate signal of intra-annual density fluctuations in tree rings of Q. ilex L. Annals of Forest Science 75, 68 (2018). https://doi.org/10.1007/s13595-018-0748-0

Zeeb, H. & Shannoun, F. (eds.). WHO handbook on indoor radon - a public health perspective (2009). ISBNS 978 92 4 154767. https://www.who.int/publications/i/item/9789241547673

Zhou H., Su H., Li C., Wan Y. (2023). Geochemical precursory characteristics of soil gas Rn, Hg, H2, and CO2 related to the 2019 Xiahe Ms5.7 earthquake across the northern margin of West Qinling fault zone, Central China. Journal of Environmental Radioactivity, 264, 107190, doi: 10.1016/j.jenvrad.2023.107190

5. Chapter 3:

Rock deformation *vs.* radon emission: some constraints from shear stress-controlled experiments

Abstract

Numerous field and laboratory studies have been conducted to investigate the relationship between radon variation and seismic events, as well as the complex link between radon emission and rock deformation mechanisms. However, a clear understanding of this correspondence and systematic observations of these phenomena are still lacking, and recent experimental studies have yet to yield conclusive results. In this study, we investigate the possible relationships between radon migration dynamics and rock deformation at the micro-scale through laboratory experiments using the SHIVA apparatus under shear stress-controlled conditions and simultaneous high-resolution radon measurements. We studied the behaviour of three different lithologies to show that radon emission varies in response to rock deformation and this variation is highly dependent on the mineralogy and microstructure. This study represents the first attempt to define radon gas as an indicator of transient and rapid rock deformation at the micro-scale.

Benà, E.[1], Spagnuolo, E.[2], Piersanti, A.[2], Galli, G.[2], Mazzoli, C.[1], Sassi, R.[1]

[1]Department of Geosciences, University of Padova, Italy
[2]Istituto di Geofisica e Vulcanologia (INGV), Rome, Italy

A slightly different version of this chapter is published in *Scientific Reports* (Benà et al., 2023).

Authorship contribution statement:
E.B. conceptualization, samples collection and preparation, shear stress-controlled experiments, data curation, writing original draft preparation, reviewing and editing; **E.S.** samples preparation, shear stress-controlled experiments, data curation, reviewing and editing; **A.P.** Rn-detector experimental set-up, change point analysis, reviewing and editing; **G.G.** Rn-detector experimental set-up, reviewing and editing; **C.M.** conceptualization, samples collection, petrographic analysis, reviewing and editing; **R.S** conceptualization, supervision, samples collection, petrographic analysis, reviewing and editing, project administration, funding acquisition.

5.1. Introduction

Radon (^{222}Rn) is one of the most studied radioelements due to its harmful effect on human health and its significance in understanding the migration through more permeable pathways, such as faults and fractures, within the Earth's crust and toward the Earth surface. Despite its short half-life (i.e., 3.8 days) Rn can migrate long distances along faults and it is detectable even in very low concentration in the soil gas. Over the years, numerous field studies have been conducted on Rn behaviour and variation in response to seismic events to evaluate possible relationships. There are many examples of these kind of applications in the literature, including fault localization from Rn concentration enhancement (Wang et al., 2014); the use of spatial Rn concentration and numerical simulation of Rn transport to delineate fault geometry (Koike et al., 2009); change in Rn concentration in soil gas and dissolved in groundwater before, during, and after earthquakes (Wakita, 1996; Jordan et al., 2011); and the correlation between Rn concentration of soil gas at an active fault, which is sensitive to cumulative recent seismicity (Koike et al., 2014).

However, unambiguous and systematic data/observations of a possible (causal) relationship between Rn and those phenomena are still lacking. To this end, laboratory experiments play a key role in understanding the complex relationship between Rn geochemical behaviour and rock deformation mechanisms, as experiments offer a unique opportunity for direct access to the source of Rn. Recent experimental studies include experiments run to test the role of temperature, compression and fracture (Tuccimei et al., 2010, 2015; Mollo et al., 2011; Scarlato et al., 2013; Nicolas et al., 2014; Koike et al., 2015; Cannelli et al., 2016), but are still not conclusive on the role of the applied deformation at close to natural seismic cycle deformation conditions.

In this research, we investigate the possible relationships between radon migration dynamics and rock deformation through laboratory experiments using the rotary shear apparatus SHIVA (Slow to HIgh Velocity Apparatus, see Di Toro et al. 2010) under shear stress-controlled conditions ("torque tests", see Cornelio et al., 2019, for details) on a pre-existing fracture in frictional contact under a constant normal stress and simultaneous continuous radon measurements using forced air circulation in a closed system from the sample holder to the radon-detector, in the absence of any other type of fluid transport. We studied the behaviour of three lithologies (paragneiss, granite and orthogneiss) characterised by different mineralogic composition and microstructure. The rock types were sampled from the crystalline basement of the Pusteria Valley (north-eastern Alps, Bolzano, Italy), a well-known area from a geological and structural point of view. In particular, the lithologies belong to the main outcrops along the Pusteria fault system characterised by a wide fractured zone and a high gas permeability (Benà et al., 2022). This work combines:

- observations derived from rock deformation tests and continuous radon monitoring;
- high resolution (i.e. high sampling frequency) Rn time series analysis through robust statistical approach;
- petrographic analysis of mineral phases and microstructure by optical microscope.

This study represents the first attempt to relate variations in radon gas (measured at high frequency-approximately 1 Hz) through alpha decays in a closed loop system, lithology (by testing three different mineral assemblages from the same natural case study) and rock deformation (under seismic deformation condition at shallow depth) at the micro-scale.

5.2. Methods

5.2.1. Petrographic analysis

Rock samples of paragneiss, granite and orthogneiss were collected from the crystalline basement located in the Pusteria Valley (north-eastern Alps, Bolzano Province, Italy). The collected samples were thin-sectioned to a thickness of 30 μm and analysed using a polarising transmitted-light optical microscope.

5.2.2. Shear stress-controlled experiments

The experiments were conducted using two samples of paragneiss, granite and orthogneiss. Each rock sample was drilled into two bare-rock cylinders with an external diameter of 50 mm. The bare-rock cylinders were then fixed into aluminium jackets using an inert glue (H40 Kerakoll). Furthermore, the rock samples within the jacket were rectified using a lathe to ensure parallelism of the contact surfaces (Nielsen et al., 2010) representing the experimental fault under investigation. The rock samples were initially placed in a pressure-vessel (Violay et al., 2013), a stainless-steel device built on the rotary shear apparatus SHIVA (Slow to High Velocity Apparatus) located in the High Pressure-High Temperature (HPHT) laboratory at the *Istituto Nazionale di Geofisica e Vulcanologia* (INGV) in Rome (Italy). The experimental setup is shown in figure 1. The pressure vessel was equipped with two Teflon O-rings to ensure complete isolation of the rock samples from the external environment. Inlet and outlet valves were connected to the radon detector, creating a closed-loop system that maintained consistent moisture and temperature conditions.

Regarding the shear stress-controlled experiments, the SHIVA apparatus is capable of simulating the seismic cycle under conditions that approximate natural seismic deformation at depths typical of the shallow upper crust. Initially, the prepared bare-rock samples were brought into frictional contact

under a constant normal stress of 5 MPa. Subsequently, the pressure vessel was assembled on SHIVA and connected to the radon detector in a closed loop (Fig. 1). Two experiments were conducted per lithology on SHIVA apparatus to ensure data reproducibility and investigate the radon response to deformation using a shear stress-control protocol (Cornelio et al., 2019). These tests proved particularly useful in studying radon dynamics in a fault system due to sample deformation and evaluating its behaviour near a seismic instability.

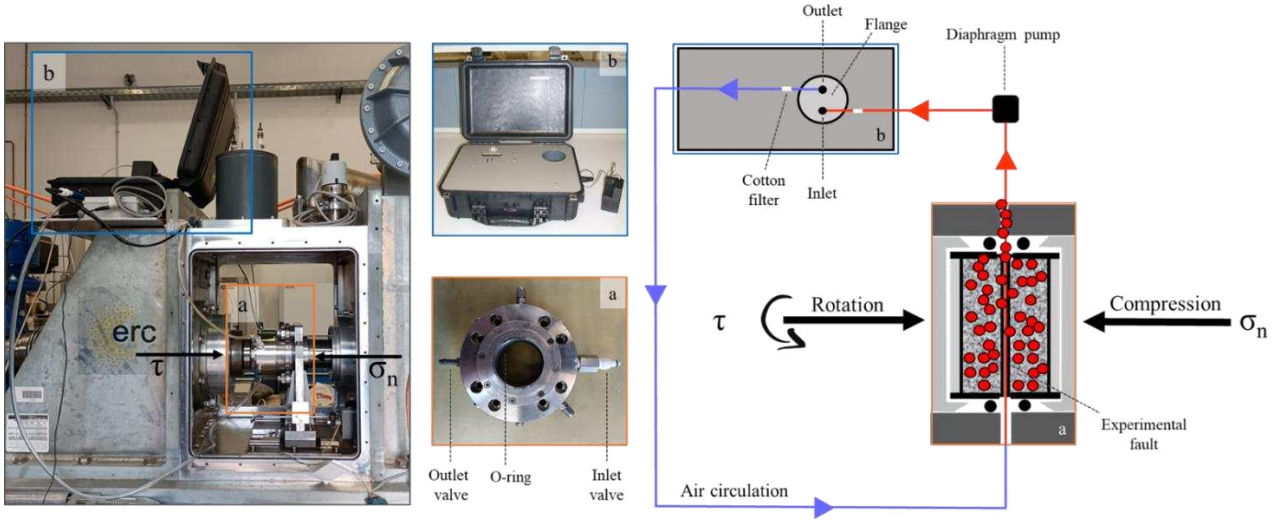

Figure 1. The experimental setup. In the right panel is shown a schematic representation of the experimental setup consisting of (**a**) the pressure-vessel connected with polyethylene tubes with (**b**) the radon detector in a closed loop system. Both were built on the rotary shear apparatus SHIVA made of a rotary axis (τ, rotation) and a stationary axis (σ_n, compression). The air flux is forced from the pressure-vessel to the radon detector with a diaphragm pump (black square). The blue line represents the air circulation in the closed loop; specifically, the red line represents the sensible air volume < 10 ml. In the central panel is reported a zoom of the (**a**) pressure vessel provided with two Teflon O-rings to isolate the sample assembly; inlet and outlet valves; (**b**) the radon detector.

The shear stress-controlled experiments (Table 1) involved a step-wise increase in the shear stress (0.5 MPa, in a time interval of 30 min) under a constant normal stress of 5 MPa. The slip and velocity evolved spontaneously to adjust the stress state on the experimental fault. The stress stepping concluded at sample failure, characterised by fault weakening, stress drop and rapid rotation of the rotary column of the SHIVA apparatus. During this step which we referred to as the "main instability", the velocity increased up to a manually set target velocity of 1 m/s. Prior to the main instability, other types of slip instability such as accelerated creep or fast but self-arresting events, were detected, resulting in slip velocities reaching a few cm/s (reported as Fast events in "Notes" in Table 1). After the experiments, the contact surface of the two samples were heavily damaged, making the sample recovery not possible. The damage of the surface explains the erratic trends observed in axial shortening and the measured normal and shear stress over time.

Experiment	Lithology	Normal stress (MPa)	Shear stress (MPa)	Notes
s1896	Paragneiss	5	0.5/30 min	
s1904	Paragneiss	5	0.5/30 min	Sign error in the manual step
s1895	Granite	5	0.5/30 min	Fast event; error overheating
s1897	Granite	5	0.5/30 min	
s1916	Orthogneiss	5	0.5/30 min	Fast event, lag in shortening
s1917	Orthogneiss	5	0.5/30 min	Fast event

Table 1. The six experiments on the three lithologies and the applied experimental parameters.

5.2.3. Real-time radon time series

Initial Rn counts and variations during the experiments were acquired using an alpha scintillation radon detector (Lucas Cell, Fig. 1b), as implemented by Cannelli et al. (2016) and Galli et al. (2019). Radon entered the detector by diffusion through an inlet filter that traps radon daughters; Rn measurements were performed by counting the decay signals with an acquisition time of 1 second. The radon detector was connected to the pressure-vessel built on SHIVA apparatus using polyethylene tubes, which were fitted with cotton filters at the inlet and outlet valves to prevent particle and dust infiltration. A diaphragm pump with a flow rate of 380 ml/min facilitated air circulation within the closed system, between the inlet valve of the vessel and the outlet flange of the radon detector ensuring the sensible air volume less than 10 ml. This configuration allows air circulation within the vessel and from the vessel to the Rn detector in a closed system. Rn is measured in counts/s to preserve the full characteristics of the time series. Variations in radon counts occurring during the six experiments were evaluated with respect to an initial condition set at the achievement of the secular equilibrium between ^{222}Rn and its short-lived progeny which is typically achieved after 3 hours. In this pre-experiment phase, the rock samples were pre-stressed under 2 MPa for 36 hours (see Appendix 2, Fig. A1, radon counts in the pre-experiment phase). The left panel shows the real configuration of the experimental setup with a) the pressure-vessel and the b) radon detector, in a closed system, built on SHIVA apparatus made of the rotary and stationary axis.

5.2.4. Change-point analysis

A Bayesian Change-Point (BCP) analysis was performed to quantitatively detect any anomalous variation in the radon time series. The BCP approach was initially developed for studying the Earth's climate system (Ruggieri, 2013). A change-point in a time series refers to a moment when a specific statistical property of the signal varies abruptly. Algorithms designed for change-point detection work by minimising specific functions of the original time series subsets, typically involving their mean

and deviation. The fundamental operation of a Bayesian Change Point (BCP) algorithm can be summarised as follows:

1. The original time series is divided in two subsections;
2. An estimate of the desired statistical property for each subsection is computed;
3. For each sampling time of the timeseries the deviation of the actual statistical property from its empirical estimate is evaluated and cumulated;
4. The cumulated deviation is minimised by varying the division point (i.e., time instant) between the two subsections; the minimising point is the change point.

When the desired statistical property is the raw mean, the procedure can be visualised in a straightforward manner. Given a time series r_1, r_2,… r_m, r_n, being m the division time instant we can write mean (Eq. 1) and variance (Eq. 2) of the subsets as follow:

Eq. 1

$$mean\ (r_m, \dots r_n) = \frac{1}{n-m+1}\sum_{t=m}^{n} r_t$$

Eq. 2

$$var\ (r_m, \dots r_n) = \frac{1}{n-m+1}\sum_{t=m}^{n} (r_t\ -\ \mathrm{mean}(r_m, \dots r_n))^2$$

the change point is the point k corresponding to r_k minimizing the total residual deviation D (Eq. 3):

Eq. 3

$$D = (k-1)var\ (r_1, \dots r_{k-1}) + (n-k+1)var\ (r_k, \dots r_n)$$

The schematic procedure outlined above can be generalised (and rather complexified) to incorporate statistical properties other than the raw mean and include the possibility of more than one change point. In fact, when more than one change point is allowed, a simple iteration of the above procedure invariably leads to data overfitting and a so-called penalising procedure must be introduced (refer to Lavielle, 2005 and Killick et al., 2012 for technical details). Indeed, BCP algorithms have become a standard statistical investigation tool and several major time series analysis and signal processing software incorporate them granting also easy reproducibility and cross-validation of results.

For the present analysis we have used the MATLAB Version R2020b. MATLAB incorporates four versions of the algorithm characterised by different desired statistical properties to minimise in finding the change point as outlined above. The four versions are named mean, std, lin, rms (function "findchangepts", please refer to MATLAB documentation for the technical details of each version). We adopted all four versions of the algorithms in our calculations. To begin with, our raw radon time

series was subjected to a low-pass filter using a running average at six different intervals of 1, 5, 10, 15, 30 and 60 min (see the six different sampling rates in Appendix 2, Fig. A2, example from the experiment s1895). In the context of this study, the raw data (1 min moving average) has been presented with the specific aim of minimising errors associated with individual measurements. The performed analysis pertains to signal processing and time series analysis, focussing on the investigation of time series and signal processing. In such cases, the signal of interest is often obscured by noise, which can be comparable to or even greater in magnitude than the signal itself. The algorithms employed in this framework are specifically designed to operate effectively in such noisy conditions. In this context, the statistical Poissonian counting error is merely one of several potential sources of noise. The MATLAB BCP algorithm identifies an arbitrary number of change points in the radon time series, with the maximum number of change points being an input parameter of the algorithm. For our study, kmax was set to 3. In the main text, only one of the four tested algorithms are reported for each lithology (e.g. the one that exhibits two change points located closely in time). However, it is important to note that all four algorithms performed similarly with minor differences (refer to Appendix 2, Figs. A3-A8, for complete data).

Finally, we compared the results of the BCP analysis with the recorded mechanical data (Piersanti et al., 2016) to verify the correlation between radon variations detected by the change point analysis and transient variations observed in the mechanical data.

5.3. Results

5.3.1. Petrographic analysis

We conducted petrographic analysis of the non-deformed (pre-experiment) lithology of paragneiss (Fig. 2 a, b), granite (Fig. 3 a, b) and orthogneiss (Fig. 4 a, b).

5.3.1.1. Paragneiss

Samples s1896 and s1904 (Fig. 2 a, b) belong to the Austroalpine basement outcropping to the south of the DAV line near the municipality of Falzes. Schultz (1997) and Mazzoli et al., (2002) estimated a Variscan metamorphism of 0.7–0.8 GPa and 630°C in this area. The samples are fine- to medium-grained, light-brown to grey paragneiss, characterised by a mineral assemblage consisting of biotite (Bt), muscovite (Ms), chlorite (Chl), garnet (Grt), plagioclase (Pl) and quartz (Qtz) (mineral abbreviations after Warr, 2021). They exhibit a schistose, porphyroblastic, and layered structure. Schistosity is planar to gently undulated and is defined by the orientation of the sheet silicates. The

porphyroblastic structure is related to the presence of Grt and Pl porphyroblasts. The layering is determined by millimetric sheet silicates-rich bands (Ms, Bt, Chl) alternating with granoblast-rich layers mainly composed of Qtz and Pl. The grain size of sheet silicates in mica-rich bands is mainly around 0.5-1 mm whereas the dimensions of Qtz and Pl grains generally fall in the range 0.5-1 mm. Plagioclase may form 3-4 mm porphyroblasts. Millimetric pseudomorphic aggregates of sericite and subordinate chlorite after staurolite are also present. Accessory phases such as tourmaline, apatite, opaque minerals, zircon, and epidote are also present.

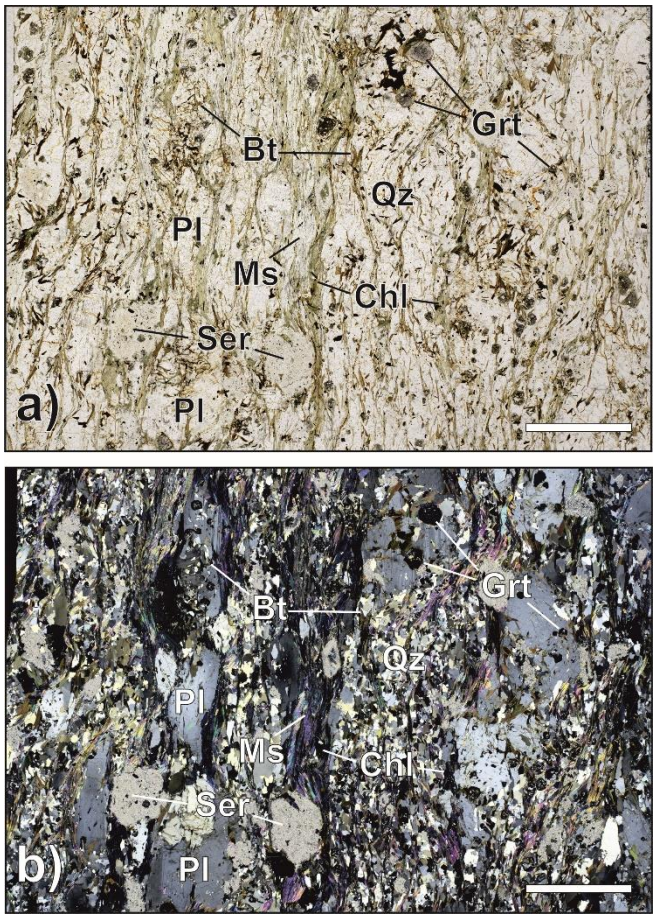

Figure 2. (**a**, **b**) Paragneiss. Plane- (**a**) and cross-polarised light (**b**) photomicrographs of paragneiss. Schistosity is planar to gently undulated and it is defined by the orientation of the sheet silicates (nearly vertical in the picture). The layering is determined by muscovite (Ms)-, biotite (Bt)-, sericite (Ser)-, chlorite (Chl)-rich bands alternating with granoblast-rich layers mainly composed of quartz (Qz) and plagioclase (Pl). Scale bar for references measures 500 μm. Mineral abbreviations after Warr (2021).

5.3.1.2. Granite

Samples s1895 and s1897 (Fig. 3 a, b) are representative of the Southalpine Permian granite (Del Moro and Visonà, 1982) near the Periadriatic Lineament in the municipality of Mules. The granite has a heterogranular seriate isotropic structure and is characterised by a mineral assemblage consisting of potassium feldspar (Kfs), plagioclase (Pl), quartz (Qtz), and biotite (Bt) (mineral abbreviations after Warr, 2021). The Kfs and Pl crystals are subhedral and euhedral, respectively.

The grain size distribution of quartz, plagioclase and K-feldspar ranges mainly between 0.2- and 5-mm. Hydrothermal activity has strongly altered the primary mineral phases, such that Bt has been extensively replaced by chlorite (Chl), Pl by a mesh of muscovite, epidote, and calcite, and Kfs has been altered to varying degrees into kaolinite. Accessory phases such as epidote, apatite, zircon, and opaque minerals are also present.

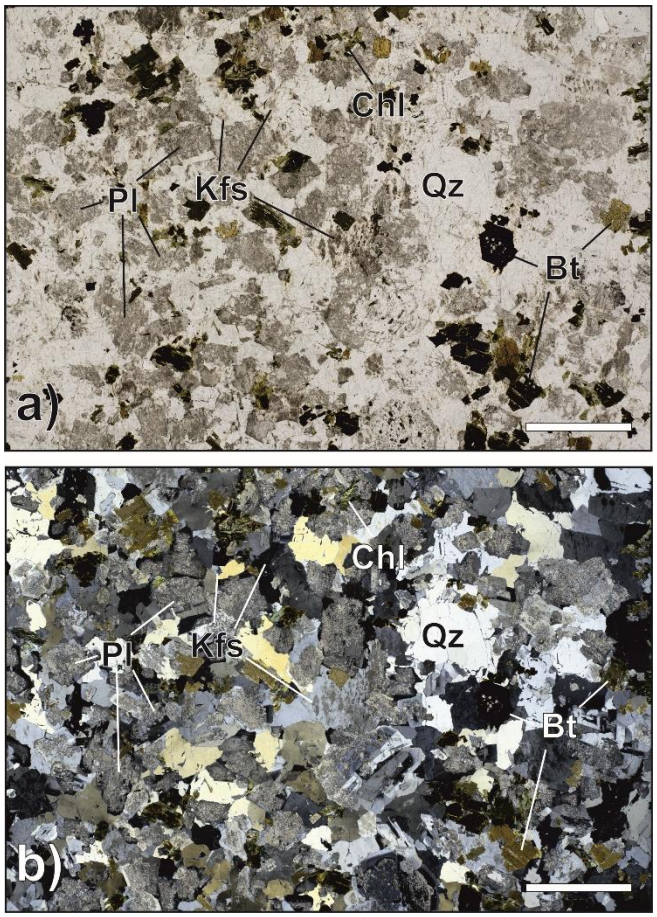

Figure 3. (**a**, **b**) Granite. Plane- (**a**) and cross-polarised light (**b**) photomicrographs of granite. The granite has a heterogranular isotropic structure and is characterised by a mineral assemblage consisting of potassium feldspar (Kf), plagioclase (Pl), quartz (Qtz), and biotite (Bt). Hydrothermal activity has strongly altered the primary mineral phases, such that Bt has been extensively replaced by chlorite (Chl), Pl by a mesh of muscovite, epidote, and calcite (greyish coloured dusty pattern in Fig. 2a). Scale bar for references measures 500 µm. Mineral abbreviations after Warr (2021).

5.3.1.3. Orthogneiss

Samples s1916 and s1917 (Fig. 4 a, b) are representative of the Austroalpine basement. Granitic orthogneisses are light-grey rocks that resemble granite, composed of minerals such as potassium-feldspar (Kfs), quartz (Qtz), plagioclase (Pl), chlorite (Chl), muscovite (Ms), and biotite (Bt) (mineral abbreviations after Warr, 2021). These rocks formed through regional metamorphism of a granitic body in the late Ordovician period (Klötzli, 1995). The degree of foliation in these rocks can range from barely perceptible to gneissic, and it is determined by the orientation of large porphyroclasts of Kfs (up to 7 mm), discontinuous bands of sericitized plagioclase crystals, and phyllosilicates (mainly

Chl and Ms). Biotite in these rocks has undergone significant alteration into Chl. Additionally, decussate Ms flakes (0.1 mm) often crystallise on chloritized biotite layers. The grain size of these rocks varies, with Kfs and Qtz exhibiting coarse grains (7 mm) and Pl exhibiting medium grains (1 mm). Very small, rare garnet grains can also be found within Pl crystals. Accessory minerals such as apatite, epidote, zircon, opaque minerals are also present in these rocks.

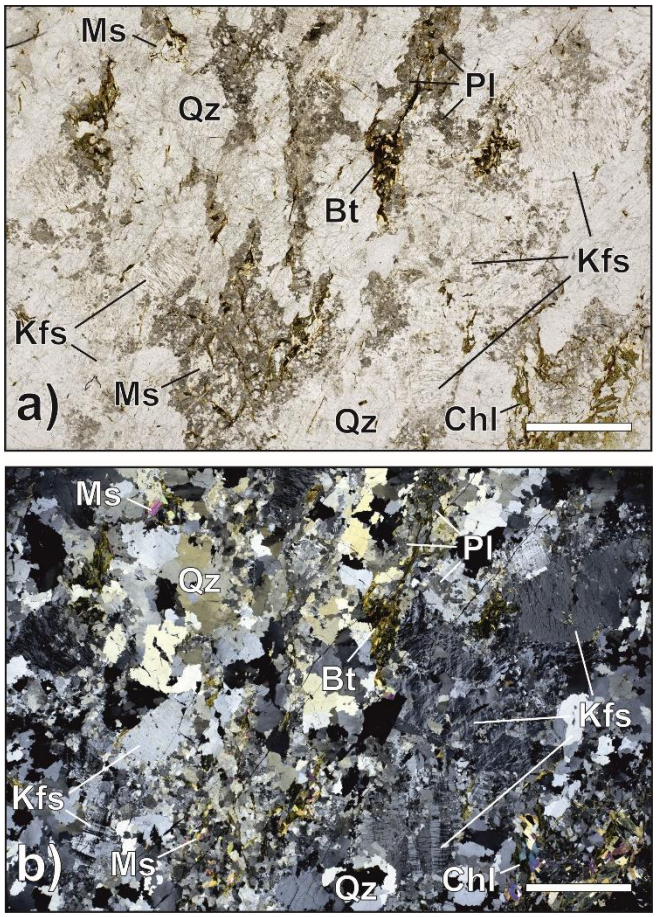

Figure 4. (**a, b**) Orthogneiss. Plane- (**a**) and cross-polarised light (**b**) photomicrographs of orthogneiss. Gneissic structure is determined by the orientation of large porphyroclasts of Kf (up to 7 mm), discontinuous bands of sericitized plagioclase crystals (greyish coloured dusty pattern in Fig. 5a), and phyllosilicates (mainly Chl and Ms). Biotite in these rocks has undergone significant alteration into Chl. Scale bar for references measures 500 μm. Mineral abbreviations after Warr (2021).

5.3.2. Shear stress-controlled experiments

We conducted six shear stress-controlled tests (two tests per lithology). During the experiment the shear stress was increased stepwise (black solid line in Figs. 5, 6 and 7), while the slip (red solid line) and the slip-velocity adjusted spontaneously. Each stepping caused variations in the axial shortening (blue solid line) and normal stress (light grey solid line). The Rn counts recorded in continuous during the stepping stage are shown on bottom panels of Figs. 5, 6 and 7 in grey colour for the paragneiss (s1896), granite (s1897) and orthogneiss (s1917) respectively.

5.3.2.1. Paragneiss

In the case of experiment s1896 (Fig. 5) Rn counts exhibit a constant trend throughout the experiment with a decrease near the main instability which occurred at a shear stress of 3 MPa (friction coefficient = 0.6). For this experiment we present the change-point analysis performed on the Rn time series using the "std" algorithm, which identified two overlaid change points (i.e. 15 s apart). Remarkably, the two change points were detected close to the main instability. The main instability was anticipated by a slight increase and accompanied by a sharp decrease in Rn counts although by visual inspection a possible link with the mechanical data was unclear. This link was rather established using the change point analyses which identified two points marking region of nearly stable behaviour of all the measured variables nearly 11:07 min before all of them started to transiently change: normal stress decreased of 0.2 MPa, slip accelerated towards the main instability and axial shortening reported a significant change in the compaction rate (nearly 0.01 mm/min) before the sharp increase recorded during the main instability.

Experiment s1904 (see Appendix 2, Fig. A9) also exhibited a nearly constant trend in Rn counts throughout the experiments with a sharp decrease in Rn counts close to the main instability which occurred at a shear stress of 3.3 MPa (friction coefficient = 0.6). For this experiment we present the change-point analysis performed on the Rn time series using the "lin" algorithm, which identified three change points. The first two change points were located close to an increase in Rn counts compared to the average Rn trend. In correspondence to these two change points, the mechanical data showed a progressive increase in the normal stress and axial shortening with no significant changes in either shear stress or slip. The third detected change point instead identified a sharp decrease in Rn counts about 3 min after the main instability. The significance of this third point though shall be analysed considering that the occurrence of the main instability in this experiment was forced by a sign error in the manual control of the shear stress which resulted in a clockwise rotation of the column. Conversely to all the other experiments, the main instability did not occur spontaneously. Despite this technical issue, again the Rn decrease at change point location also corresponded to a sharp increase in slip and compaction of the rock samples.

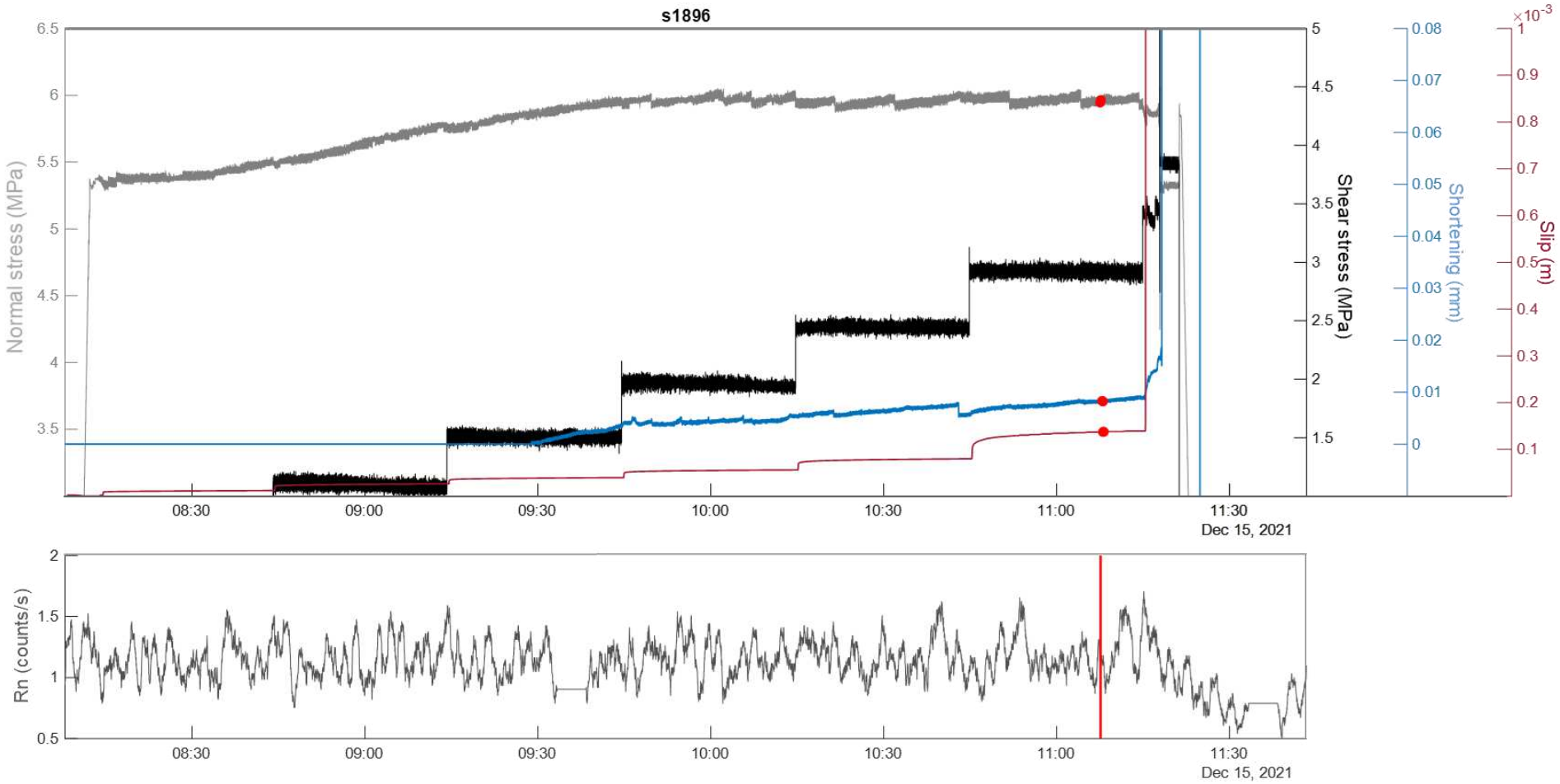

Figure 5. Experiment s1896, paragneiss. Top panel: Normal stress (MPa, dark grey solid line), shear stress (MPa, black solid), slip (m, red solid), and axial shortening (mm, blue solid); change points (algorithm "std", red circle). Bottom panel: radon, count/s moving average over 1 min, red lines change points (algorithm "std").

5.3.2.2. Granite

Experiment s1897 (Fig. 6) shows a constant trend in Rn counts throughout the duration of the experiment and a slight increase in Rn count close to the occurrence of the main instability at a shear stress of 3.4 MPa (friction coefficient = 0.7). For this experiment we present the change-point analysis performed on the Rn time series using the "lin" algorithm, which identified three change points. All three change points were located near the rock instability, close to the first increase in Rn counts. Specifically, the three change points marked three stages of the last shear stress step (during the stepping up and before the main instability event) where the normal stress decreased of 0.2 MPa and slip increased up to 0.3 m. Axial shortening gradually increased throughout the experiment suggesting constant compaction up to 0.06 mm at the end of the experiment.

Experiment s1895 in granite (see Appendix 2, Fig. A10) shows a constant trend in Rn counts during the first two hours of the experiment (8.30 to 11:00 a.m.) and a gradual increase throughout the duration of the experiment until the onset of the main instability which occurred at shear stress of 4 MPa (friction coefficient = 0.8), slightly higher than the granite sample s1897. After the instability, Rn counts returned to a constant trend. For this experiment we show the change-point analysis performed in the Rn time series using the "mean" algorithm, which identified three change points. The first change point was located near the first increase in Rn counts trend, coeval to a gradual increase in the axial shortening due to a gradual compaction of the samples. The last two change points were located a few minutes apart in correspondence to another gradual increase in Rn counts (maximum value 3.6 counts/s) about 25 min before from the main instability occurring at time 12:12 which caused a fast and self-arresting event (slipping at nearly 0.2 m/s). The trend shown in the mechanical data is consistent with the detected change points, as they correspond to a sharp increase in slip and increase in the shortening (up to 0.06 mm). This experiment was manually stopped after the occurrence of this small instability which resulted in a thin layer of pseudotachyliytes visible over the contact surface of the recovered samples suggesting that the experiment experienced a large temperature increase. The manual stop was forced by an overheating error of the control system.

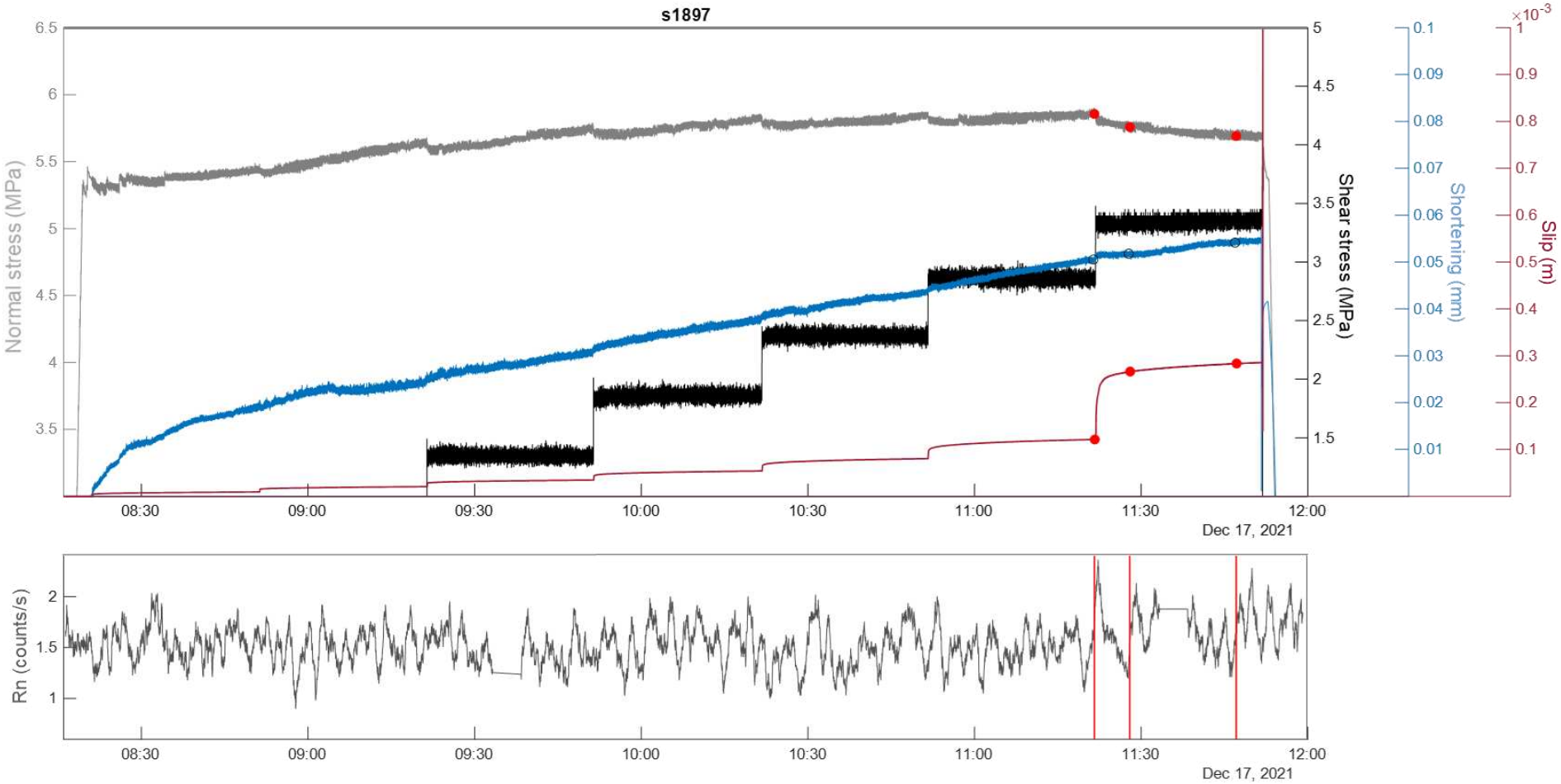

Figure 6. Experiment s1897, granite. Top panel: Normal stress (MPa, dark solid line), shear stress (MPa, black solid), slip (m, red solid), and axial shortening (mm, blue); change points (algorithm "mean", red circles). Bottom panel: radon, count/s moving average over 1 min, red lines change points (algorithm "mean").

5.3.2.3. Orthogneiss

In the case of experiment s1917 (Fig. 7) Rn counts exhibited a constant trend throughout the experiment; the main instability occurred at a shear stress of 4.3 MPa (friction coefficient = 0.8). For this experiment we present the change-point analysis performed in the Rn time series using the "std" algorithm, which identified two overlaid change points (i.e., 9 s apart). These two change points were located at the last stage of the stepping in shear stress, before the main instability and after the occurrence of a short but fast unstable event (time c.a. 20:14) running at 0.14 m/s (see Appendix 2, Fig. A11). An initial dilation was recorded right before the occurrence of this fast event which was followed by a sharp increase in axial shortening (= compaction). Although no particular trends are visible in the Rn series, the change points highlighted clear variations in the mechanical data.

In case of experiment s1916 (see Appendix 2, Fig. A12), Rn counts exhibit a constant trend throughout the experiment, except for a sharp increase after the rock instability occurring at a shear stress of 3.5 MPa (friction coefficient = 0.7).

For this experiment we present the change-point analysis performed in the Rn time series using the "mean" algorithm, which detected two change points. It is worth noting that this experiment is the only one in which the first identified change point was located at the beginning of the experiment. This change point marked a slight increase in Rn counts, which is related to the initial rise in normal stress and shortening can be observed, linked to the first sample compaction. The second change point was located about 2 min after an unstable event running at slip velocity of 0.1 m/s. This event was preceded by a short dilation (time 20:30) before the sample started compacting and normal stress slightly decreased. At the end of this event and until the end of the experiment we detected a slight increase in Rn counts.

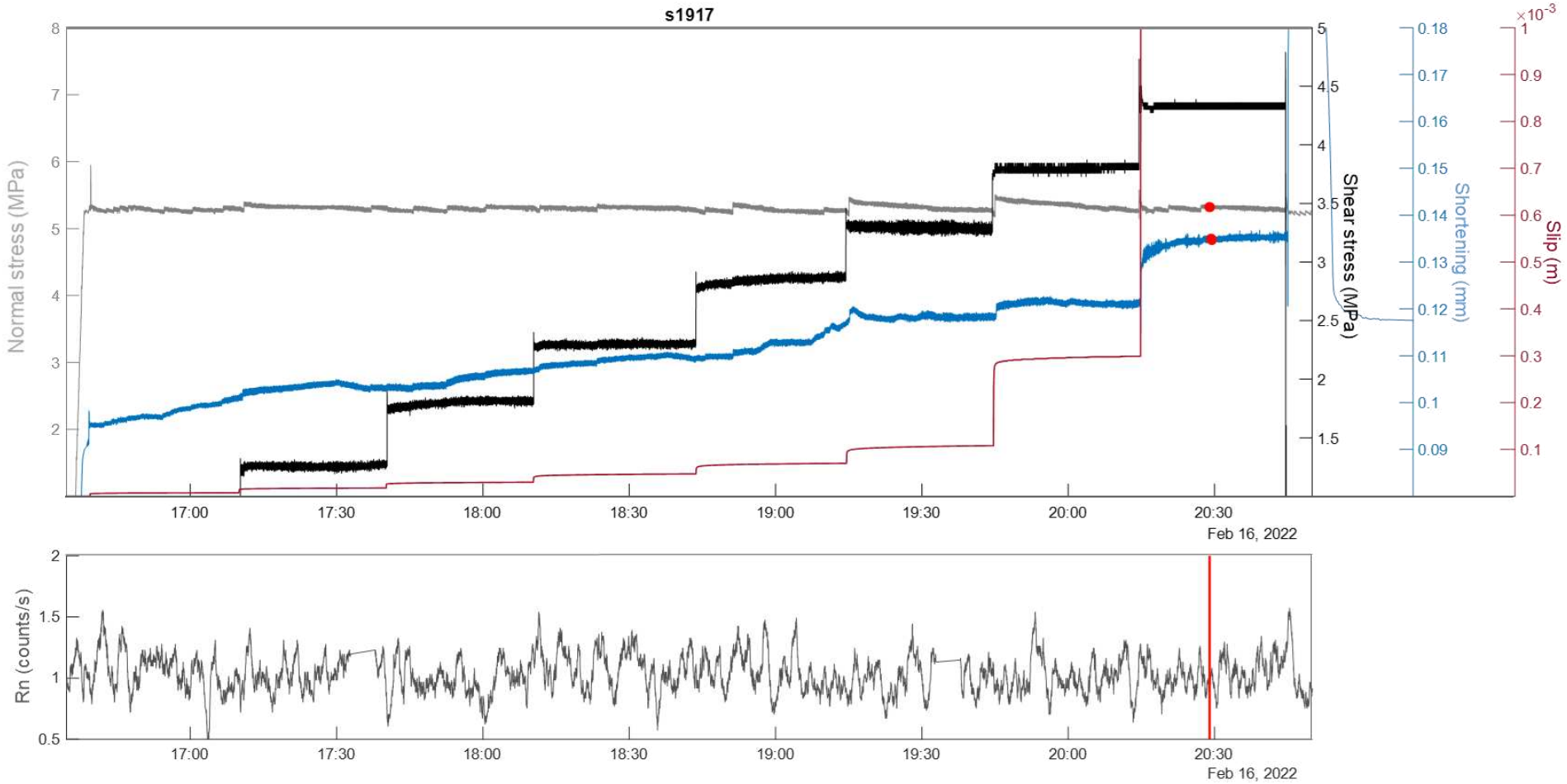

Figure 7. Experiment s1917, orthogneiss. Top panel: Normal stress (MPa, dark solid line), black shear stress (MPa, black solid), slip (m, red solid), and axial shortening (mm, blue solid); change points (algorithm "mean", red circles). Bottom panel: radon, count/s moving average over 1 min, red lines change points (algorithm "mean").

5.4. Discussion

The experiments conducted on three different lithologies revealed two important features: (*i*) the three lithologies exhibited distinct trends in radon emissions and (*ii*) the change-point analysis performed on the Rn time series effectively marked significant stages of the experiment and confirmed a causal variation between radon variations and transient stages of the mechanical data. The strength of this statistical approach lies in the remarkable consistency of results obtained from all the algorithms used. These algorithms not only identified the most significant variations in radon counts, but also highlighted specific mechanical features as all the change points coincided with relevant variations in mechanical behaviour. Notably, the results obtained from all the adopted algorithms consistently indicated a strong correlation with the mechanical data. Additionally, due to the nature of this technique, it is necessary to set a maximum number of allowed change points. In this study, the maximum number of points was not always assigned, and when assigned, they often appear at the same point (e.g. experiments s1896 and s1917). This serves as a strong indication of the high significance of the performed statistical analysis.

The two paragneisses (i.e. s1896, s1904) exhibited a fairly constant radon trend throughout the experiment, with slight decrease at the onset of the main instability event. The observed radon trend in paragneiss can be attributed to the specific mineralogy and microstructure of this rock. Paragneiss is a relatively soft rock due to the presence of millimetric iso-oriented layers made mostly of sheet silicates (45% of the volume). Under the applied stress, these sheet silicates flake are further oriented and compacted, forming an almost impermeable barrier preventing radon exhalation from the sample surface. This phenomenon may explain the decrease in radon counts close to and during the main instability. The change-point analysis highlighted that variations in radon counts are consistent with the mechanical data, where the two overlaid change points in the case of e.g. experiment s1896, were detected at the beginning of radon decrease close to the main instability.

On the other hand, granite behaves differently. Both experiments s1895 and s1897, although run at slightly different stress conditions due to a technical challenge, showed a gradual increase in radon counts, reaching the maximum values close to and during the main instability. This slight increase in Rn counts corresponded to a gradual increase in axial shortening throughout the experiment. The change-point analysis confirmed that radon variations are reflected in the mechanical data, where three change points were detected in both granites at the beginning of radon increase and before the main instability. The mineralogical and microstructural features of the granite produce a different radon trend compared to paragneiss. Granite is a magmatic rock mainly composed of granular minerals such as quartz and feldspars, with only small amounts of sheet silicates (8% of the volume),

this makes this lithology hard and compact. Under the load application (both normal and shear stress), granular minerals such as quartz and feldspars are fractured, gradually decreasing their average grain size and increasing the microscopic porosity, increasing the sample gas permeability (Payton et al., 2022). Therefore, it is likely that during gradual sample fracturing, a greater fraction of radon escapes from the sample surface.

In the case of the two samples of orthogneiss (i.e. s1916, s1917) we documented a slight increase in radon counts after the main instability in the first experiment, but no significant trend is visible in the second experiment. Both experiments evidenced the onset of a short but fast (c.a. 0.1 m/s of slip velocity) event before the main instability, anticipated by a short phase of dilatancy. The change-point analyses marked the occurrence of these events in the respective radon time series. Orthogneiss displayed a behaviour that is midway between granite and paragneiss in terms of microstructure. The granoblastic layers made up of granular quartz and feldspars show a decreasing grain size due to increasing fracturing, leading to an increase in microscopic porosity (Payton et al., 2022) and conferring a higher gas permeability similar to granite. However, at the same time, the lepidoblastic bands made up of sheet silicates (15% of the volume) are compacted, forming an almost impermeable barrier preventing radon exhalation from the fracture, similar to paragneiss. Therefore, during the load application (both normal and shear stress) in orthogneiss, the increased Rn counts likely derived from the increased porosity of granular layers (probably leading to dilatant stages) is compensated by a decreased Rn emission due to sheet silicate flakes compaction in lepidoblastic bands, sealing the porosity and preventing gas flow through the rock. This mixed structure made of granular materials and clays exhibited alternating dilatant/compacting behaviour as documented by the recording of the axial shortening which is also significantly different from either granite or paragneiss. In these experiments, our aim was to control and isolate only few of the many phenomena that can occur at the natural scale and lead to radon variations at the surface.

In nature, various factors, including the presence of carrier fluids, can affect the emission, concentration and migration of radon. Additionally, faulting and other geological processes can increase radon emission, but this behaviour is not always consistent: in some cases, a decrease or insignificant variation in the radon trend can also occur. Therefore, it is crucial to carefully analyse the specific petrographical and microstructural features at a micro-scale, as well as the geological and structural conditions of the area at a macro-scale to understand Rn behaviour in a complex tectonic setting. Although external fluid dynamics are absent in these experiments, the shear stress control procedure still represents the gradual increase in the tectonic loading which can be observed in nature during the earthquake cycle.

The radon counts observed in these experiments can be considered representative of the mechanical behaviour of faults in the represented lithologies, within a very simplified, closed and controlled environment. The duration of laboratory experiments greatly compresses the timescales of the real seismic cycle, and the temporal resolution of events is proportionally reduced. Nevertheless, in several cases, we have evidence of significant radon changes (i.e., detectable by Change Point Analysis) before the onset of mechanical instabilities.

5.5. Conclusions

The shear stress-controlled experiments, carried out on the three different lithologies (paragneiss, granite, orthogneiss) highlight a significant phenomenon involving a direct and almost instantaneous correlation between rock deformation and radon variation, which is also dependent on lithology. By enhancing temporal resolution of the experiments (close to real-time measurements) clear trends and transient variations in radon emissions by the rock samples can be identified and correlated with specific and transient features in the mechanical data. Rn emission varies according to rock deformation and is highly dependent on lithology, mineralogy and microstructure. This behaviour is evident in all the three considered lithologies, paragneiss displays a sharp decrease in radon counts during the main instability, granite shows a gradual increase in radon counts throughout the experiment and orthogneiss exhibits a behaviour intermediate between granite and paragneiss, in terms of microstructure, with no significant increase or decrease in radon counts. Robust statistical tool (i.e. change point analysis) is able to identify frictional instabilities from independent Rn measurements, highlighting a clear correlation between Rn emission and the mechanical behaviour of rocks. This relation is measurable in a short time frame (minutes) and it is lithology dependent (e.g. not all rocks are expected to create easy pathways for radon emission during frictional instabilities). These observations are reliable in a simplified, closed and controlled environment but, starting with the micro-scale, help to establish limitations on the utilisation of radon gas as an indicator for transient and rapid rock deformation in complex natural scale phenomena.

References

Benà, E., Ciotoli, G., Ruggiero, L., Coletti, C., Bossew, P., Massironi, M., Mazzoli, C., Mair, V., Morelli, C., Galgaro, A., Morozzi, P., Tositti, L., Sassi, R. Evaluation of tectonically enhanced radon in fault zones by quantification of the radon activity index. Sci Rep 12, 21586 (2022). https://doi.org/10.1038/s41598-022-26124-y.

Cannelli, V., Piersanti, A., Spagnuolo, E. Galli, G. Preliminary analysis of radon time series before the MI=6 Amatrice earthquake: possible implications for fluid migration. Annals of Geophysics, 59, fast track 5 (2016). doi:10.4401/ag-7166

Cornelio, C., Spagnuolo, E., Di Toro, G. et al. Mechanical behaviour of fluid-lubricated faults. Nature Communications 10, 1274 (2019). https://doi.org/10.1038/s41467-019-09293-9

Del Moro A, Visonà D. The epiplutonic Hercynian Complex of Bressanone-Brixen, Eastern Alps, Italy. Petrological and radiometric data. Neu. Jb. Mineral. Abh., 145, 66-85. (1982).

Di Toro, G., Niemeijer, A., Tripoli, A., Nielsen, S., Di Felice, F., Scarlato, P., Spada, G., Alessandroni, R., Romeo, G., Di Stefano, G., Smith, S., Spagnuolo, E., Mariano, S. From field geology to earthquake simulation: a new state-of-the-art tool to investigate rock friction during the seismic cycle (SHIVA). Rend. Fis. Acc. Lincei, 21 (Suppl 1): S95-S114 (2010). doi 10.1007/s12210-010-0097-x.

Galli, G., Cannelli, V., Nardi, A., Piersanti, A. Implementing soil radon detectors for long term continuous monitoring. Applied Radiation and Isotopes, 153, 108813 (2019). https://doi.org/10.1016/j.apradiso.2019.108813

Jordan, T.H., et al. Operational earthquake forecasting: state of knowledge and guidelines for utilisation. Ann. Geophys. - Italy, 54, 319-391 (2011).

Klötzli U. Geochronologische Untersuchungen an Metagranitoiden im ostalpinen Altkristallin W und S des Tauernfensters. Arbeitstagung der Geologischen Bundesanstalt. Lienz, 95-97 (1995).

Koike, K., Yoshinaga, T. & Asaue, H. Radon concentrations in soil gas, considering radioactive equilibrium conditions with application to estimating fault-zone geometry. Environ. Geol., 56, 1533-1549 (2009)

Koike, K., Yoshinaga, T., Suetsugu, K., Kashiwaya, K., Asaue, H. Controls on radon emission from granite as evidence by compression testing to failure. Geophys. J. Int, 203, 428-436 (2015). doi: 10.1093/gji/ggv290

Koike, K., Yoshinaga, T., Ueyama, T. & Asaue, H. Increased radon- 222 in soil gas because of cumulative seismicity at active faults. Earth Planet Space, 66 (57), 1-9 (2014b).

Lavielle, Marc. Using penalized contrasts for the change-point problem. Signal Processing, 85, 1501-1510 (2005).

Mazzoli, Sassi R., Burlini L. Experimental study of the seismic properties of Eastern Alps (Italy) along the Aurina - Tures - Badia Valleys transet. Tectonophysics, 374, 179-194, Amsterdam (2002). ISSN: 0040-1951.

Mollo, S., Tuccimei, P., Heap, M.J., Vinciguerra, S., Soligo, M., Castelluccio, M., Scarlato, P. & Dingwell, D.B. Increase in radon emission due to rock failure: an experimental study. Geophys. Res. Lett., 38, L14304, (2011) doi:10.1029/2011GL047962.

Neilsen S., Spagnuolo E., Violay Marie. Composite SAmple MOunt Assembly (SAMOA): The Ultimate Sample Preparation for Rotary Shear Experiments. Rapporti Tecnici INGV, Vol. 215 (2010).

Nicolas, A., Girault, F., Schubnel, A., Pili, ´ E., Passelegue, F., Fortin, J. & Deldicque, D. Radon emanation from brittle fracturing in granites under upper crustal conditions. Geophys. Res. Lett., 41, 5436–5443 (2014).

Payton R. L., Chiarella D., Kingdon A. (2022) The influence of grain shape and size on the relationship between porosity and permeability in sandstone: a digital approach. Sci Rep, 12, 7531. https://doi.org/10.1038/s41598-022-11365-8

Piersanti, A., Cannelli, V., Galli, G. The Pollino 2012 seismic sequence: clues from continuous radon monitoring. Solid Earth, 7, 1303–1316 (2016). doi:10.5194/se-7-1303-2016.

R. Killick, P. Fearnhead & I. A. Eckley. Optimal Detection of Changepoints With a Linear Computational Cost, Journal of the American Statistical Association, 107:500, 1590-1598, (2012). DOI: 10.1080/01621459.2012.737745.

Ruggieri, E.: A Bayesian Approach to Detecting Change Points in Climatic Records. Int. J. Climatol., 33, 520–528 (2013)

Scarlato, P., Tuccimei, P., Mollo, S., Soligo, M., and Castelluccio, M. Contrasting radon background levels in volcanic settings: Clues from 220Rn activity concentrations measured during long-term deformation experiments, Bull. Volcanol., 75, 751 (2013). doi:10.1007/s00445-013-0751-0, 2013.

Schultz, B., 1997. Pre-Alpine tectonometamorphic evolution in the Austroalpine basement to the south of the central Tauern Window. Schweiz. Mineral. Petrogr. Mitt. 77, 281-297.

The MathWorks, Inc. Signal Processing Toolbox version: 8.5 (R2020b). Accessed: September 06, 2023. Available: https://www.mathworks.com

Tuccimei, P., Mollo, S., Scarlato, P., Castelluccio, M. Real-time setup to measure radon emission during rock deformation: implication for geochemical surveillance. Geosci. Intrum. Method. Data Syst., 4, 111-119 (2015).

Tuccimei, P., Mollo, S., Vinciguerra, S., Castelluccio, M., Soligo, M. Radon and thoron emission from lithophysae-rich tuff under increasing deformation: an experimental study. Geophys. Res. Lett., 37, L05305 (2010). doi:10.1029/2009GL042134.

Violay, M., Nielsen, S., Spagnuolo, E., Cinti, D., Di Toro, G., Di Stefano, G. Pore fluid in experimental calcite-bearing faults: abrupt weakening and geochemical signature of co-seismic processes. Earth and Planetary Science Letters, 361, 74-84 (2013). http://dx.doi.org/10.1016/j.epsl.2012.11.021

Wakita, H. Geochemical challenge to earthquake prediction. Proc. Natl. Acad. Sci. U.S.A., 93, 3781-3786 (1996)

Wang, X., Li, Y., Du, J., Zhou, X. Correlations between radon in soil gas and the activity of seismogenic faults in the Tangshan area, North China. Radiat. Meas., 60, 8-14 (2014)

Warr L.N. IMA–CNMNC approved mineral symbols. Mineralogical Magazine, 85, 291-320 (2021).

6. CONCLUSIONS

The main goal of this thesis was to investigate the tectonic control on enhancing the geogenic radon potential at surface, analysing the potential degassing process in aseismic fault zones as fundamental factor in radon hazard and risk assessment.
This aim has been addressed working at a double scale of investigation: macro-scale and micro-scale (laboratory-scale).
This work fulfilled the goals originally presented in the research project and summarised by the three main questions debated in the literature.

Chapter 1. What is the potential degassing process along the non-seismic Pusteria fault system and its role in increasing the GRP at surface?

The first chapter was focused on the evaluation at the macro-scale of the potential degassing processes along the investigated aseismic Pusteria fault system in the study area. To accomplish this objective, I have defined the geogenic radon component called Tectonically Enhanced Radon (TER) representing the additional contribution of tectonics to the Geogenic Radon Potential (GRP) over an area. Then, the TER has been quantified by calculating the Radon Activity Index (RAI) that defines the geochemical activity of a fault in terms of Rn emission.
The obtained results highlight that the fracture zone of the Pusteria fault system has a fundamental role for gas (^{222}Rn and CO_2) migration towards the surface thus providing TER as an additional contribution to the Rn diffusing from the source rocks increasing the GRP at surface. The TER component is the main degassing process along the investigated fault system.
Furthermore, the areas characterised by high radon values are associated with high fault density and these zones represents the TER zones. It is also possible to assume that the RAI calculated at each Rn peak values along N-S profiles represents a good proxy to quantify the geochemical activity of a fault zone.
In the study area, the TER areas are characterised by medium to very high RAI values. However, although the central sector of the Pusteria fault system shows a high fault density, the associated low RAI values suggest the presence of less permeable segments along the fault system. The comparison between the calculated RAI for the study area and those calculated from seismic areas with seismic faults from the literature, highlights that also aseismic faults can provide channels for Rn migration towards the Earth's surface with the same order of magnitude of seismic faults.
Considering the radon migration from the deep source rocks towards the surface, it is clear that the quantification and mapping of the TER areas are important to better evaluate the potential risk for the

inhabitants due to the increased radon availability to enter buildings. Mapping TER zones is of practical interest for local authorities in the definition of radon hazard (GRP) in urban areas (implications on Rn risk).

Chapter 2. What is the effectiveness of mapping the geological hazard to define the collective radon risk exposure?

The second chapter was aimed on understanding the effectiveness of mapping the geological hazard (GRP) to define the collective radon risk areas (CRAs) according to a new, more geological interpretation of RPAs, as compared to that outlined in the BSS directive (2013/59/EURATOM).

I used the simple risk formula to combine the GRP map, obtained applying a robust multivariate Machine Learning technique, involving the land use as location type (the vulnerability factor) and population density (the exposure factor).

In line with a geological-based interpretation of RPAs, we can recognise hazard-based RPAs (CRAs) and detriment-based RPAs (IRAs) as complementary concepts within territorial planning and remediation actions, respectively, rather than alternatives.

The obtained results show that the use of the random forest algorithm as a ML model proved to be robust and highly effective for generating a GRP map of the study area. This GRP map incorporated seven predictors, reflecting geological factors (lithological background and TER), soil characteristics (groundwater circulation, soil permeability), and meteorological conditions (DTM derivative). The variable importance analysis highlighted the dominant impact of the Rn source, still showing significant contributions from other predictors.

Considering that the GRP is known as the most critical spatial predictor of the indoor radon concentration (IRC), it is clear that an accurate mapping of this hazard factor effectively represents the total amount of radon that could potentially influx within buildings.

Given that GRP values are three orders of magnitude higher than IRC, there is no reason to establish a specific GRP threshold. Indoor radon risk can exist even for "very low" concentrations of radon in the soil and, consequently, for very low GRP values. Qualitative GRP classes can serve as delineation of zones, similar to those used in seismic micro zonation studies, guiding land-use planning strategies, construction types, and remediation actions.

The elaboration of GRP maps is a crucial tool for both Rn hazard and risk analysis since it represents the base for identifying the RPAs under a new, more geological perspective.

This is essential for collective and individual risk assessment, including, on the one hand the land-use planning and prevention, and, on the other hand, strategic planning for indoor surveys, and specific remediation actions. The absence of clear guidelines for defining RPAs needs the geological-

based conceptualisation of a complementary approach to mapping the Collective Risk areas (for prevention) and Individual Risk Areas (for remediation). From this study, it is clear that mapping the GRP (geo-hazard) is a fundamental starting point in Rn risk assessment.

The study area, being the first time, it was investigated from a geochemical point of view, shows a great potential in degassing process not only for Rn migration but also for other gases (e.g. CO_2, H_2, CH_4).

At the macro-scale, the test area deserves deepest geological investigations adding, for instance, the gas geochemistry or isotope geochemistry to study the origin and the composition of the carrier gases. In addition, future studies aimed to reach the citizen may be focused on the definition of the effective individual risk assessment by creating models that also consider the indoor radon measurements and anthropogenic factors controlling radon accumulation in the dwellings, in order to predict the detriment for the population.

Chapter 3. What is the potential relationship between radon migration dynamics and rocks deformation?

The third chapter was aimed to understand the potential relationship between Rn emission and rocks deformation of three lithologies (paragneiss, orthogneiss and granite) samples in the study area. The shear stress-controlled experiments, carried out on the three selected lithologies, highlight a significant phenomenon involving a direct and almost instantaneous correlation between rock deformation and radon counts variation, which is dependent on lithology. Increasing the temporal resolution to a short time frame of minutes, it is possible to observe clear trends and variations in the radon counts (i.e. emission).

In order to detect unbiased variations in Rn counts we used a robust statistical tool, the change points analysis, which marked strong changes in Rn time series. These changes can be correlated with specific features in the mechanical data, even if the Rn time series and the mechanical data are completely independent datasets. Such correlation between the two independent datasets highlights a clear link between Rn emission and the rock deformation of rocks and with frictional instabilities on pre-existing faults in this case. This correlation is measurable in the short time frame of minutes and it is lithology dependent.

Therefore, Rn emission varies according to rock deformation and is highly dependent on lithology, mineralogy and microstructure as clearly shown in the case of all the three investigated lithologies. In particular, the paragneiss displays a sharp decrease in radon counts during the main instability, the granite shows a gradual increase in radon counts during the loading stage of the experiment and the orthogneiss do not displays significant increase/decrease in Rn counts. The latter observation might

be explained by orthogneiss' microstructure which encompass intermediate features between granite and paragneiss microstructures.

Results pertain a very simplified, closed and controlled environment respect to the natural scale where Rn emission and migration depends on several others variables as mentioned in the introduction. However, this study is a starting point to utilise the Rn gas as an indicator for transient and rapid rock deformation in complex natural scale phenomena.

The experiments performed in this project at the micro-scale give promising results in understanding the complex Rn migration mechanisms by isolating only the rock (and faults) deformation as dominant process.

Considering that there are many other variables influencing Rn migration along faults, this study deserves deepest investigation, on the one hand including other important variables (e.g. the presence of a carrier gas) and, on the other hand, testing Rn behaviour in other different lithologies (e.g. limestone).

Appendix 1

Table A1:

Profile	N. peak	X	Y	Rn max	RAI
P4	1	712003	5189508	57	1.14
P5	1	712513	5190538	109	2.18
	2	712513	5188437	68	1.36
P6	1	713003	5190406	243	4.86
P7	1	713502	5190416	122	2.44
P8	1	714012	5189998	193	3.86
P9	1	714512	5189987	134	2.68
P10	1	715002	5189998	90	1.80
P11	1	715502	5189559	120	2.40
	2	715502	5188580	56	1.12
P12	1	716001	5189804	68	1.36
	2	716001	5188825	79	1.58
P13	1	716491	5189814	74	1.48
P14	1	717001	5190344	54	1.08
	2	716991	5188886	74	1.48
	3	717511	5190518	91	1.82
	4	717501	5188539	65	1.30
P16	1	718001	5189712	115	2.30
P17	1	718500	5190508	69	1.38
	2	718500	5188702	110	2.20
P18	1	719000	5191619	69	1.38
	2	719000	5189579	132	2.64
P19	1	719510	5191130	693	13.86
	2	719500	5189987	125	2.50
	3	719500	5188570	288	5.76
P20	1	720000	5191925	188	3.76
	2	720010	5190069	159	3.18
	3	719990	5188886	135	2.70
	4	720010	5187907	124	2.48
P21	1	720500	5191915	119	2.38
	2	720500	5189916	392	7.84
	3	720510	5188172	174	3.48
P22	1	721010	5191762	151	3.02
	2	720999	5189926	611	12.22
P23	1	721499	5191997	112	2.24
	2	721499	5191007	499	9.98
	3	721489	5190008	308	6.16
	4	721510	5189008	159	3.18
P24	1	721999	5190997	213	4.26
	2	721999	5188865	115	2.30

Table A1. Radon Activity Index (RAI) values calculated in correspondence of radon peaks along the estimated (from P4 to P24) profiles in the study area. N. peak = number of considered peaks along the i^{th} profile; X, Y = location of the radon peaks; Rn max = maximum radon value along the i^{th} profile; RAI = Radon Activity Index calculated as the ratio between the maximum radon value and the background value (50 $kBq \cdot m^{-3}$).

Figure A1:

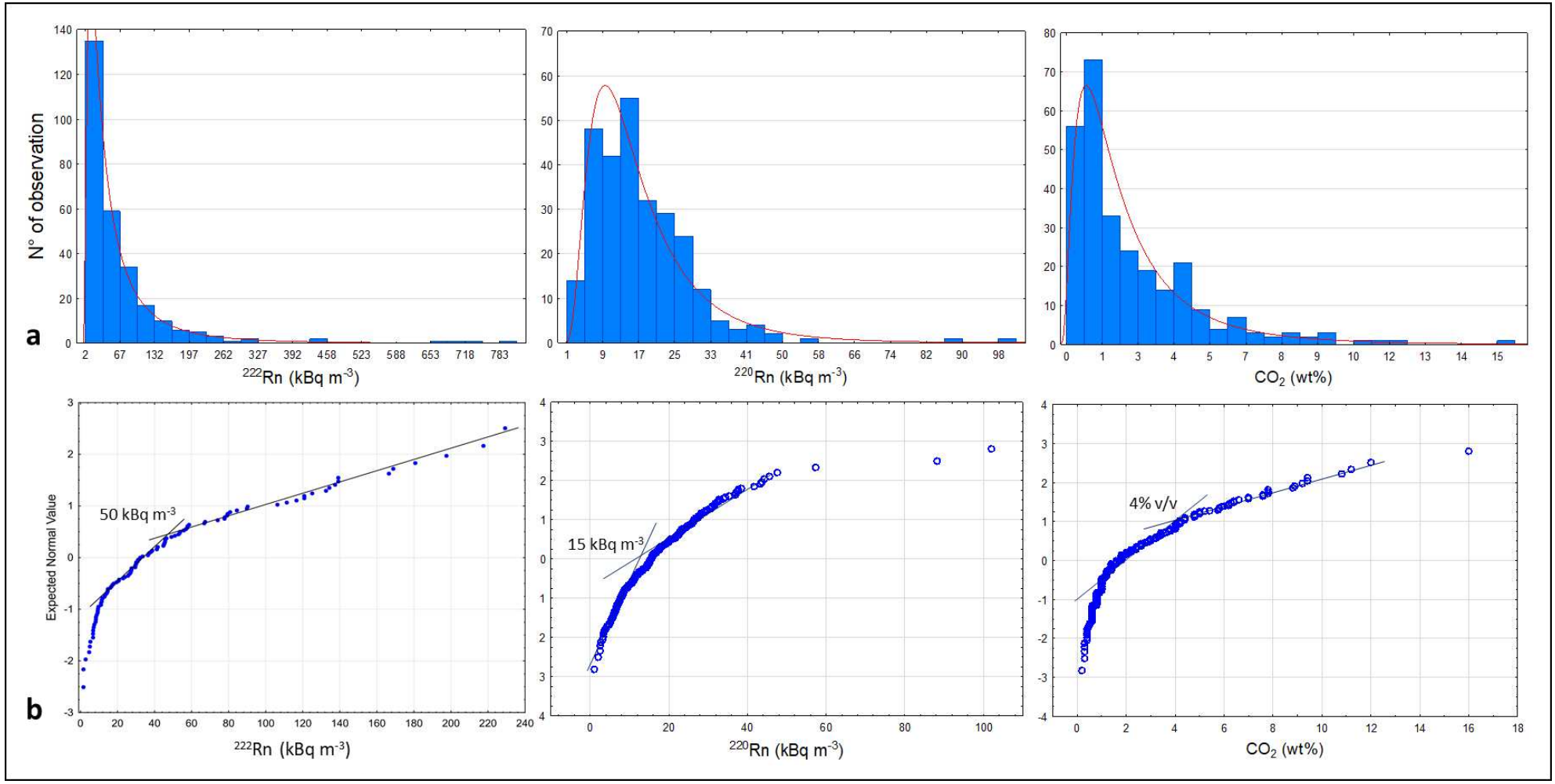

Figure A1. (**a**) Histograms and (**b**) normal probability plots and of soil gas data. Concerning the NPP of radon, the x axis ranges between 1.54 kBq·m^{-3} (min) and 240 kBq·m^{-3}, in order to better highlight the anomaly threshold.

Table A2:

Lithology		^{238}U (Bq kg^{-1})	σ %	^{226}Ra (Bq kg^{-1})	σ %	^{232}Th (Bq kg^{-1})	σ %	^{40}K (Bq kg^{-1})	σ %	U (ppm)	Ra (ppm)	Th (ppm)	K (wt%)	^{222}Rn* (Bq m^{-3})
Gneiss	PU04	19	18	82	13	38	11	1469	6	1.5	7.4	9.4	4.7	83.50
	AN01	22	19	60	11	42	16	1436	6	1.8	5.4	10.3	4.6	
	CS01	21	22	25	17	26	9	627	6	1.7	2.3	6.4	2.0	
	PU02	49	16	59	12	40	19	1025	6	4.0	5.4	9.7	3.3	
	NE02	15	28	19	27	26	14	695	6	1.2	1.7	6.5	2.2	
	NE03	33	11	41	9	50	7	689	6	2.6	3.7	12.3	2.2	
	FA01	26	12	26	18	57	7	1325	5	2.1	2.3	14.1	4.2	
Granite	MU05	47	20	75	12	111	9	1575	6	3.8	6.8	17.2	5.0	68.30
	FA03	38	20	41	11	69	9	428	7	3.0	3.7	16.9	1.4	
	FA04	25	26	28	23	47	11	942	6	2.1	2.5	11.5	3.0	
	FA05	35	17	51	9	52	7	1121	6	2.9	4.6	12.9	3.6	
Phyllite	PU05	26	15	24	14	32	8	436	7	2.1	2.1	7.8	1.4	27.71
	SS01	25	10	35	12	52	8	1100	5	2.0	3.1	12.7	3.5	
	SS02	36	15	49	20	87	7	1352	5	2.9	4.4	21.3	4.3	

Table A2. Radionuclide content (Bq·kg^{-1}) in the main outcropping lithologies in the study area: gneiss (e.g., orthogneiss, paragneiss), granite and phyllite. *^{222}Rn = mean ^{222}Rn activity (kBq·m^{-3}) at equilibrium with parent radionuclides (^{226}Ra) obtained by the Akerblom formula (Akerblom, 1993).

Figure A2:

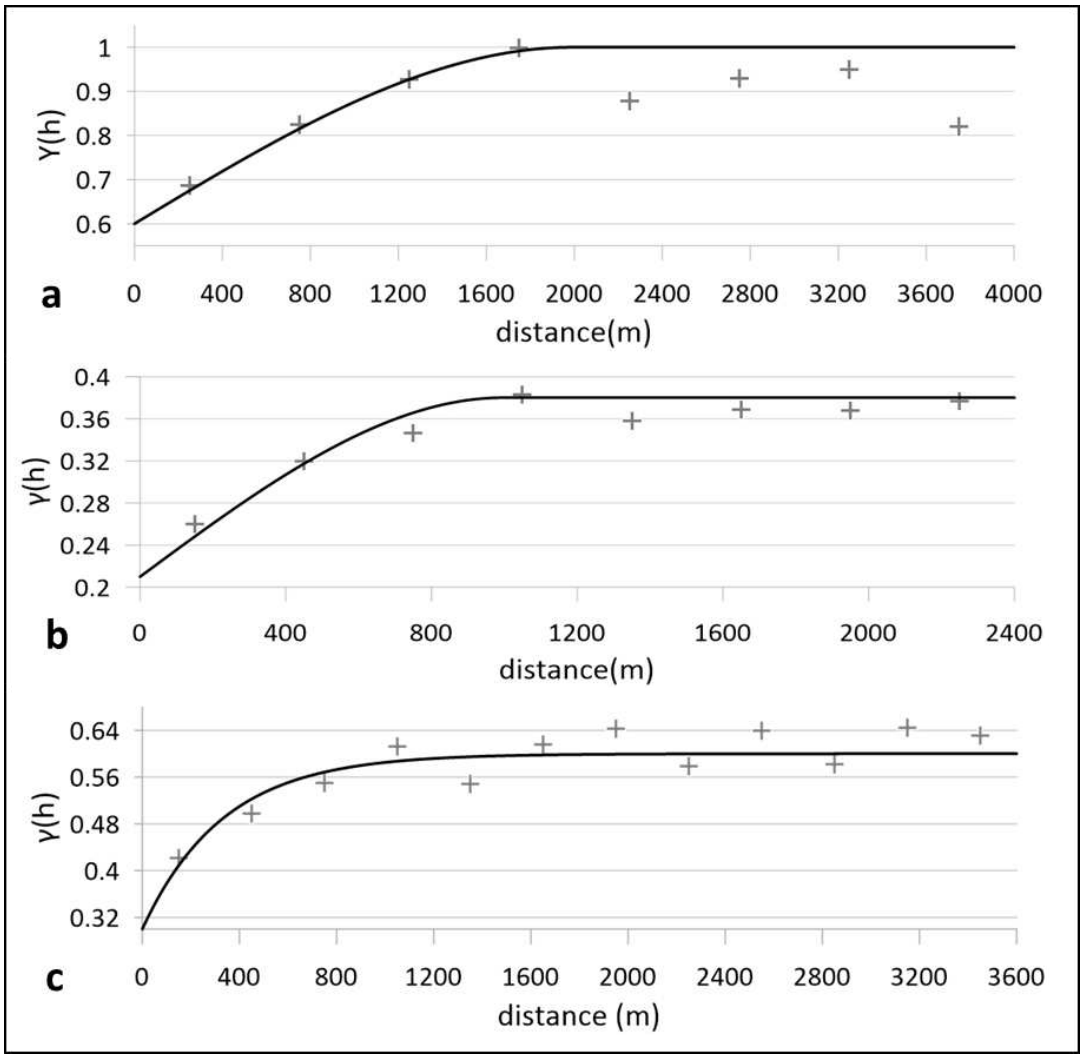

Figure A2. Experimental variograms and models calculated for (**a**) ^{222}Rn, (**b**) ^{220}Rn and (**c**) CO_2. Crosses indicate mean γ values for each lag and continuous lines indicate the variogram models. Following the equations of the selected models:
γ(h) = 0.6*Nugget+0.4*Spherical (2000, 1000, 90) for ^{222}Rn (**a**);
γ(h) = 0.21*Nugget+0.17*Spherical (1000, 500, 50) for ^{220}Rn (**b**);
γ(h) = 0.3*Nugget+0.3*Exponential (1000, 500, 95) for CO_2 (**c**).

Figure A3:

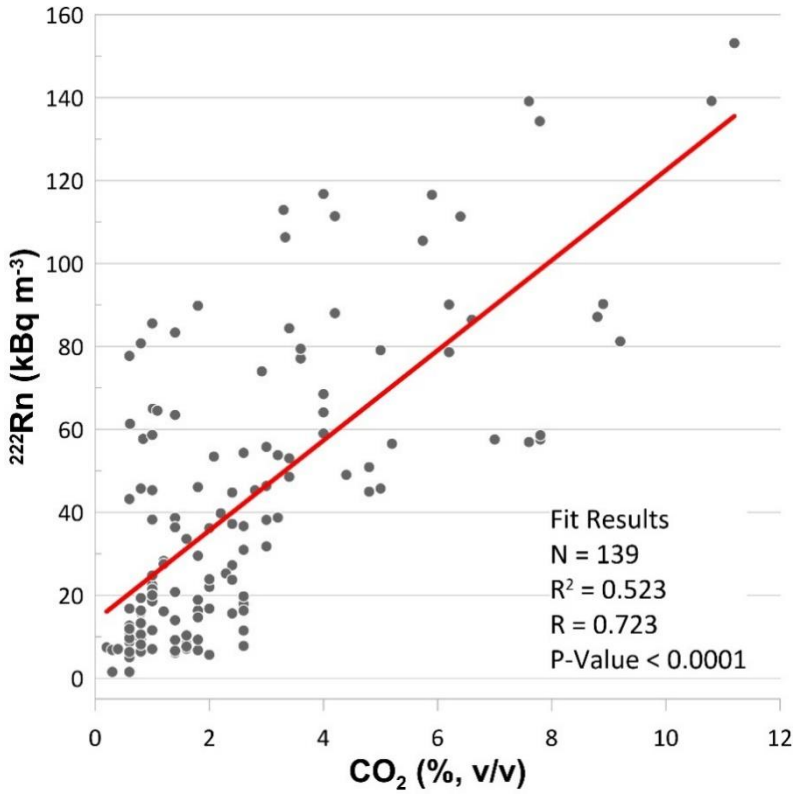

Figure A3. Scatterplot ^{222}Rn (kBq·m^{-3}) versus CO_2 (%, v/v) shows that there is a significant linear relationship between the two gases (p value < 0.0001) with coefficients R = 0.723 and R^2 = 0.523.

Appendix 2

Figure A1:

CO_2 (%)

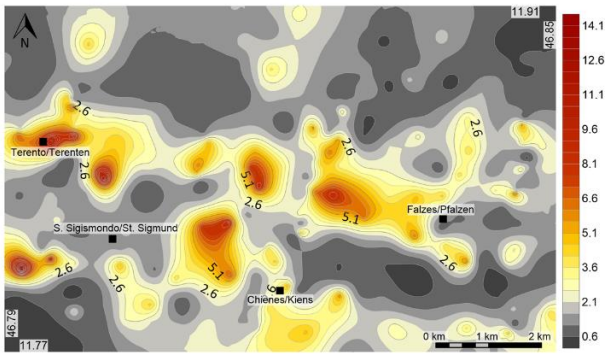

^{220}Rn (kBqm^{-3})

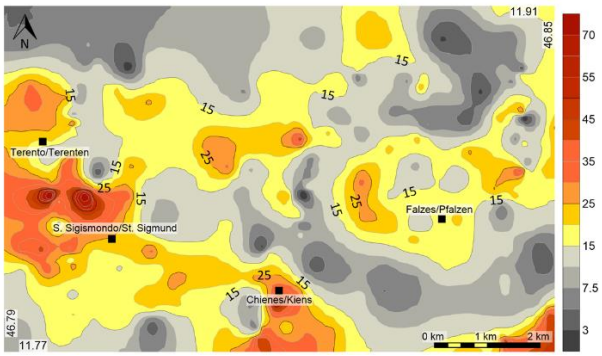

TGDR (µSv/h)

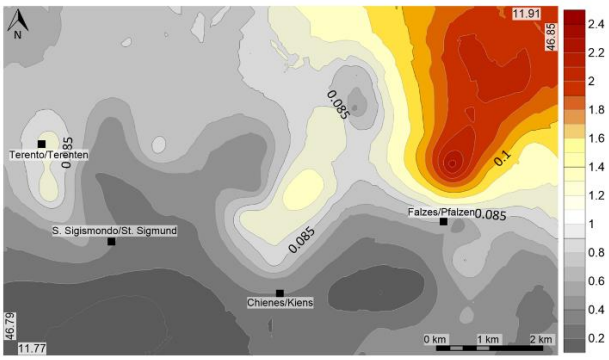

Permeability (m^2)

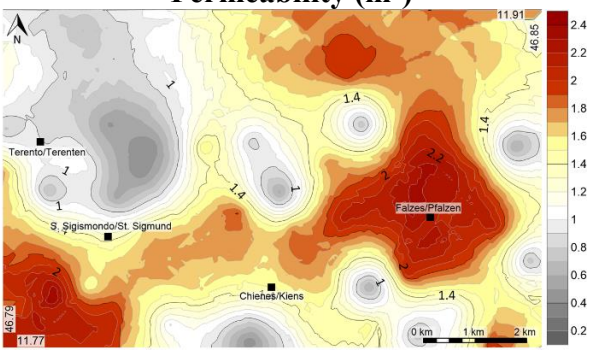

Elevation (m.a.s.l.)

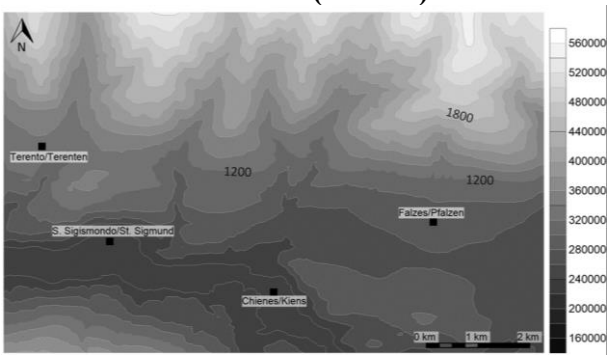

Slope (%)

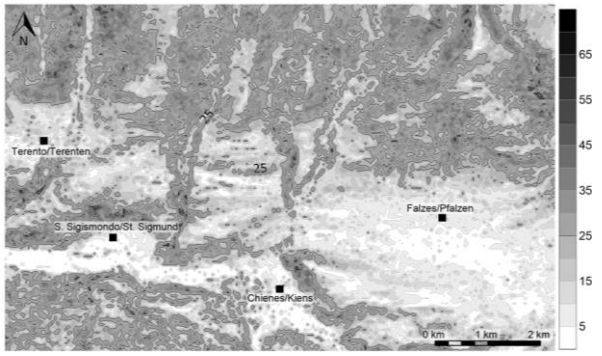

Solar radiation (Wh/m²)

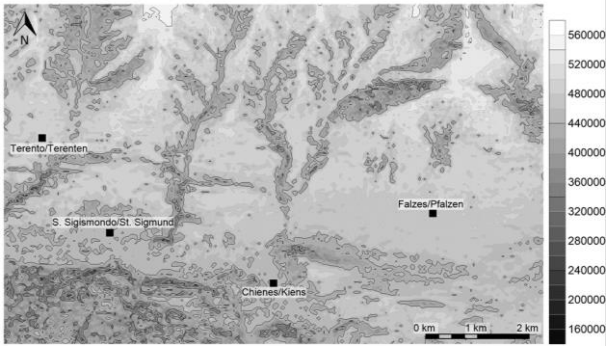

Aspect (degrees)

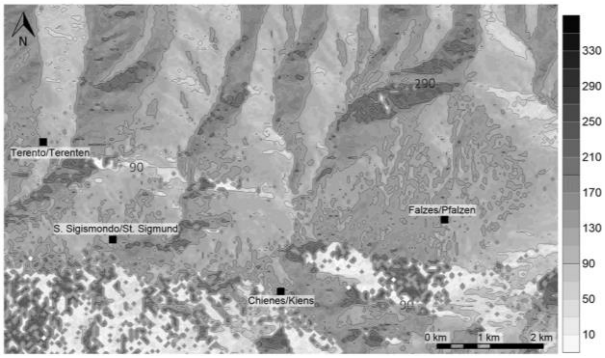

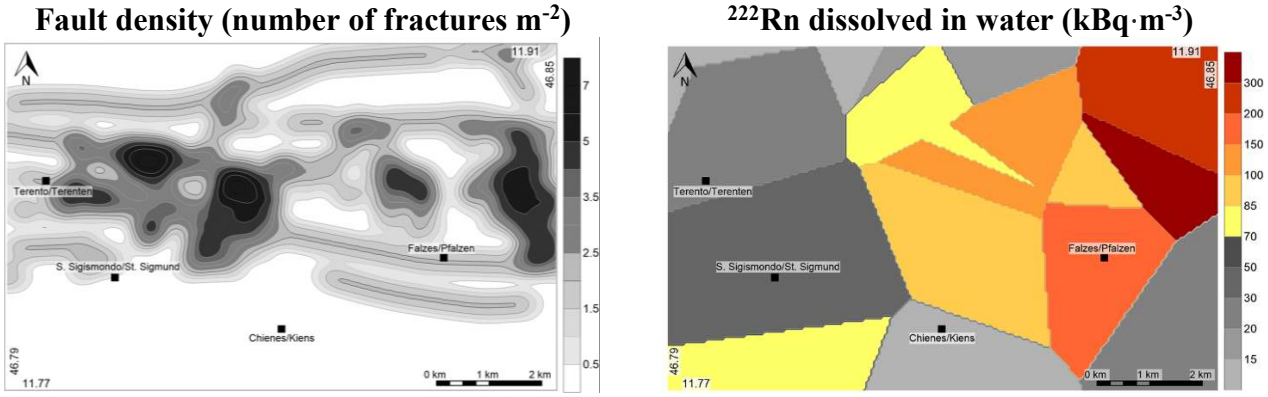

Figure A1. The 10 potential predictor variables transformed into 50m x 50m raster grids.
CO_2 = carbon dioxide; ^{222}Rn = radon; ^{220}Rn = thoron, TGRD = Terrestrial Gamma Dose Rate.

Figure A2 a, b:

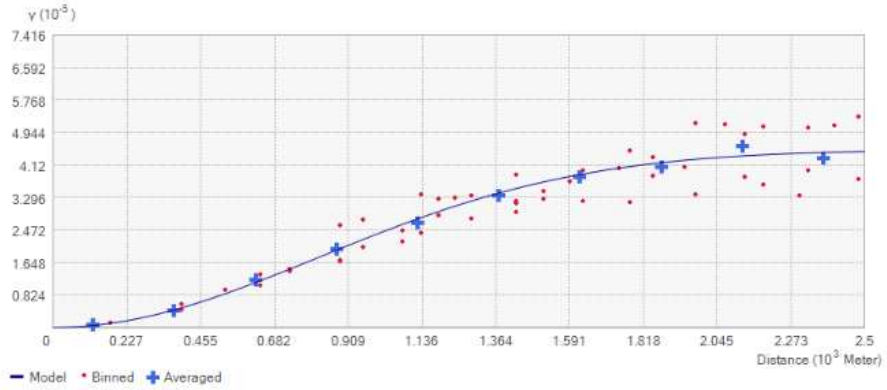

Figure A2a. Calculated experimental variogram of Terrestrial Gamma Dose Rate (TGDR). The equation of the selected model is: γ (y) = 4.5e-8*Nugget+0.000045*Gaussian (2000,1000,43,0).

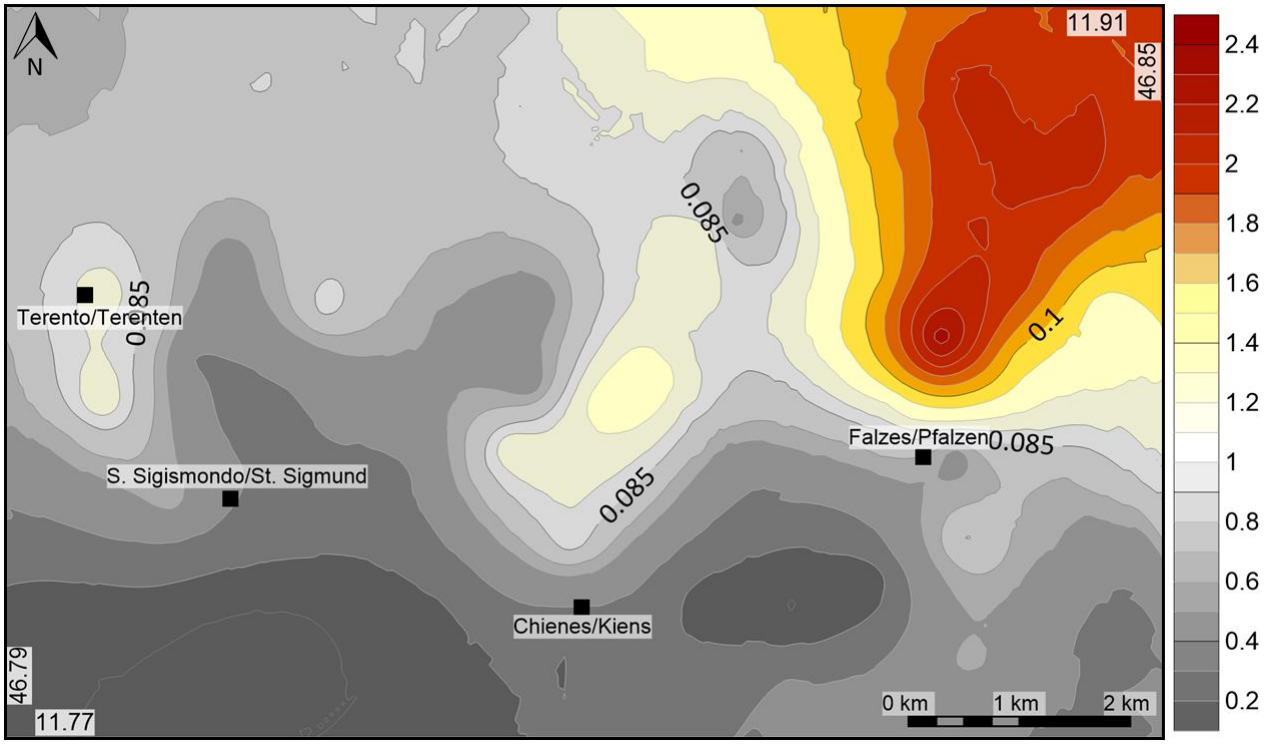

Figure A2b. Prediction map of the Terrestrial Gamma Dose Rate (TGDR) expressed in μSv/h. TGDR ranges between a minimum value of 0.06 μSv/h and a maximum value of 0.12 μSv/h.

Figure A3 a, b:

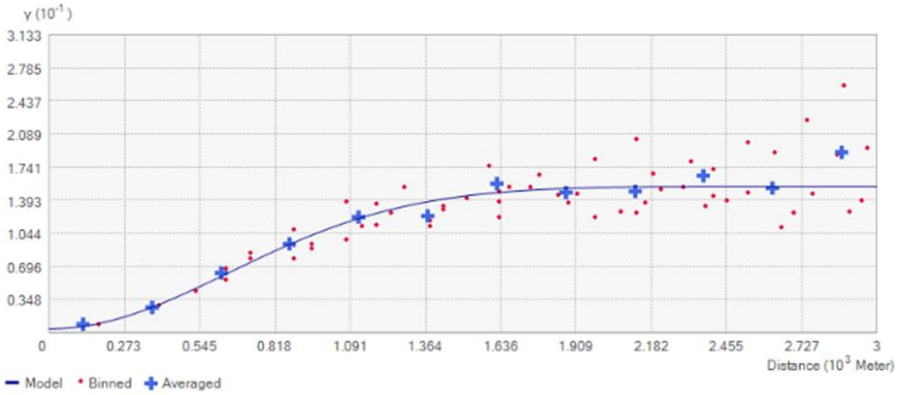

Figure A3a. Calculated experimental variogram of permeability. the equation of the selected model is: γ (y) = 0.004*Nugget+0.15*Gaussian (1600,800,73,0).

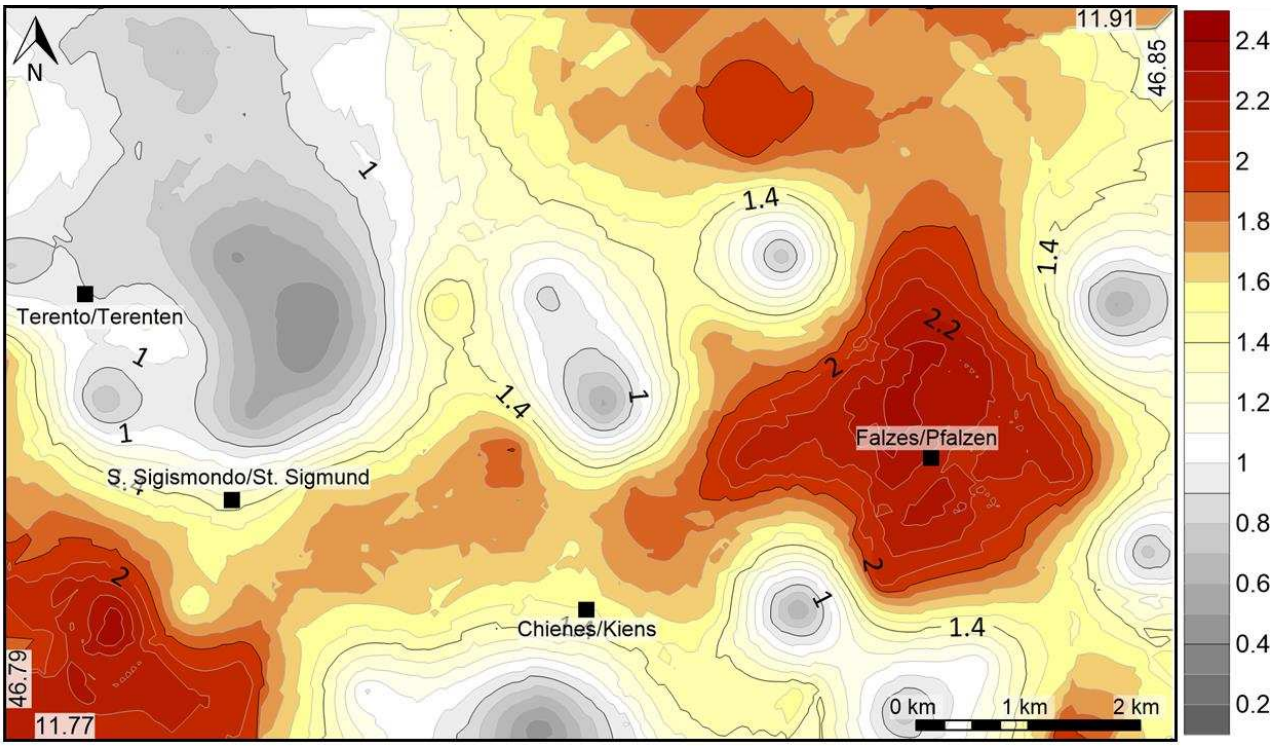

Figure A3b. Prediction map of the soil permeability expressed in m^2. The permeability ranges between a minimum value of 0.43 m^2 and a maximum value of 2.34 m^2.

Table A1:

Variable	Coefficient	Std. coeff.
TGDR	39.131	0.413
FD	0.109	0.151
Solar	0.000	0.000
Slope	0.010	0.103
Aspect	0.013	0.100
DTM	0.000	-0.001
^{220}Rn	0.014	0.129
CO2	0.240	0.427
Permeability	0.384	0.149
^{222}Rn in water	0.000	0.057
Intercept	-1.487	

Table A1. The results of LASSO regression of the 10 candidates.
TGDR = terrestrial gamma dose rate; FD = fault density; Solar = solar radiation; DTM = digital terrain model; ^{220}Rn = Thoron; CO_2 = carbon dioxide.

Table A2:

Predictor	VIF
TGDR	1.51
FD	1.35
^{220}Rn	1.06
CO_2	1.08
Permeability	1.17
Slope	1.23
Aspect	1.04

Table A2. Variance Inflection Factor (VIF) values of the 7 selected predictors in the RF model.
TGDR = terrestrial gamma dose rate; FD = fault density; Solar = solar radiation; DTM = digital terrain model; ^{220}Rn = Thoron; CO_2 = carbon dioxide. All the selected predictors show VIF < 7.

Figure A4:

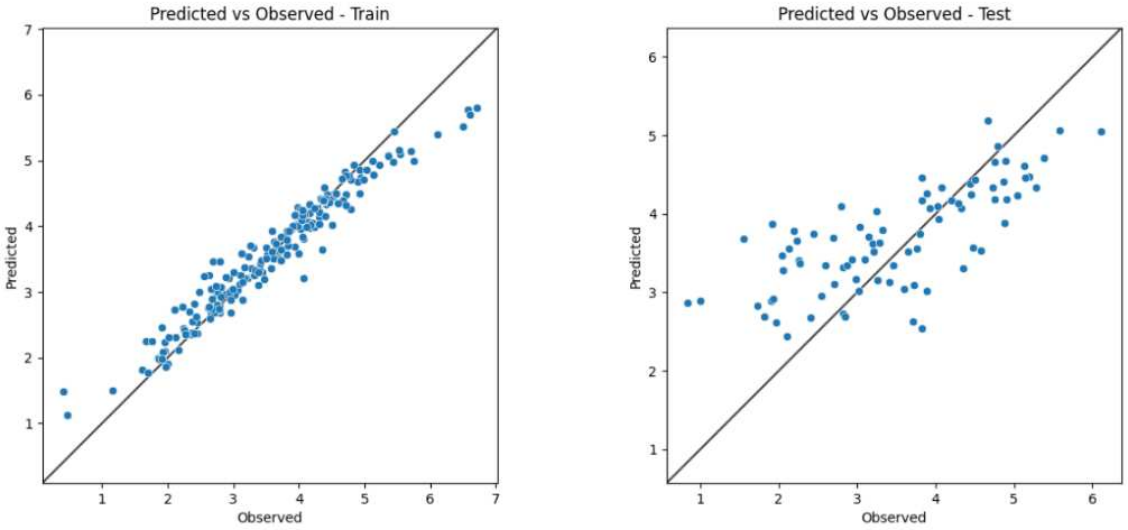

Figure A4. Predicted vs. observed values for training (to the left) and test (to the right) data.

Figure A5:

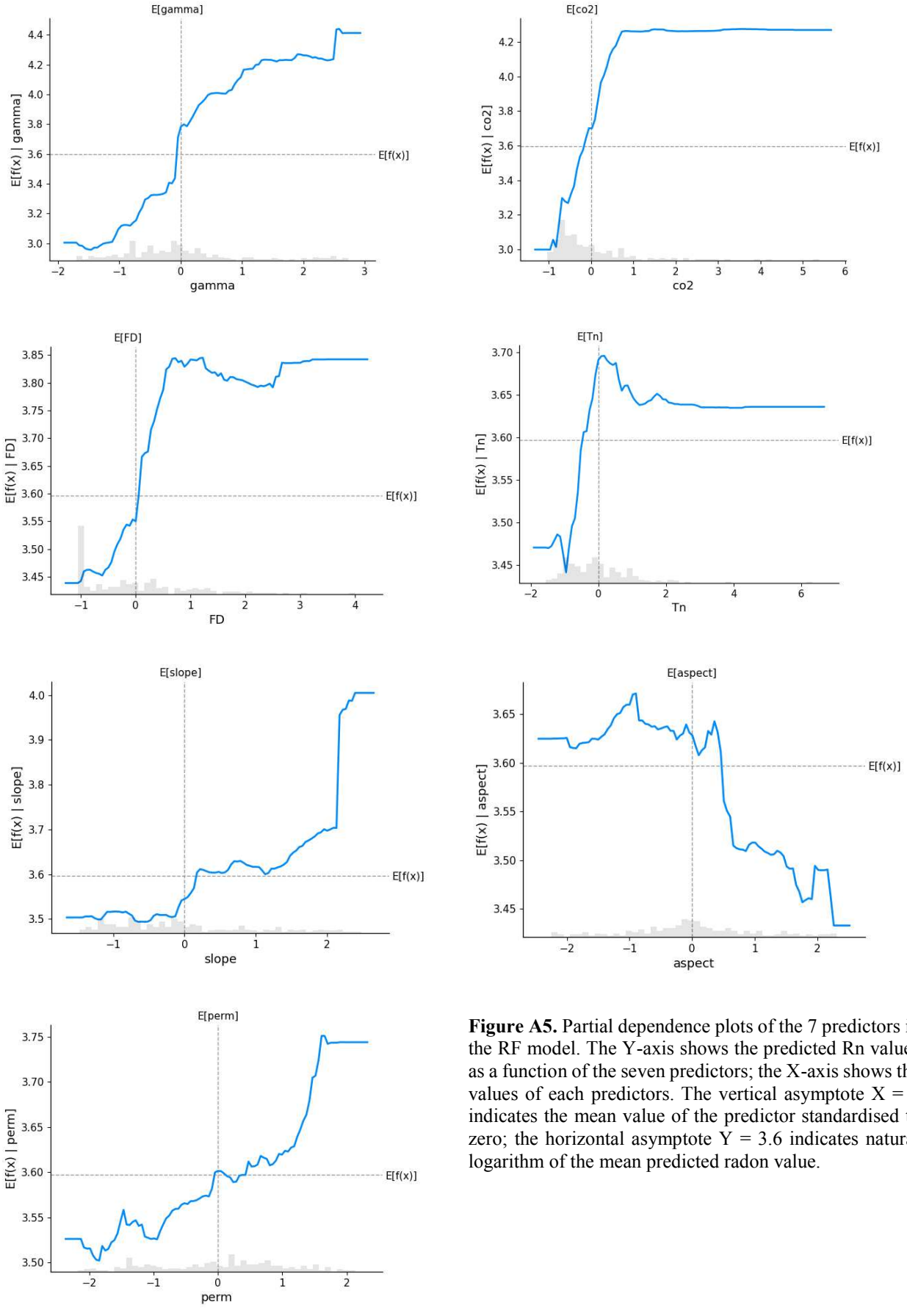

Figure A5. Partial dependence plots of the 7 predictors in the RF model. The Y-axis shows the predicted Rn values as a function of the seven predictors; the X-axis shows the values of each predictors. The vertical asymptote X = 0 indicates the mean value of the predictor standardised to zero; the horizontal asymptote Y = 3.6 indicates natural logarithm of the mean predicted radon value.

Explanation of figure A5:

On the Y-axis, the predicted radon values from our model are shown as a function of each predictor (i.e., TGDR, FD, CO_2, ^{220}Rn, slope, aspect, permeability); on the X-axis, the values of the predictor values are displayed. The axes have been standardized to facilitate comparison between predictors, with Y = 3.6 representing the natural logarithm of the mean predicted radon, and X = 0 indicating the mean value of the standardised predictor. The resulting curve identifies the relationship between the predictor variable and the expected radon values in the RF model. Figure 6 shows that for negative scores of TGDR, FD, CO_2, ^{220}Rn, slope, and permeability, the curve increases up to the expected average radon value. The aspect acts differently, with negative values displaying a slight upward trend and a slight decrease for expected radon values above the mean of 3.6. Furthermore, even for radon values higher than the expected mean, the curve exhibits an increasing trend for positive scores of TGDR, FD, CO_2, slope, and permeability. This implies that these variables are significant in predicting radon potential, which increases as the predictor values increase. The curves for CO_2 and FD, in particular, reach a plateau, indicating that as these two variables increase, the predicted radon remains constant. However, for positive ^{220}Rn values, the curve drops until it reaches a plateau above the expected mean radon value. This indicates that as ^{220}Rn increases, radon rises and then falls until it stabilizes above its expected mean. The aspect behaviour appears different than the other predictors. The curve grows sharply for negative aspect scores and decreases for radon values above the expected mean. For positive aspect scores, however, the curve rapidly drops below the expected mean radon value. As a result, both predicted radon and aspect decrease, accordingly. The PDP of each predictor is calculated by accounting for the average effect of the other predictors in the model.

Appendix 3

Figure A1:

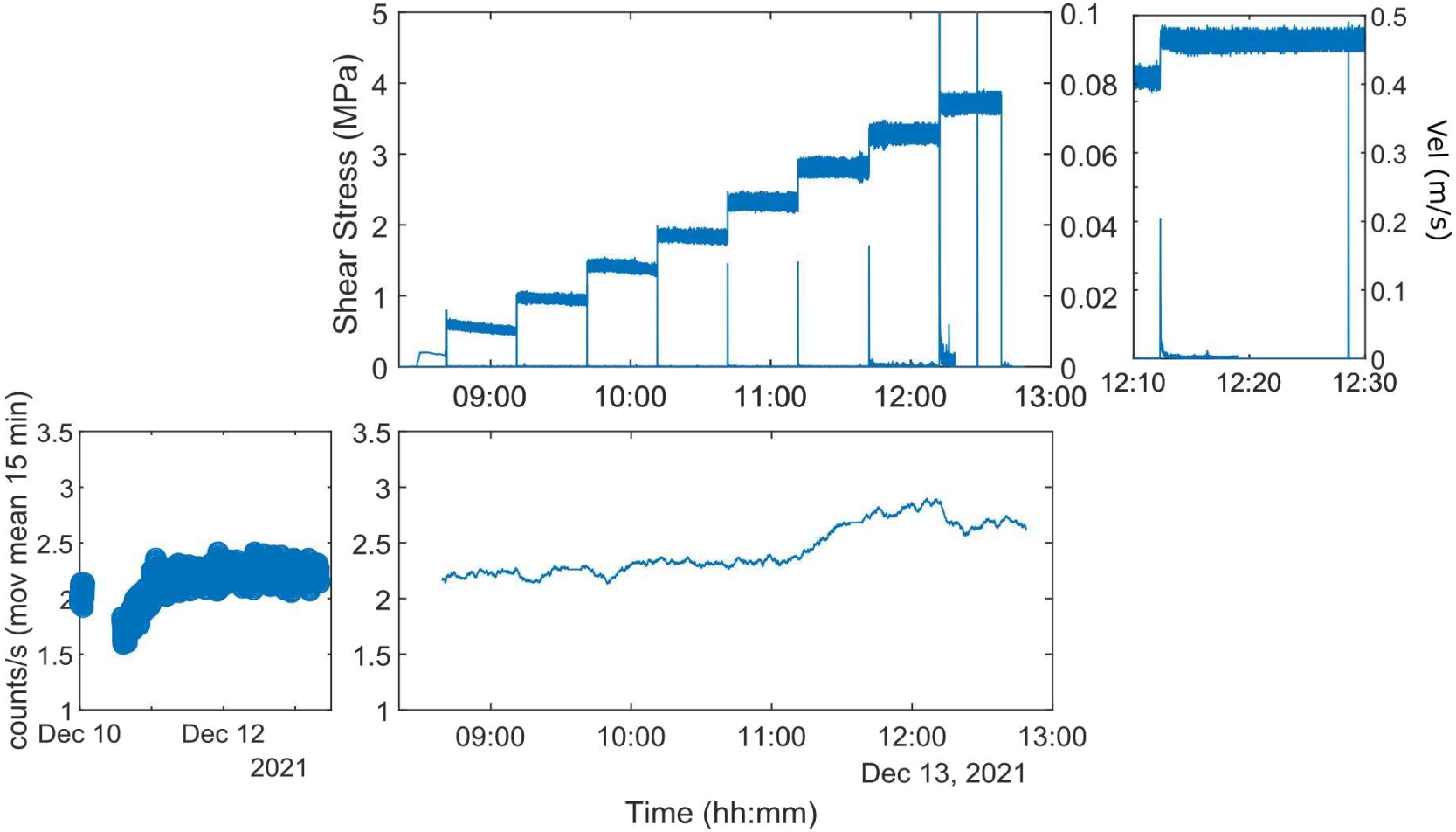

Figure A1. Top left panel: shear stress (MPa, blue) vs. time (hh:mm) for the duration of the experiment. Top right panel: a zoom of the shear stress representing one of the fast slip events recorded before the main frictional instability. Bottom left panel: the radon counts/s moving average over 15 min in the pre-experiment phase (lasted 36 hours) during and after achievement of the secular equilibrium between ^{222}Rn and its short-lived progeny. Bottom right panel: the variation in radon counts/s during the experiment (lasted ca. 4 hours) with respect to the radon initial conditions.

Figure A2:

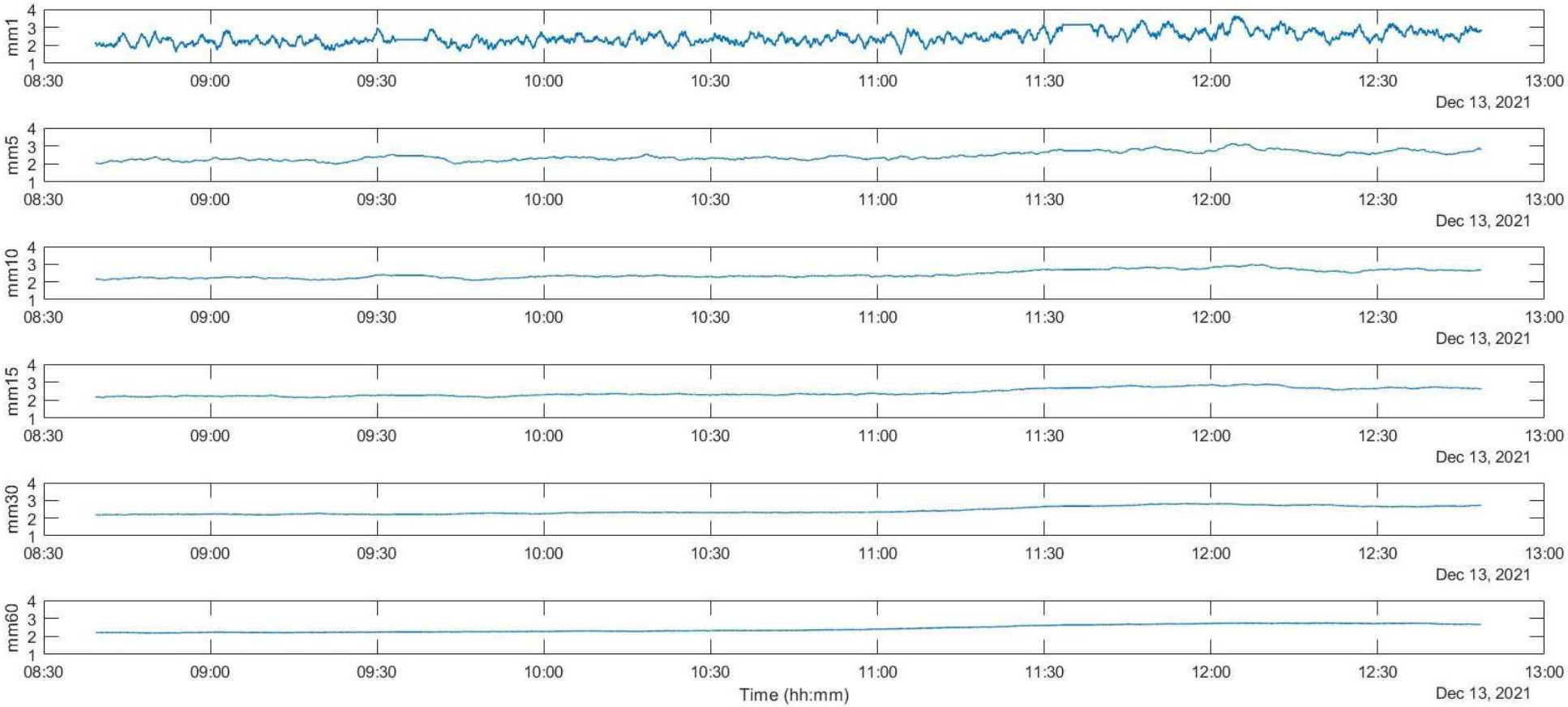

Figure A2. One example of the different sampling rates for a granite, experiment s1895. Blue line: radon, count/s moving average over 1 min, 5 min, 10 min, 15 min, 30 min and 60 min. The change point analysis was performed using a1 min moving average.

Figure A3:

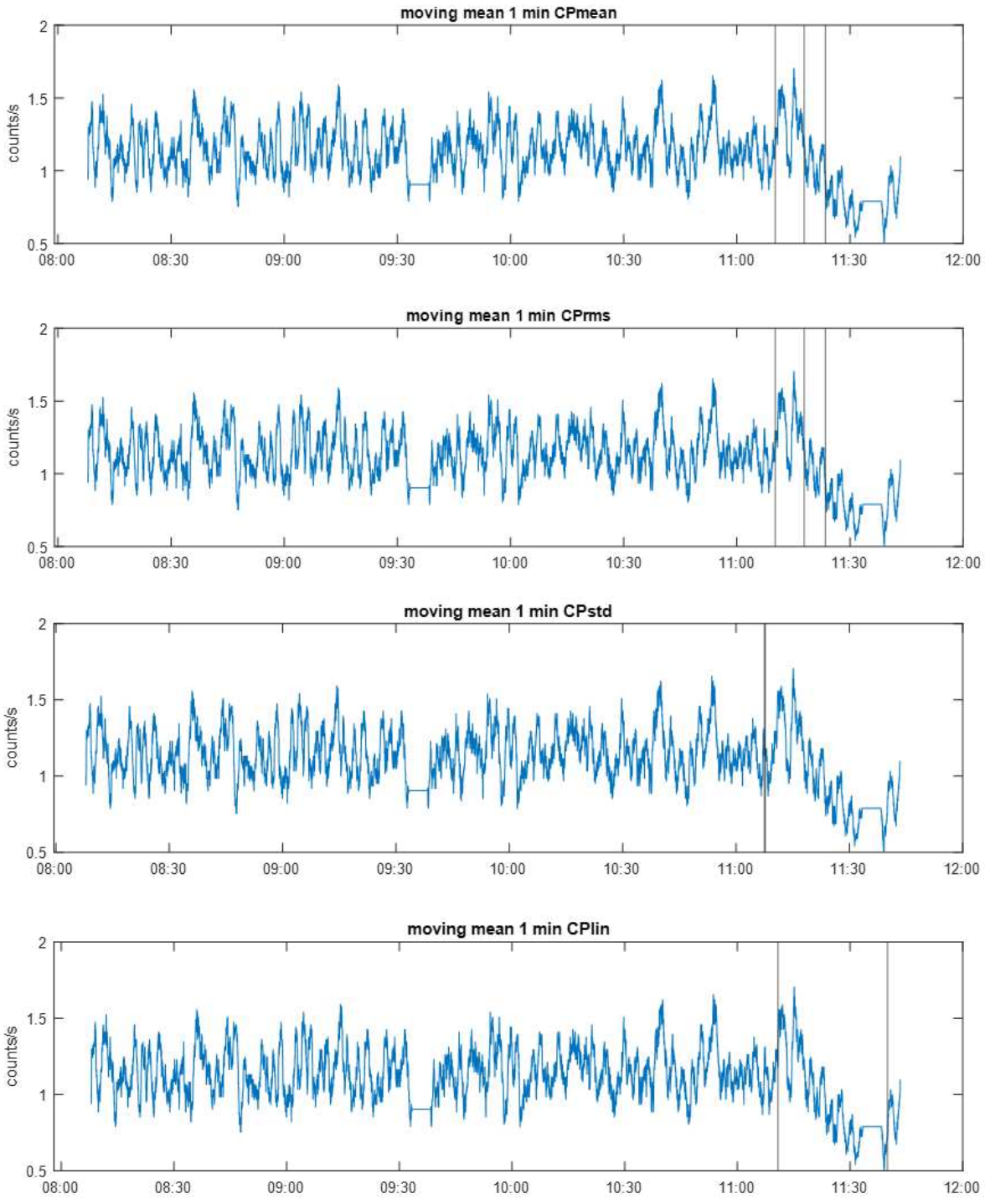

Figure A3. Paragneiss s1896. Blue line: radon, count/s moving average over 1 min, grey lines change points.

Figure A4:

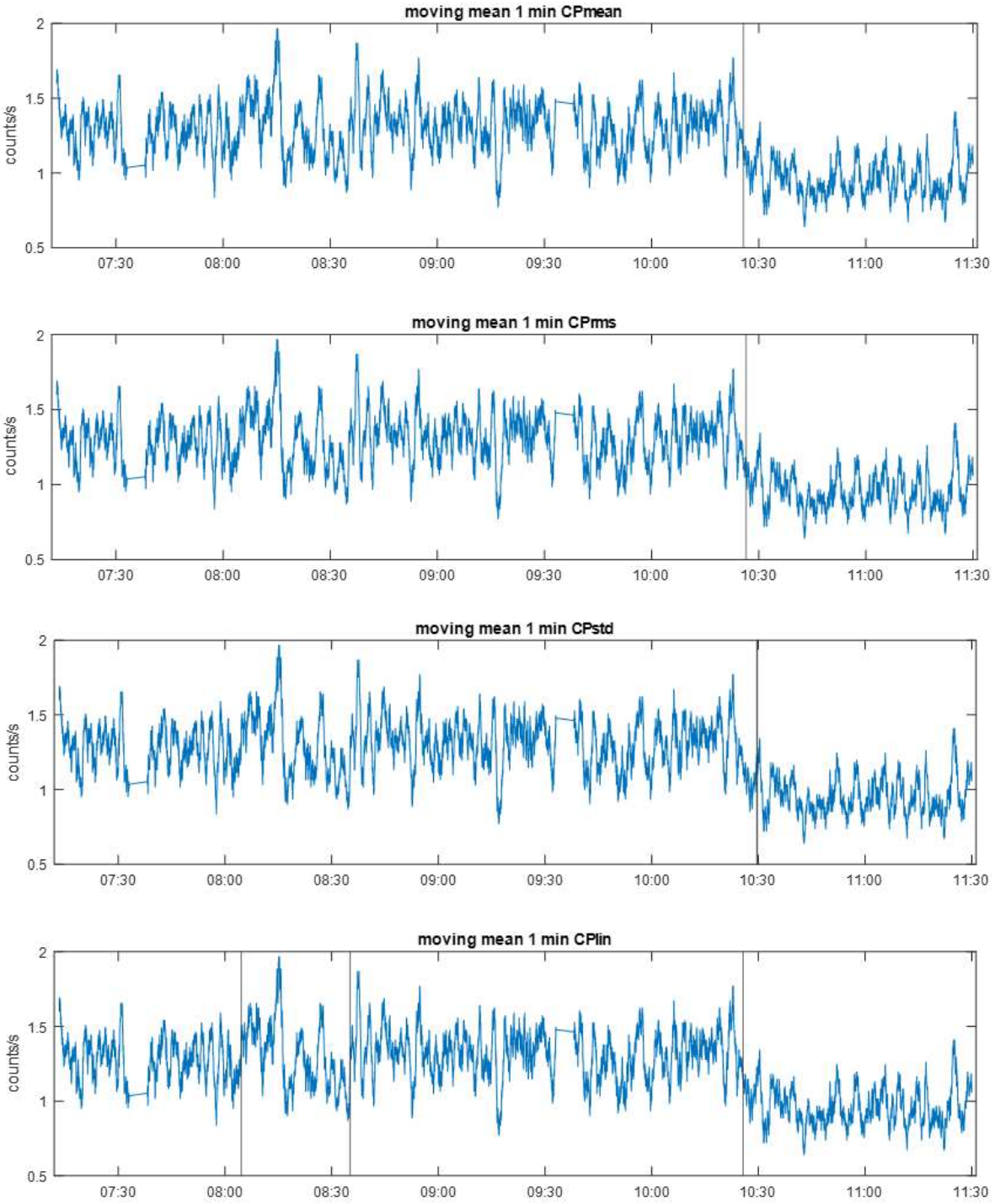

Figure A4. Paragneiss s1904. Blue line: radon, count/s moving average over 1 min, grey lines change points.

Figure A5:

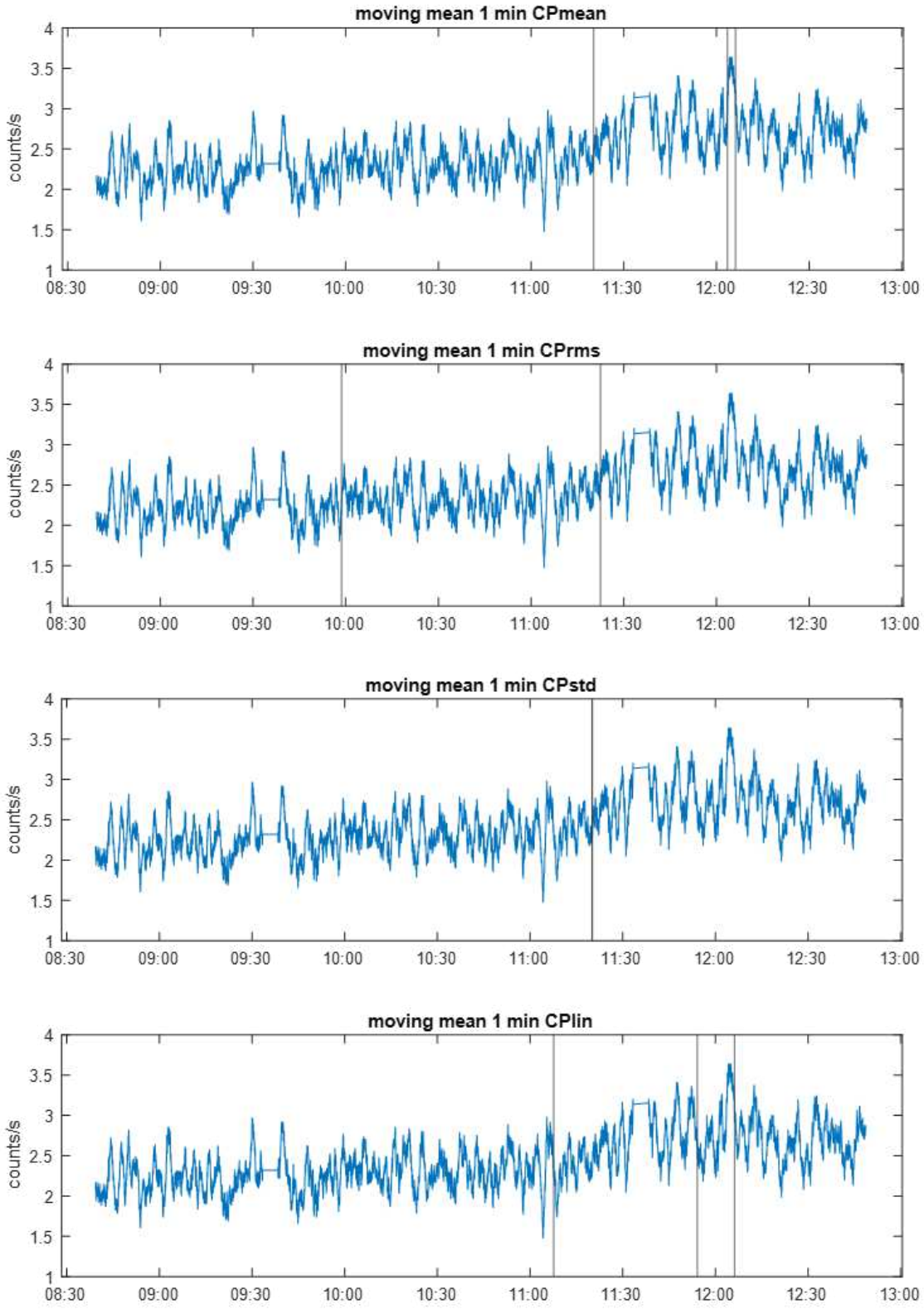

Figure A5. Granite s1895. Blue line: radon, count/s moving average over 1 min, grey lines change points.

Figure A6:

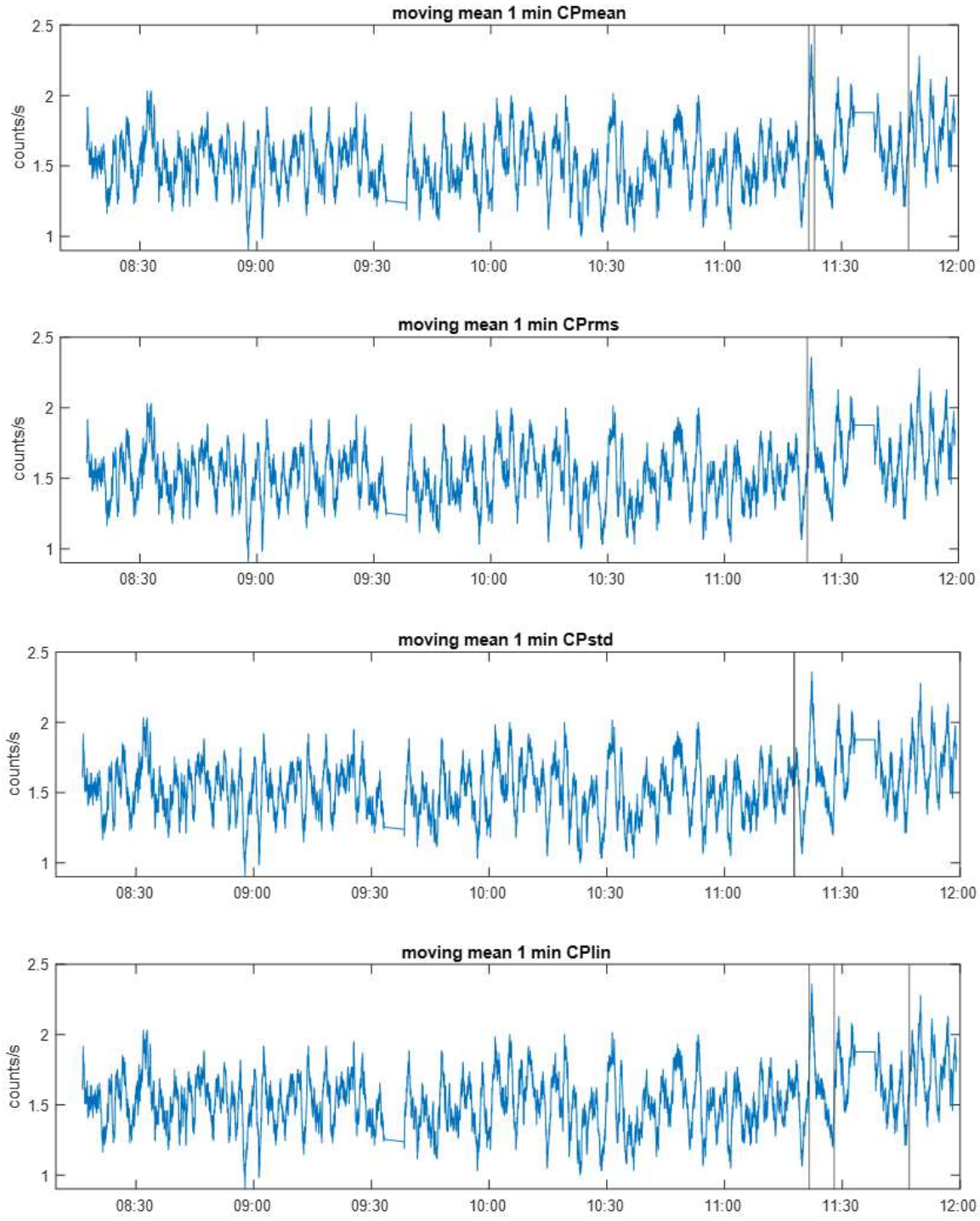

Figure A6. Granite s1897. Blue line: radon, count/s moving average over 1 min, grey lines change points.

Figure A7:

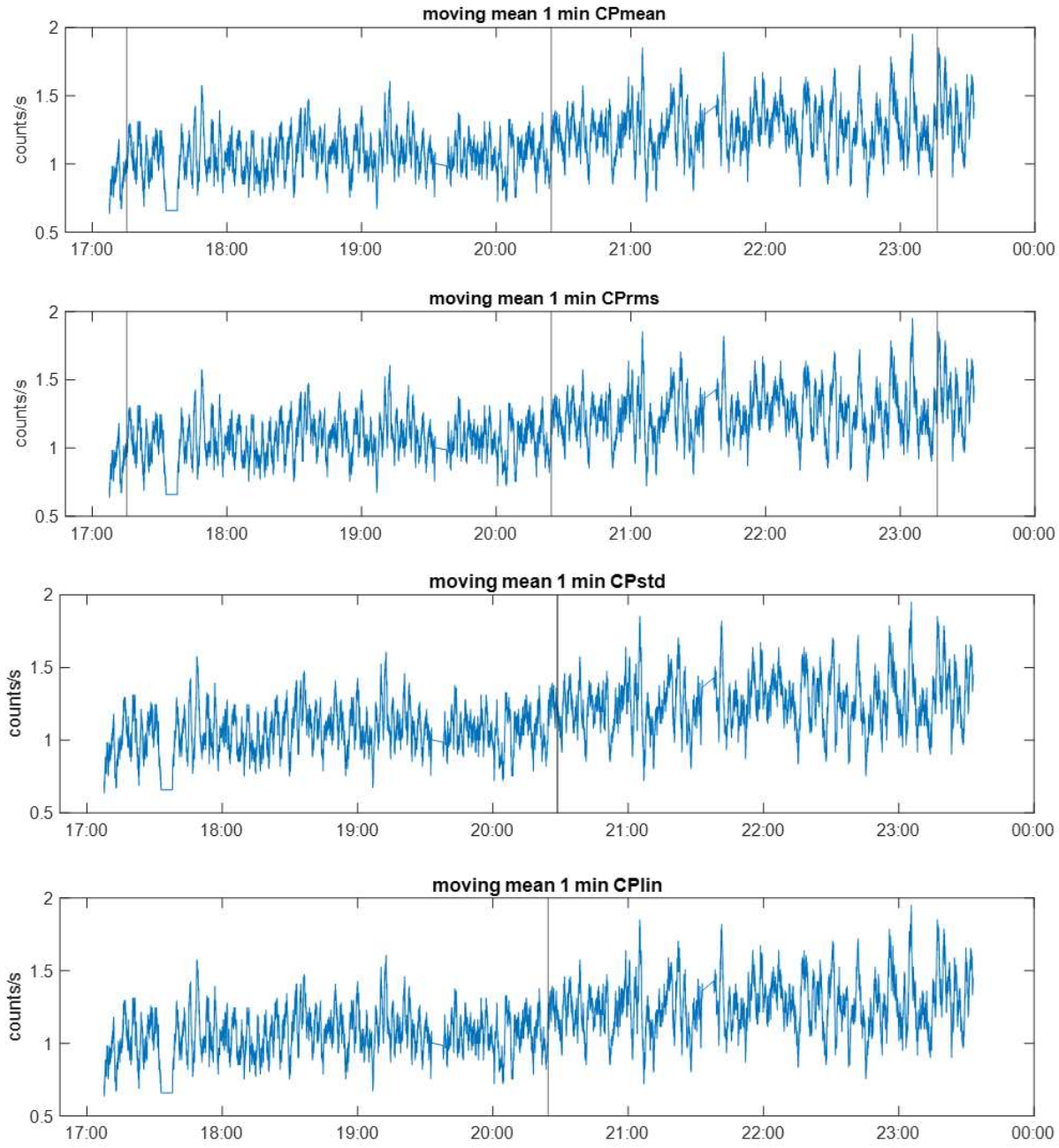

Figure A7. Orthogneiss s1916. Blue line: radon, count/s moving average over 1 min, grey lines change points.

Figure A8:

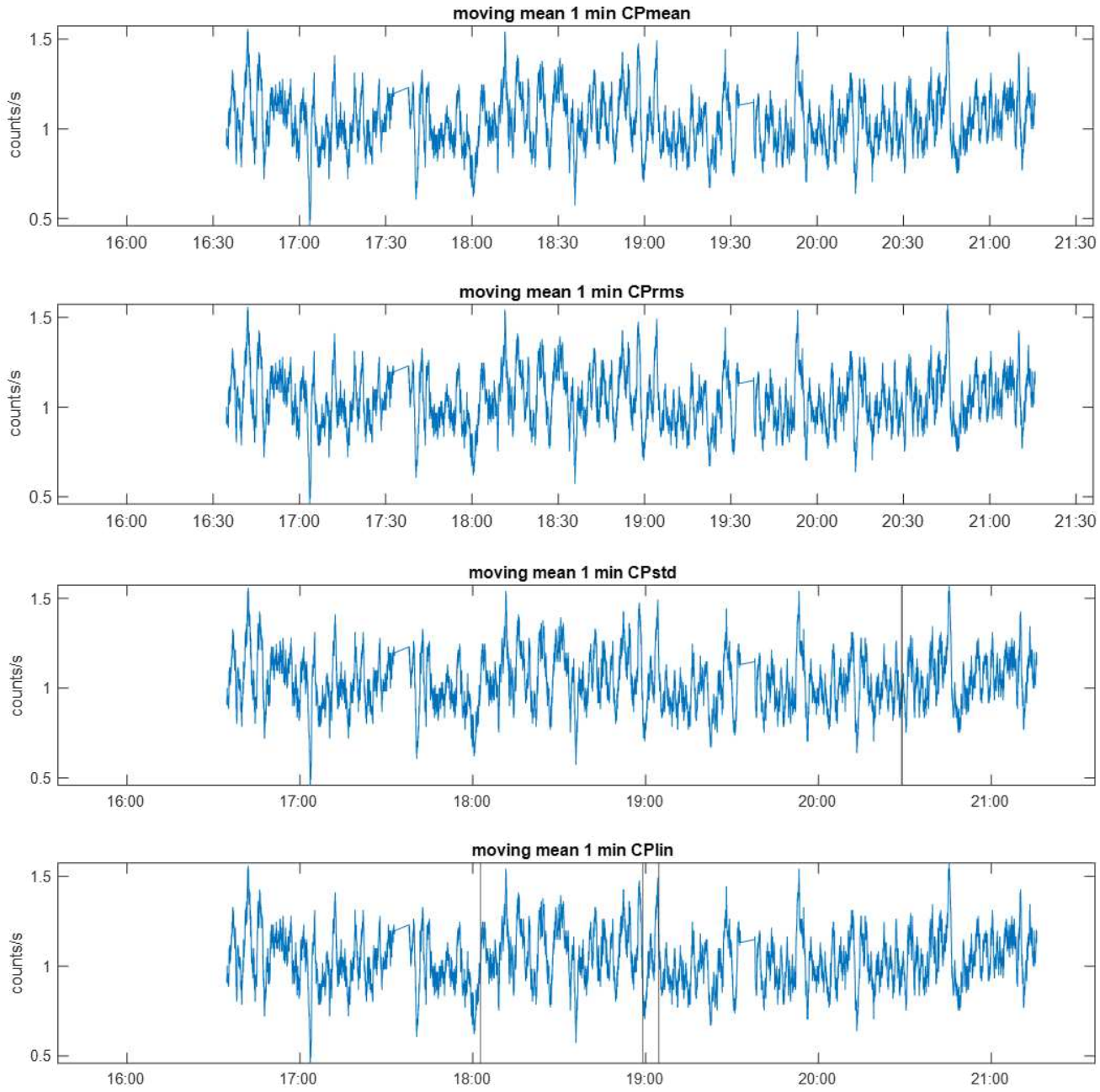

Figure A8. Orthogneiss s1917. Blue line: radon, count/s moving average over 1 min, grey lines change points.

Figure A9:

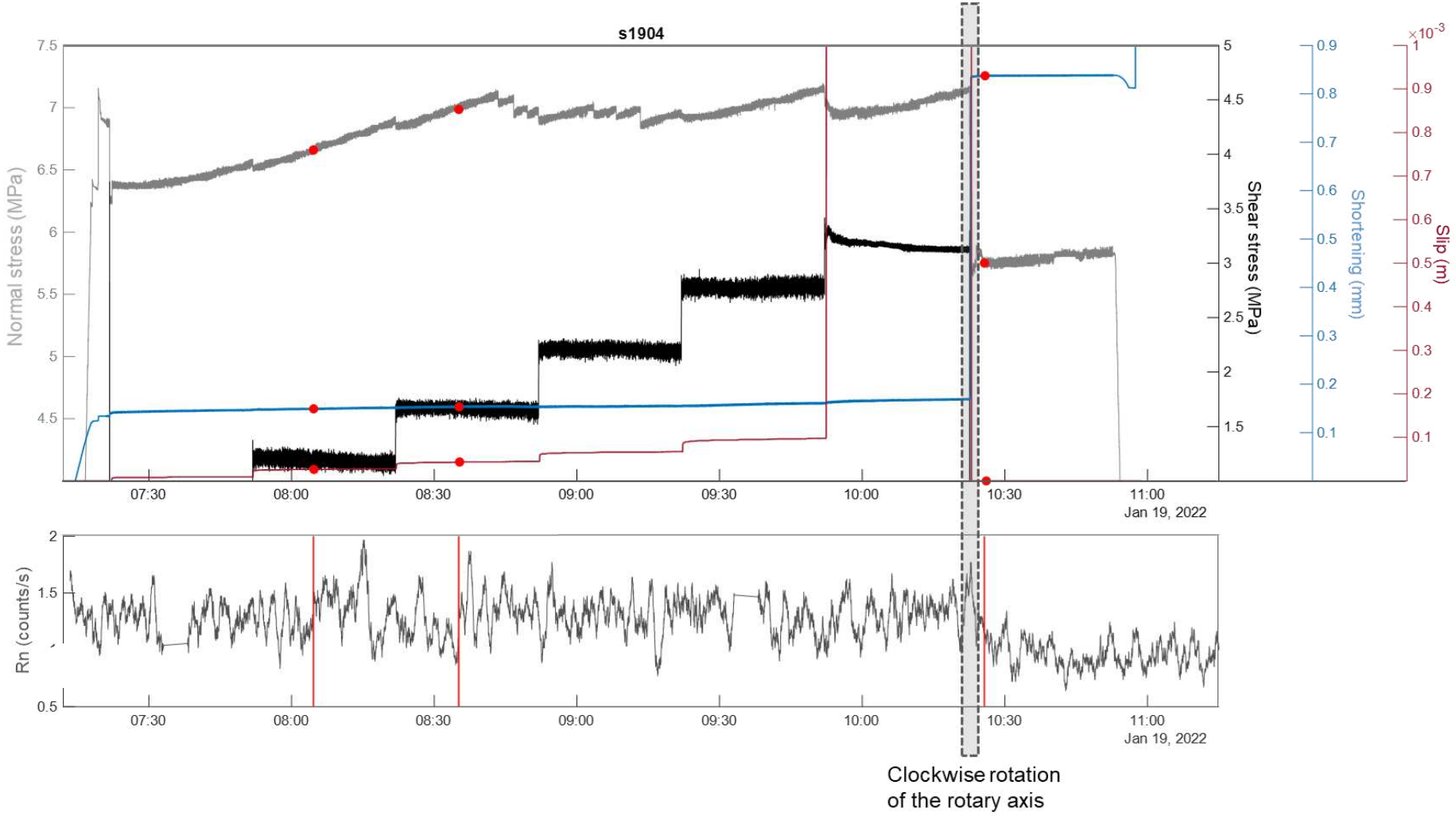

Figure A9. Paragneiss s1904. Top panel: dark grey normal stress (MPa), black shear stress (MPa), dark red slip (m), blue axial shortening (mm); red points change points (std). Bottom panel: radon, count/s moving average over 1 min, red lines change points (std).

Figure A10:

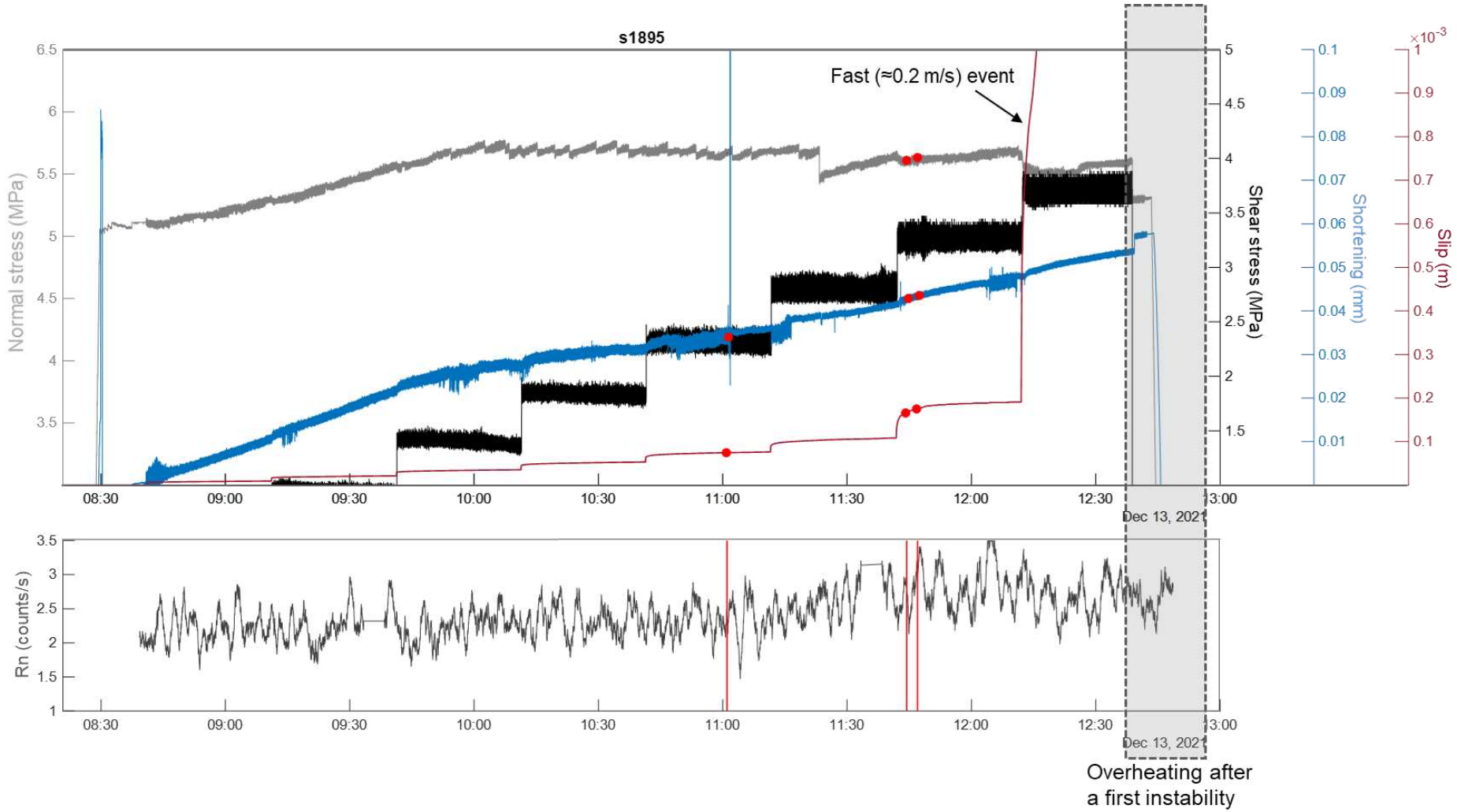

Figure A10. Granite s1895. Top panel: dark grey normal stress (MPa), black shear stress (MPa), dark red slip (m), blue axial shortening (mm); red points change points (mean). Bottom panel: radon, count/s moving average over 1 min, red lines change points (mean).

Figure A11:

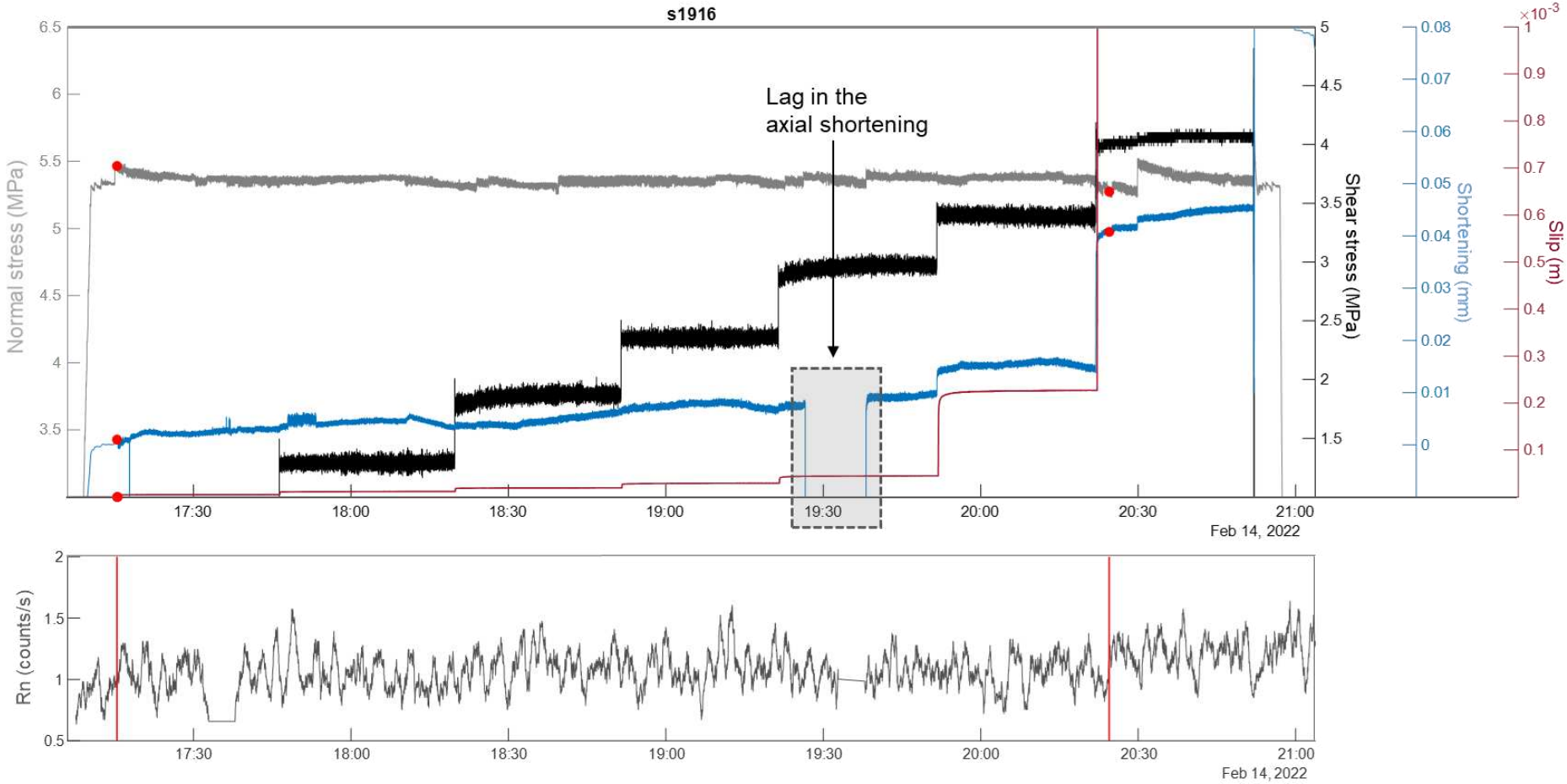

Figure A11. Orthogneiss s1916. Top panel: dark grey normal stress (MPa), black shear stress (MPa), dark red slip (m), blue axial shortening (mm); red points change points (mean). Bottom panel: radon, count/s moving average over 1 min, red lines change points (mean).

Figure A12:

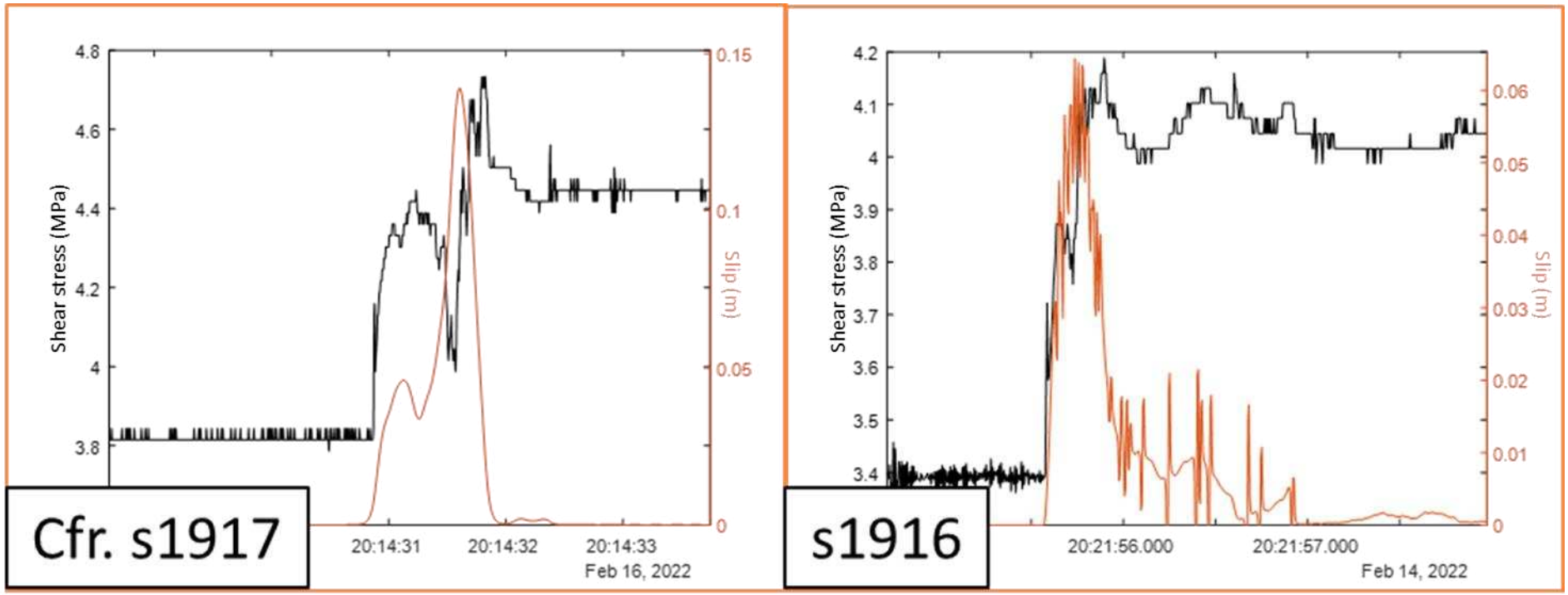

Figure A12. Shear stress (black line, MPa), slip (orange line, m). Short and fast slip events recorded before the main instability event in experiments s1917 and s1916, compared. These events reached slip velocities of 0.15 and 0.06 m/s respectively. Other events were detected by the change points analysis.